SYNTHESIS AND MECHANICAL PROPERTIES OF HIERARCHICAL NANOPOROUS METALS

A Dissertation
Presented to
The Academic Faculty

By

Ran Liu

In Partial Fulfillment
Of the Requirements for the Degree
Doctor of Philosophy in the
Georgia W. Woodruff School of Mechanical Engineering

Georgia Institute of Technology
August 2015

SYNTHESIS AND MECHANICAL PROPERTIES OF HIERARCHICAL NANOPOROUS METALS

Approved by:

Dr. Antonia Antoniou, Advisor
School of Mechanical Engineering
Georgia institute of Technology

Dr. Nathan Mara
CINT
Los Alamos National Lab

Dr. David McDowell
School of Mechanical Engineering
Georgia institute of Technology

Dr. Bruno Frazier
School of Electrical Engineering
Georgia institute of Technology

Dr. Olivier Pierron
School of Mechanical Engineering
Georgia institute of Technology

Date Approved: March 18, 2015

To My Beloved Parents and Grandparents

ACKNOWLEDGEMENTS

Foremost, I would like to foremost thank my advisor, Prof. Antonia Antoniou, for her continuous support of my Ph.D. study. My work would not have reached this state of completion without her invaluable encouragement, guidance and advice. She has been everything that I could ask for in a Ph.D. mentor and I am very grateful to her. I would like to express my gratitude to my thesis committee members: Prof. David McDowell, Prof. Olivier Pierron, Dr. Nathan Mara and Prof. Bruno Frazier for their help and guidance during the course of my research here at Georgia Tech. I would like to acknowledge NSF for funding this project. This work was performed, in part, at the Center for Integrated Nanotechnologies (CINT).

I would like to thank Mr. Kevin Baldwin for alloy deposition which enabled me to synthesize the nanoporous metals used in my study. I would also like to thank Bill Mook for his help with in-situ mechanical experiments at CINT. I wish to thank Dr. Vadim Roytershteyn for his wisdom and friendship. During my time here, he was available to chat with me and has provided me valuable advice on a number of research and non-research related issues.

I would like to acknowledge Mr. Eric Woods and Dr. Walter Henderson in Nanotechnology Research Center at Georgia Tech for their assistance on equipment training and troubleshoot issues. They are always there when I need help. I couldn’t have asked for a better support group. I would also like to thank all my friends and labmates for making my stay at Georgia Tech more memorable and enjoyable.

Finally, I would like to thank my family for giving me much needed support through my many years of school, allowing me to pursue my interests and complete this thesis.

TABLE OF CONTENTS

LIST OF TABLES

LIST OF FIGURES

LIST OF ABBREVIATIONS

3D	Three dimensional
NP	Nanoporous
PVD	Physical vapor deposition
SCE	Saturated calomel electrode
SEM	Scanning electron Microscope
TEM	Transmission electron microscope
RBS	Rutherford Backscattering Spectrommetry
SE	Secondary electron
XPS	X-ray Photoelectron Spectroscopy
NT	Nanotwinned
NC	Nanocrytalline
XPS	X-ray Photoelectron Spectroscopy
HF	Hydrofluoric acid
MD	Molecular dynamics
LAMMPS	Large-scale Atomic/Molecular Massively Parallel Simulator
EAM	Embedded atom method
HRTEM	High resolution TEM
FFT	Fast Fourier Transform
XRD	X-Ray Diffraction

LIST OF SYMBOLS

$\boldsymbol{E_f}$	Foam modulus
$\boldsymbol{E_s}$	Modulus of a solid strut
$\boldsymbol{E'}$	Biaxial modulus of NP metal
$\boldsymbol{\rho^*}$	Relative density
$\boldsymbol{\rho_{NP\ metal}}$	Density of NP metal
$\boldsymbol{\rho_{solid\ strut}}$	Density of solid strut
$\boldsymbol{\rho_{initial\ alloy}}$	Density of initial alloy
$\boldsymbol{\rho}$	Number density which is equal to N/V
$\boldsymbol{\alpha}$	Ratio of N/N'
$\boldsymbol{\beta}$	Factor describing differences of the internal structure
$\boldsymbol{N}$	Number of atoms in the initial alloy
$\boldsymbol{N'}$	Number atoms in the NP metal
$\boldsymbol{x}$	Atom fraction in the initial alloy by mass
$\boldsymbol{V}$	Control volume
$\boldsymbol{l}$	Length of thin film composed of initial alloy
$\Delta\boldsymbol{l}$	Change in length
$\mathbf{W}$	Width of thin film composed of initial alloy
$\Delta\mathbf{w}$	Change in witdh
$\boldsymbol{h}$	Height/thickness of thin film composed of initial alloy
$\Delta\boldsymbol{h}$	Change in height
$\mathbf{K}$	A proportionality constant
$\boldsymbol{\sigma_{NP\ metal}}$	Strength of NP metal

$\boldsymbol{\sigma_{solid\ strut}}$	Strength of a solid strut
$\boldsymbol{\sigma_s}$	Strength of a solid strut
$\boldsymbol{\sigma}$	Stress required to prevent sample shrinkage
$\boldsymbol{\sigma_m}$	Mismatch stress
$\boldsymbol{\sigma_y}$	Yield strength
$\boldsymbol{\sigma_y^T}$	Yield strength in tension
$\boldsymbol{\sigma_c^T}$	Yield strength in compression
$\boldsymbol{dh}$	Dimensional change in one direction
$\boldsymbol{\lambda_{min}}$	A minimum crack spacing
$\boldsymbol{\Gamma}$	Fracture energy of the film
$\boldsymbol{t}$	Strut thickness
$\boldsymbol{l}$	Strut length
$\boldsymbol{d}$	Joint size
$[\boldsymbol{\varepsilon}]$	Stopping cross section factor
$\boldsymbol{\rho_M^*}$	Experimentally obtained relative density
$\boldsymbol{\hat{I}}$	Threshold intensity
$\boldsymbol{I}$	Intensity of the grayscale micrograph image
$\boldsymbol{I_t}$	Critical intensity value that segregates the image to specific features
$\boldsymbol{L_x}$	Width of the image
$\boldsymbol{L_y}$	Height of the image
$\overline{\boldsymbol{\rho(x,y,z)}}$	Average over a narrow surface layer
$\boldsymbol{\rho_{M_i}^*}$	Relative line density
$\boldsymbol{E_j^*}$	Relative modulus with enlarged joints
$\boldsymbol{E^*}$	Relative modulus without enlarged joints

$\boldsymbol{\nu^P}$	Poisson's ratio of NP metal
$\boldsymbol{P}$	Force applied at the midpoint of the strut length
$\boldsymbol{M}$	Moment related to the force *P*
$\boldsymbol{\delta_c}$	Displacement at the midpoint of the strut length
$\boldsymbol{\varepsilon}$	Strain related to the displacement δ_c
$\boldsymbol{I_1}$, $\boldsymbol{I_2}$	Moment of Inertia
$\boldsymbol{\lambda}$	Twin lamella spacing
$\boldsymbol{t_f}$	Film thickness
$\boldsymbol{H_f}$	Hardness of NP metal
$\boldsymbol{C_G}$	Geometrical constant
$\boldsymbol{C_H}$	Ratio of strut hardness to strength
E	Atomic strain tensor
E*	Atomic deviatoric strain tensor
F	Deformation gradient tensor
I	Identity tensor
$\boldsymbol{e^*}$	The second invariant of the deviatoric strain tensor
$\boldsymbol{q}$	Ratio of yield strength in tension to that in compression
$\mathbf{p_m}$	Mean pressure of indentation
$\boldsymbol{\varepsilon_m}$	Mean strain of indentation
$\boldsymbol{a}$	Contact radius of indentation

SUMMARY

Nanoporous (NP) metals are a unique class of materials that are characterized by extremely high surface-to-volume ratios and possess such desirable properties of metals as high electrical conductivity, catalytic activity, and strength. Due to these properties, NP metals have demonstrated great potential in many applications. At the same time, a deep understanding of their mechanical properties is lacking, especially for hierarchical metals where individual struts and joints that make up open cell 3D network are nanocrystalline. The aim of this work is to provide such understanding through a dedicated experimental campaign. Towards this goal, a variety of hierarchical NP metal systems have been synthesized, such as nanocrystalline NP Pt and nanotwinned NP Cu. I examined the mechanical properties of these systems via *ex-situ* and *in-situ* nanoindentation experiments to infer scalings of modulus and strength with crucial parameters such as relative density and characteristic dimensions of struts. The ex-situ experiments performed to date have shown that NP Pt and NP Cu are found to have highly elevated properties comparable to single-crystal systems and far exceeding expectations based in simplified dimensional arguments. The origin of this enhancement is traced back to a combination of material effects arising from small dimensions of the struts/joints and the geometrical features of NP metals. Selected applications of the systems synthesized during this work in electrochemistry and catalysis are demonstrated, typically with the performance comparable to or exceeding the best available alternative system.

CHAPTER 1

INTRODUCTION

1.1 ***Nanoporous Metals***

Nanoporous (NP) metals are a unique class of materials characterized by extremely high surface-to-volume ratios, high electrical conductivity, catalytic activity, and strength. This unusual combination of properties is highly attractive in many applications. Indeed, NP metals have shown great promise as key components of electrodes in batteries [1], supercapacitors [2, 3], as well as catalysts [4-7], sensors [8-10], and filters. It is important to emphasize that these materials are rapidly moving from proof-of-concept systems to being considered for practical applications. At the same time, fundamental understanding of the origins of their properties is lacking, significantly hindering further progress. In almost all of the applications, understanding and controlling mechanical properties of NP metals is of paramount importance. For example, battery electrodes require materials that accommodate volumetric changes during cycling without compromising their mechanical properties, while design considerations for catalysts require materials with good catalytic activity and stability after numerous cycles.

Structurally, open cell NP metals can be considered as three-dimensional (3D) network of struts and joints with comparable sizes in the nanometer range. Most of the work on NP metals to date has centered on NP Au with struts in the 2-100 nm range synthesized from initial alloy with micron sized grains [11-17]. In contrast, the systems examined in this work have nanograined struts. The abundance of free surfaces, large

relative density, and proximity of the typical sizes of the network building blocks to their internal length scales (e.g. sizes of the grains in polycrystalline metals) can therefore present unusual properties for these hierarchical NP metals. Clearly, the mechanical properties of the overall structure depend both on the material properties of individual struts and on their geometrical arrangement in space (we will refer to this as geometrical structure, or foam morphology). Yet, the hierarchical nanostructure of NP metals presents fundamental challenges to theoretical understanding of their behavior. At the same time, this inherent complexity offers exciting opportunities to optimize the macroscopic material properties.

The objectives of this dissertation are as follows:

1) To experimentally explore the synthesis of hierarchical NP metals by dealloying and to identify the degree of control over the NP metal structure that could be achieved by varying synthesis conditions.

2) To experimentally identify the key ingredients of the structure-property relation for hierarchical NP metals. This includes the role of geometry, and the role of material effects associated with internal structure of struts/joints with characteristic sizes in the 5-100 nm range.

3) Explore applications of NP metal systems synthesized during the course of this work to catalysis and energy storage.

1.2 ***Background***

1.2.1 Synthesis techniques

Dealloying is a technique frequently used to synthesize NP metals with pores and ligaments below 100 nm. Dealloying is essentially a controlled corrosion technique where element(s) of an alloy can be selectively dissolved in an aqueous solution. Under certain conditions, the remaining elements self assemble to form a three dimensional network of ligaments and pores [18-21]. A variety of NP metals have been successfully synthesized by dealloying, such as NP gold from Au-Ag alloy [11, 17, 19, 22-26]; NP platinum (Pt) from $Pt_{0.25}Cu_{0.75}$ [27] or amorphous Pt_xSi_{1-x} [28, 29]; NP nickel(Ni) from Ni_xCu_{1-x} [30]; and NP Copper (Cu) from Cu_xMn_{1-x} [31, 32], Cu_xZn_{1-x} [33, 34]. The initial alloy composition, dealloying rate, and the type of electrolyte control the ligament pore size of the open cell type foams. The ligament and pore sizes can be further coarsened by subsequent annealing [35, 36] or immersion in an electrolyte [37]. Dealloying has been successfully used to synthesize macroscopic free standing samples of both film and bulk materials. Crack formation during dealloying used to be a serious problem in the synthesis of NP metals. However, considerable progress has been made towards the synthesis of crack-free NP metal foams during the last decade. Several procedures have been proposed to minimize crack formation during synthesis, such as gentle dealloying [28, 38] or stepped potential technique [39].

1.2.2 Overview of the mechanical properties of NP metal foams

The mechanical properties of NP metals depend on both its morphology (the size and the geometrical arrangement of the interconnects) and on the properties of the

material making up the ligaments. However, in NP metals the characteristic sizes of pores and ligaments are such that the abundant free surfaces may play an important role, while the length-scales of ligaments are comparable to their internal features (e.g. grains). This leads to a fascinating coupling between geometry and material properties at the nano-scale.

A revealing way to appreciate the unique mechanical properties is given by a weight-normalized strength to stiffness diagram as shown on Fig. 1.1 for a variety of materials [40]. Clearly, NP metals fall outside the bounds of either dense metals or bulk foams. Experimentally, mechanical properties of NP metal foams can be captured by a variety of tests. Nanoindentation and micropillar compression capture the behavior of a small volume of material, while macroscopic tensile or compressive tests assess response of a larger volume (see also Section 4). The experiments need to be carefully interpreted since large scale densification of the pores, or possible pressure sensitivity like seen in bulk metal foams can affect the measurements. We have utilized nanoindentation tests that give hardness and reduced modulus. In situ experiments on free standing samples will be also conducted. We have figured out one way to fabricate nanoporous pillars which can be used to for in-situ micropillar compression tests in the future.

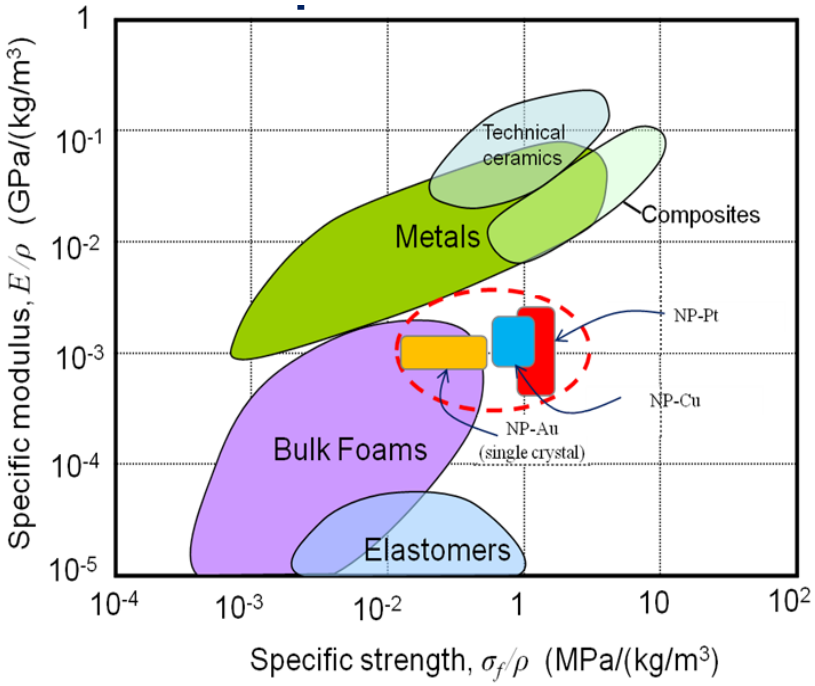

Figure 1.1 Weight-normalized stiffness (E) and strength (σ_f) for a variety of materials. The region occupied by NP metals is outside the known ranges for conventional materials. The bounds are estimated from NP Gold under a variety of tests [11, 25, 35, 36, 41-44] as well as from our results on polycrystalline NP Platinum and NP Copper that are based on combined micropillar compression and Nanoindentation measurements. Note that for metals, strength signifies the yield strength. The figure is based on Ashby (2005).

1.2.3 The effects of geometrical structure on mechanical properties

Gibson and Ashby have systematically studied how the foam properties such as modulus and strength depend on density for different types of foams. For open cell foams, the relative density relates to geometry of ligament as $\rho^* \propto (t/l)^2$ where t and l are the strut thickness and length respectively. Based on the Timoshenko beam theory, the relative foam modulus (E_f/E_s) can be found to scale with $E_f/E_s \propto (t/l)^4$ where E_f is the foam modulus and E_s is the modulus of a solid strut. The relative modulus as a function of the relative density can be expressed as

$$E_f/E_s = C_1(\rho^*)^2 \tag{1.1}$$

where C_1 is a constant related to the cell geometry. Experimental data for bulk foams gives $C_1 \sim 1$. When the individual ligament fails by plastic collapse at junctions, the relative yield strength (σ_f/σ_s) can be found to scale with $\sigma_f/\sigma_s = (t/l)^3$ where σ_f is the foam yield strength and σ_s is the yield strength of a solid strut. The relative strength can be related to the relative density via

$$\sigma_f/\sigma_s = C_2(\rho^*)^{1.5} \tag{1.2}$$

where C_2 is a constant related to the cell geometry. Experimental data for bulk foams suggest that $C_2 \sim 0.3$. For low density foams ($\rho^* < 0.1$) Eq. (1.1) agrees well with experimental measurements [45]. In contrast, validity of this scaling law has not been established for NP metal foams. Some researchers find reasonable agreement of Eq. (1.1) with experimental data (e.g.[25]), while other observe and enhancement in the modulus of NP metal foams that scales with strut thickness (e.g. [44]). We summarize in Fig. 1.2 available experimental measurements of the relative modulus and relative density for NP metal foams and compare them against the prediction of Eq. (1.1). It is immediately apparent that there exist little correlation between relative density and the relative modulus. While it is tempting to attribute the NP metal foam behavior to size effects at the nanoscale, the validity of the scaling laws themselves to NP metal foams has not been firmly established. Indeed, as we discuss in this dissertation the dependence of properties on relative density of NP metal foams occupies a different parameter space than the one occupied by bulk metal foams. As such, Eq. (1.1) may no longer be used to describe NP metal foam properties. When scaling laws for the larger relative densities have been properly established they can be used to correctly separate nanosize effects from those

due to geometry. In this work, we set out to understand why the data for the relative modulus of NP metal foam exhibit no correlation with relative density and examine whether it originates from essentially nanoscale effects or whether the scaling relationship itself needs to be modified.

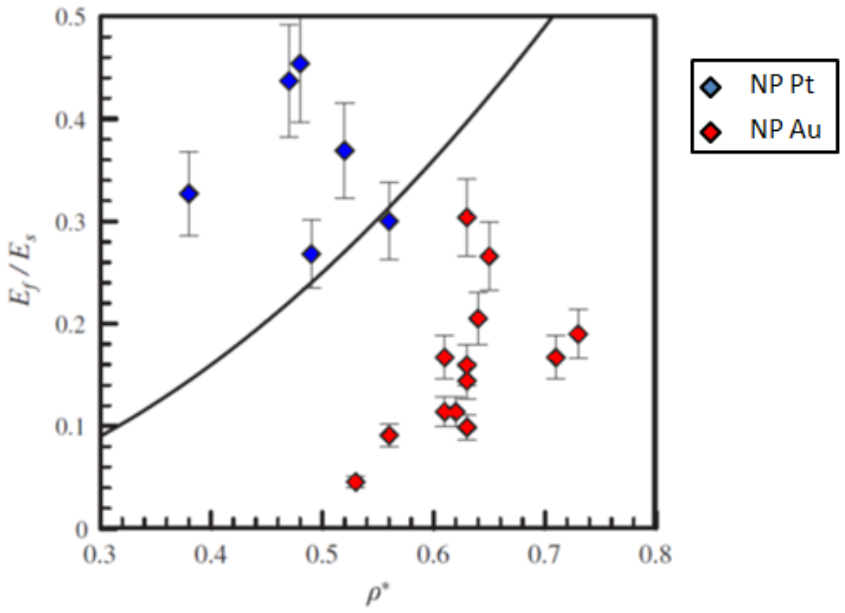

Figure 1.2 Relative modulus as a function of the relative density. The solid line represents scaling law (Eq. (1.1)). Symbols represent material systems of NP Au from the literature and our own data on NP Pt.

At relative density above 0.3, the effective bending length of beam becomes comparable to the beam thickness, leading to shorter effective bending length. As a result, individual ligament becomes more difficult to bend compared to compression or tension so that the overall deformation behavior of foams will be dominated by uniaxial yield rather than bending. Although this problem can be somewhat overcome by adding higher order terms to Eq. (1.2), compensating for the high density effects, the underlying deformation mechanism is still unclear and the accuracy of this compensation is difficult to evaluate due to the scattering of experimental data. In addition, it has been recognized

that the geometrical features of foams such as ligament orientation [40, 46], cell arrangement [40, 46, 47], and mass distribution [48] can also have significantly influence on foam properties and deformation mechanisms. Furthermore, NP metal foams have an extremely high surface area that can accommodate volumetric changes. If the ligaments are able to annihilate or accommodate defects then the durability of the material will also be enhanced.

1.2.4 The effects of internal structures on mechanical properties

It has been know that grain size have great influence on the mechanical behavior of metals. In 1950's Hall and Petch independently established that the yield strength σ_Y is proportional to the inverse of square root of grain diameter d [49, 50]. This relation can be expressed as $\sigma_Y = \sigma_0 + Kd^{-1/2}$ where σ_0 is the lattice friction stress needed to move dislocations, K is a constant. This relationship was found to have good agreement with experimental observations of materials with grain sizes in the millimeter through submicrometer regimes. However, there are still many uncertainties. First, the experiment data are quite scattered that they can be used to support either $d^{-1/2}$ or d^{-1} [51, 52]. Second, it is difficult to prove the validity of the Hall-Petch relationship for nanostructure materials with grain size about tens of nanometers. The inverse Hall-Petch effect was first proposed by Chokshi et al. and has been observed experimentally in nanocrystalline materials when the grain sizes below 25nm [53, 54]. It has been suggested that plastic deformation at this case is no longer dominate by dislocation motion but by atomic sliding of grain boundaries [54]. Third, the presence of large amount of free surface or grain boundaries, serving as sinks or sources of dislocations, would undoubtedly affect their mechanical properties. Although the Hall-Petch model based on pile-up effects

accommodates the experimental data well, there remains a lack of direct evidence to support this hypothesis. In the analysis of NP metals, the strut strength is typically inferred by properly accounting for the effect of geometry on properties. Such analysis can only be used to place reasonable bounds for the properties of NP metal struts. While not a direct measurement, such bounds are helpful in assessing the effects of internal structure on the foam properties.

1.3 ***Experimental Methodologies employed in this work***

1.3.1 Synthesis techniques

In this work, we synthesize NP metal foams of NP Pt and NP Cu by dealloying amorphous binary silicides e.g. Pt-Si and Cu-Si respectively. In order to impede crack formation during dealloying, our amorphous films were deposited under residual compressive stress. During dealloying, silicon is preferentially dissolved in the electrolyte leaving behind the more noble species (Pt or Cu) to assemble into a three dimensional network of struts. As synthesized NP Pt is in the range of 4-10 nm and as synthesized NP Copper has struts in the range of 20-30 nm. Subsequent annealing can increase the strut dimensions.

1.3.2 Chemical composition and structural characterization

The NP metal structures were observed under a scanning electron microscope (SEM) where the relative density, and strut dimensions were obtained. A select number of samples were observed under Transmission Electron Microscope (TEM). TEM confirmed that the initial alloy was amorphous and that the NP Pt and NP Cu were

polycrystalline with grains equal to the strut thickness [28]. The composition of the amorphous films was determined by Rutherford backscattering spectrometry (RBS).

1.3.3 Nanoindentation

The mechanical properties of NP metals of different morphologies were characterized using a Triboindenter (Hysitron) equipped with a Berkovich tip with radius of ~150 nm. Nanoindentation is a well-established technique for assessing material properties of materials at the nanoscale. However, several factors can influence the measurements of the modulus during indentation.

1) If a small number of cells are sampled by the indenter, the modulus tends to be underestimated. It has been demonstrated that for low density porous materials, testing a minimum of five cells in each direction is necessary to properly measure the modulus [55, 56]. On the other hand, if the indentation depth is too high, large scale densification can give an increase in the modulus. In our tests of nanoporous metals the modulus was obtained by averaging measurements up to an indentation depth of 100-150nm (i.e. within 5-8 cells). Simple estimates utilizing existing models of indentation show that this procedure may underestimate the modulus by up to 30%.

2) An equally challenging problem in testing thin film is properly accounting for the influence of a stiff substrate, which results in an overestimate of the modulus. For fully density thin films the substrate effect is corrected using different models that account for the strain mismatch across the interface of thin film and substrate [57-59]. However, the substrate effect in nanoporous films cannot yet be corrected using the above techniques since the modulus of NP foams is not constant with indentation depth.

In order to make a qualitative assessment of the substrate effect, we employed the technique described in Refs. [57, 58] to analyze the NP Pt data by assuming that Poisson's ratio is zero and the modulus remains a constant throughout the indentation process. In this scenario we find that the substrate can cause the NP Pt modulus to be overestimated by up to 30%. In order to measure film-only properties, the reported modulus is obtained from indents within 10% of the overall foam sample thickness to eliminate substrate effects. Because the substrate effects are weaker for plastic deformation, the reported hardness is the average hardness obtained from unloading curves of indents with indentation depth within 30% of the overall foam sample thickness and equivalent to two to five pore sizes so as to avoid underestimating the hardness at shallow depths.

3) For open cell foams with relative density smaller than 0.3, the plastic deformation usually fully converts to densification of the overall foams and the plastic Poisson ratio is ideally zero. The hardness of the foam, H is simply $H = \sigma_f$ [60, 61]. As the effective Poisson ratio increases, the hardness increases from σ_f to $3\sigma_f$ [40]. Recent studies on NP metals show that lateral expansion occurs during pillar compression testing, indicating plastic a nonzero value of $v_p \sim 0.2$ [41]. In addition, by comparing the hardness value to the yield strength directly from uniaxial compression test, $H = 3\sigma_f$ agree wells with experimental data [62]. To data there is no theoretical solution for the effect Poisson ratio but because of the high density of NP metals compared with traditional bulk foams, it should be safe to conclude that the hardness of NP metal, H should be 2 to 3 times larger than its yield strength, σ_f.

4) Residual stresses (compressive) can overestimate the modulus [63]. The amorphous alloy in our work is under compressive stress but after dealloying the residual compressive stress decreases significantly. For very small levels of residual stress, the modulus may change within a few percent. We therefore anticipate that residual stresses have a negligible influence on the modulus measurements of NP Pt foams.

1.3.4 Substrate curvature method

An estimate of the residual stresses before and after dealloying was obtained from an in-house laser scanning system. The residual stress inside thin film can be influenced by the Argon ion energy, chamber pressure, substrate temperature, and film thickness. The results from our in-house installed instrument are validated with a Profilometer NT3300. The curvatures before and after sputtering were measured and calculation from the Stoney formula shows that compressive stress from 150 MPa to 250 MPa for Cu-Si thin films after sputtering. In addition, the change in curvature as a function of dealloying time was obtained. The residual stress decreases to $\leq$ 50 MPa at the end of dealloying.

1.3.5 Micropillar fabrication and tests

Micropillars that are 3um height, 5um diameter with aspect ratio about 0.375 were fabricated using focus ion beam (FIB). The low aspect ratio can largely avoid the error induced by misalignment between the loading axis and the of axis pillar. We have also tried with lithographic patterning and sputter deposition to fabricate patterns such as pillars and trenches. The mechanical response of those pillars will be measured using insitu compression tests in the SEM.

1.4 ***Thesis Organization***

This section describes how the thesis will be organized in the following five chapters.

Chapter 1 illustrates the background knowledge of synthesis techniques and experimental methodologies employed in this works.

Chapter 2 presents a relationship between shrinkage, relative density, and atomic fraction is proposed and experimentally verified. The relationship can be used to obtain remnant atomic fraction from SEM images: one before and one after dealloying. It also can be used to predict shrinkage during dealloying.

Chapter 3 presents a modified scaling equation for the dependence of relative density and relative stiffness on the geometric parameters such as strut thickness (*t*) and length *(l)* and junction size (*d)*. We found agreement between our model and NP Au data and show that the enhanced properties are mainly due to the geometrical effects.

Chapter 4 presents our study on mechanical properties of nanocrystalline platinum using both experimental methodology and MD simulations. The hardness decreases with decreasing average thickness of the struts, but the dependence on aspect ratio (*t*/*l*) is much weaker than the expectations drawn from a simple dimensional analysis. Many other parameters controlling properties of NP metals such as strut diameter and grain siz may be influenced by the synthesis mechanism, their identification will pave the path for informed design of NP metal with desirable characteristics.

Chapter 5 presents our synthesized NP Cu that exhibits a sixty-fold increase in foam strength when compared to the report in literature. The inferred strut strength greatly exceeds yield strength of bulk copper and compares well with other nanostructured systems. These results suggest that the internal structure of struts is at least partially responsible for the observed increase in strength of foam.

Chapter 6 presents the morphology of NP Cu can be controlled by the applied potential during dealloying. The relationship between applied potential, dealloying rate and grain growth were discussed. A simple hypothesis was proposed to explain the evolution of morphology of NP Cu during dealloying. Different models were employed to study the dependence of properties on strut thickness and relative density of NP Cu.

Chapter 7 presents a technique that can abstract material properties from nanoindentation with a flat-ended cylindrical indenter. I compared the Hertz theory and FEM models to study the slope of Young's modulus and effective modulus during compression test. The comparison between elastic and elastic perfectly-plastic models reveal the moment when plastic deformation occurs. Then, a model was developed for the nanoindentation test carried on NP Cu. This model was validated with DIC analysis using SEM micrographs. In the future work, more refined model can be established to count the effects of undercutting and establishment of contact.

Chapter 8 summarizes all results and presents recommendations for future work.

CHAPTER 2

A RELATION BETWEEN RELATIVE DENSITY, ALLOY COMPOSITION AND SAMPLE SHRINKAGE FOR NANOPOROUS METAL FOAMS

2.1 ***Introduction***

Nanoporous (NP) metal foams are characterized by high surface-to-volume ratios. We focus on NP metals synthesized by dealloying, a controlled corrosion process that causes less noble element in an alloy to dissolve in an electrolyte while the remnant element self assembles into a three dimensional network of struts. The relative density, i.e. $\rho^* = \rho_{NP\ metal}/\rho_{solid\ strut}$, the ratio of NP metal density to solid strut density, is equal to the volume fraction occupied by the solid in a porous medium. In studies of NP metals synthesized by dealloying it has been sometimes assumed that the relative density is equal to the atomic fraction that remains after dealloying. However the volume of the assembled structure may be different from the volume of the initial alloy. These inherent dimensional changes can be as high as 72% [64] and need to be taken into account in the estimates of relative density. While some researchers have recognized that these quantities are related [35, 65] there exist conflicting reports in the literature that simply equate relative density of NP metals to the remnant atom fraction. Extensive studies on bulk metal foams [40] have shown that such properties as stiffness, strength, etc., scale only with relative density. If shrinkage effects are ignored, then the relative density will be underestimated, leading to incorrect estimates of weight-normalized properties. For

example, mechanical properties will appear enhanced and can be misconstrued as size effects when NP metal foams are compared to bulk metal foams. In the following descriptions we understand density to mean the number density, $\rho = N/V$, which is the number of atoms N constrained in a control volume V. in this paper, we propose and experimentally verify a relation between relative density, the dimensional change and remnant atomic fraction. Apart from its significance for correct estimates of relative density, such relation could be useful in other context. For example, in MEMS device design using NP metals, it may be desirable to know a priori how much a sample will shrink during dealloying to ensure compatibility with other components. We note that, in general, dealloyed samples decrease in volume, but expansion has also been observed [66]. In this paper, we assume that the sample shrink.

2.2 ***Experimental Methodology***

We synthesized NP Pt by dealloying amorphous (Pt_xSi_{1-x}, where x=0.1, 0.2, 0.35 atomic fraction) under varying amounts of residual compressive stress to ensure limited crack formation during dealloying [28]. Our previous work has demonstrated that the state of the initial alloy can affect silicon removal and NP Pt assembly during dealloying, causing the formation of isotropic and anisotropic (Voronoi and columnar) morphologies as shown in Figure 2.1.

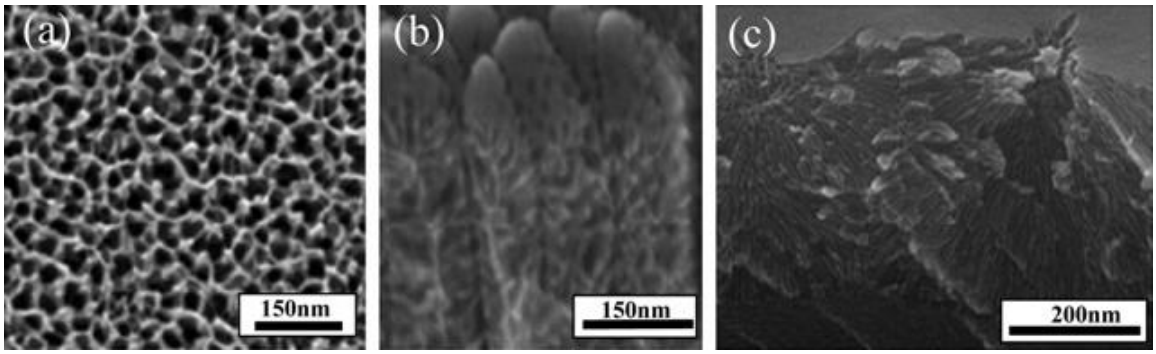

Figure 2.1 SEM micrographs of NP Pt foam showing different morphologies. (a) Plan view of the open cell. (b) 45^0 tilt-view of the columnar type. (c) 45^0 tilt-view of the Voronoi type.

Samples were dealloyed in an electrochemical cell. A range of densities was obtained by changing the externally applied voltage (V) from 0.3 to 0.9 V as documented elsewhere [10, 13, 67, 68]. All but one side of each sample was coated with a thin polymeric film that did not react with the hydrofluoric acid.

We obtained the thickness change and the relative ndensity using properly focused and processed electron micrographs in a procedure that is outlined in Liu et al. [69]. We find that the relative density measured from stereographic projections and Rutherford backscattering spectrometry (RBS) are in good agreement as long as high-quality SEM micrographs are used.

2.3 ***Model derivation***

We assume that the initial alloy is a rectangular solid with dimensions lwh containing a total of N atoms. During dealloying, atoms will selectively dissolve in the electrolyte and an NP structure will form. This is accompanied by overall dimensional changes, i.e., the resulting structure occupies less volume than the initial alloy. The assembled NP structure will have N' atoms and will occupy a rectangular solid with

dimensions $(l-\Delta l)(w-\Delta w)(h-\Delta h)$. The NP structure itself will consist of a threedimensional network of struts.

We compare the ratio of number density of the initial alloy to the number density of the NP structure to quantify both volumetric and atom population changes during dealloying. Let

$$\frac{\rho_{initial\ alloy}}{\rho_{NP\ metal}} = \frac{1}{\alpha}\left[\frac{(l-\Delta l)}{l}\frac{(w-\Delta w)}{w}\frac{(h-\Delta h)}{h}\right] \tag{2.1}$$

where $\alpha = N'/\mathrm{N}$, is the ratio of total atoms in the NP metal to the total atoms in the initial alloy. For certain systems, e.g. $\mathrm{Pt_xSi_{1-x}}$, where one element (Si) completely dissolves [29], α will be equal to x, the Pt atom fraction. In other systems, e.g. $\mathrm{Au_xAg_{1-x}}$, where a small amount of Au dissolves in the electrolyte and a small amount of Ag remains[26, 70, 71], α will be a combination of Au and Ag atoms. In those cases, the the relation between remnant fraction, shrinkage and relative density derived below can be used to determine α.

The number density ratio in Eq. (2.1) can also be written in terms of the relative number density ρ^*, i.e. the percentage of solid in a porous medium as:

$$\frac{\rho_{initial\ alloy}}{\rho_{NP\ metal}} = \frac{\rho_{initial\ alloy}}{\rho^*\ \rho_{strut}} = \frac{\beta}{\rho^*} \tag{2.2}$$

where $\beta = \rho_{initial\ alloy}/\rho_{strut}$ is a factor describing the differences of the internal structure between the initial alloy and the strut. For example, if both the initial alloy and the strut are crystalline with face-centered cubic (fcc) structure and the constituent elements of similar sizes, the ratio $\beta = 1$. This is the case for the $\mathrm{Au_xAg_{1-x}}$system, where x is the atom fraction. On the other hand, the $\mathrm{Pt_xSi_{1-x}}$ alloy is amorphous while resulting

foam has nanocrystalline with fcc structure. The number density of the amorphous alloy is variable and depends, for example, on deposition conditions, such as sputter bias or pressure. However, since both Pt and Si atoms have comparable diameter, we expect that for Pt_xSi_{1-x}, $\beta \approx 1$ within a few percent. Detailed studies on the density of amorphous silicon have found that it is within 2% of crystalline silicon [72]. Note that β in Eq. (2.2) is defined as the ratio of the number densities. In principle all of the calculations can be reformulated in terms of the mass density, but the meaning and values ofα and β will change.

Eqs. (2.1) and (2.2) can be combined to relate macroscopic dimensional change to the relative density $\rho *$, a composition-dependent ratio a and a structuredependent ratio β. For simplicity, we assume that the change along two directions will be proportional to the change in another. This assumption is not necessary but simplifies the equations. If height (film thickness) is the independent variable, then: $\frac{\Delta l}{l} = \frac{\Delta w}{w} = K\frac{\Delta h}{h}$, where K is a proportionality constant. For K = 0, shrinkage is limited to one dimension, e.g. the film thickness, and when K = 1, dimensional change occurs equally along all directions. The through-thickness shrinkage ratio becomes:

$$\Delta h/h = \begin{cases} 1 - \alpha\beta/\rho^*, & K = 0 \\ 1 - (\alpha\beta/\rho^*)^{1/3}, & K = 1 \end{cases} \quad (2.3)$$

For our Pt_xSi_{1-x} thin film, the thin polymeric layer will limit dimensional change along two directions, but will not completely prevent it.

2.4 ***Results and Discussion***

Figure 2.2 shows a plot of shrinkage ratio through the thickness, $\Delta h/h$, as a function of the ratio of remaining atom fraction to relative density, α/ρ^*. The solid lines show model predictions based on Eq. (2.3) for structures with same strut and initial alloy morphology ($\beta = 1$). Experimental data for NP Pt foam of different morphologies ($\beta \approx 1$) are plotted on Figure 2.2. The error bars on the experimental measurements represent an average of three to four data points that are binned within 5% of their α/ρ^* value. In addition, Fig. 2.2 include open cell NP Au sample from the literature that are summarized in a Table found in supplemental material [39, 64, 65, 73, 74]. For NP Au sample the relative density was obtained using SEM images included in each article with the exception of [65].

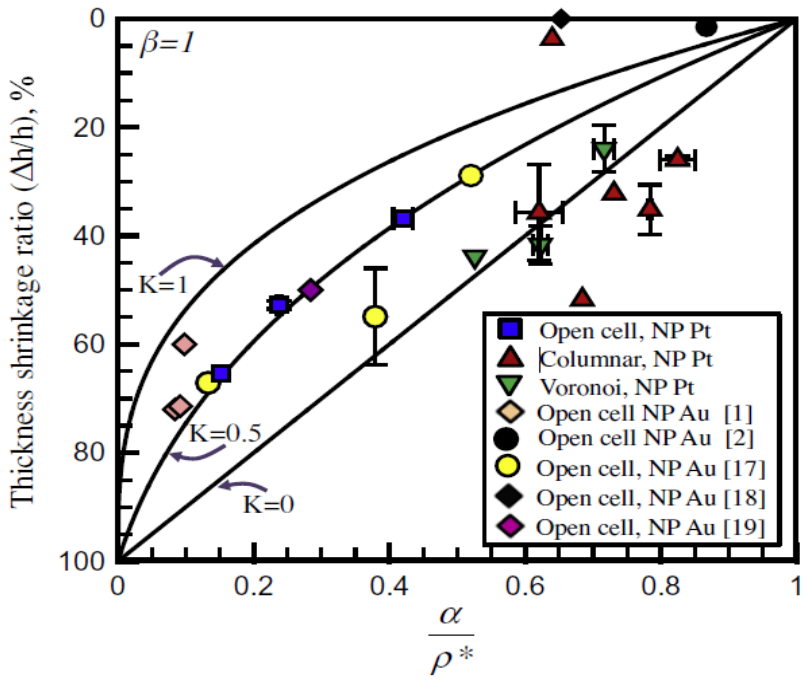

Figure 2.2 Through thickness shrinkage ratio (dh/h) as a function of the atom fraction to relative density ratio (α/ρ^*) for different morphologies of NP metal foams with *β=1*.

Overall, we find good agreement between the experimental observations and the model predictions. The transversely isotropic structures i.e. columnar and voronoi (see Figure 2.1) agree well with the model that describes dimensional change along one direction, e.g. the thickness ($K = 0$). Closer inspection of the structures before and after dealloying can help explain this. For the columnar type NP foam each column boundary divides the width and length of the thin film into smaller segments of ~100 nm. Any shrinkage that occurs in the lateral direction (i.e. along width and length of the thin film) will be accommodated by enlarging the gap between columnar boundaries. Our measurements indicate as much as 6% shrinkage occurs in the diameter of columnar boundaries after dealloying. This local change in lateral dimensions is enough to form NP metal foam without any apparent macroscopic lateral changes in dimension. The same observation is true for voronoi type NP foam where concave features form on the free surface as the dealloying front progresses in a radial fashion through the thickness [10]. The depth of the concave features is large enough to locally relax the surface so that there is little apparent lateral shrinkage in the film. Therefore, local relaxation in the form of columnar boundaries or surface perturbations causes these anisotropic structures to conform to the model that describes dimensional changes occurring only along the thickness direction.

On the other hand, the experimental measurements of open cell NP metal foams agree well with models that allow through thickness and in-plane shrinkage. In particular, the experimental measurements agree well with the model prediction for $\beta = 1$ and $K = 0.5$, as seen in Figure 2.2. The samples we synthesized are thin films with typical through thickness dimensions of 1-10 μm and in-plane dimensions of ~0.5-1 cm. Closer

inspection of the edges of the samples that were coated with a thin polymeric film revealed that a certain amount of undercutting has occurred and NP foam formed underneath a finite region of the polymeric film. The apparent macroscopic change of ~20% in the in-plane direction of the film arises from a certain degree of undercutting near the perimeter of the sample. This lateral change may have also been accommodated by porosity adjustments of the sample.

Experimental observations from the literature also agree very well with the model predictions. In particular we draw attention to the reconstructed 3D NP foam specimen work using electron tomography in the work of Rösner et al. [28, 65]. In that work, the authors accounted for all dimensional changes and used the finite volume of NP metal to obtain relative density. We find that their observations agree well with the sterographic projection technique we used to obtain relative density and their measurements agree with our model predictions. We expect free standing samples of NP metal foams synthesized from isotropic alloys to closely follow the model predictions for K=1 in Eq. (2.3).

The maximum relative density for an NP metal synthesized by dealloying occurs when there is no volume change from the initial alloy such that $\rho^* = \alpha$. Due to shrinkage $\rho^* > \alpha$, with density values commonly in the 50-70% range and $\alpha = 10 - 35\%$ for systems examined in the literature. Thus a simple assumption of $\rho^* = \alpha$ underestimates the density by a factor of 2-7. Based on scaling arguments, properties such as the relative foam modulus or conductivity, scale linearly with ρ^*. Other foam properties, such as relative yield strength, $\sigma_{NP\ metal}/\sigma_{sollid\ strut}$, scale with $(\rho^*)^{3/2}$ [40]. The errors in measurements of relative density can lead to a factor of 18 errors in the relative yield

stress! Such apparent enhancements in properties of NP metal foams can be misconstrued as size effects for struts in the nanoscale. It is therefore essential to obtain correct estimates of density by accounting for any shrinkage in the samples.

In order to examine the effects of sample shrinkage when the system is constrained from undergoing dimensional changes, we consider the following simplified scenario. Suppose the sample needs to undergo a dimensional change in one direction of the order of $dh/h \sim 35\%$. The stress required to prevent this change from occurring can be estimated as $\sim\sigma\sim E'(dh/h)\sim$15GPa where E' is the biaxial modulus of NP metal. Clearly such excessive stress cannot be sustained. In order to prevent its buildup, the system can self-assemble into a structure of lower relative density. However, experimental evidence suggests that allowed variations in density are limited and the excessive stress build-up is frequently relieved by mechanisms related to boundary changes, such as free surface perturbations, relaxation of inner boundaries (e.g. boundaries between columns in the columnar foam), or formation of surface cracks. Note that formation of cracks has until recently been a major unsolved problem in synthesis of NP metal foams. Remarkably, the recently proposed solutions, e.g. gentle dealloying [39], introduction of compressive stresses [28] or control over dealloying rate [75], may in fact allow the sample to undergo the necessary dimensional changes. This suggests that the dynamics of the dealloying and self-assembly processes play an important role in deciding between the two possibilities. A schematic of the possible modes a material may undergo to alleviate stress build-up is shown as part of the Supplementary material.

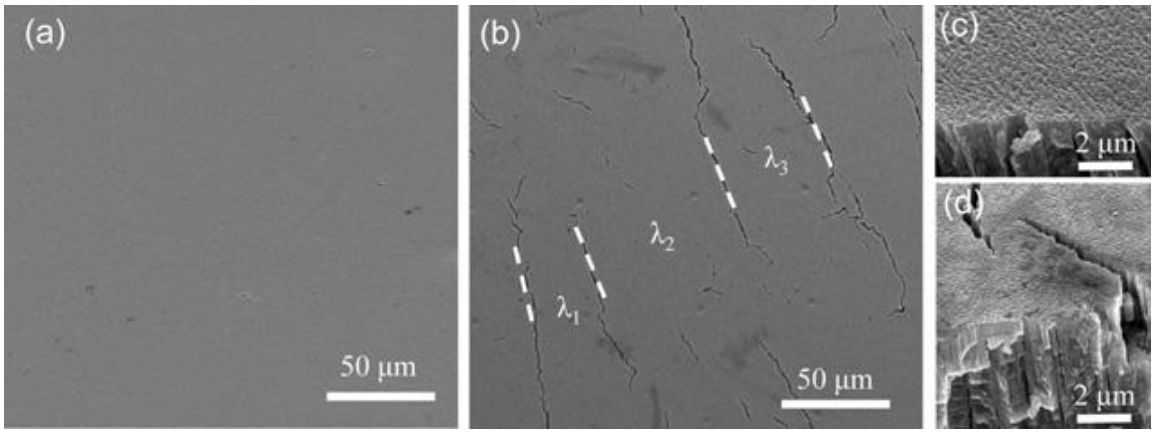

Figure 2.3 SEM plan views of columnar type NP Pt with α/ρ^{*}=0.6 and (a) dh/h~0.4 (b) dh/h~0.04. SEM tilt views of same samples with (c) dh/h~0.4 and (d) dh/h~0.04 showing that parallel cracks penetrate only halfway through the film thickness.

All of the samples in our work were synthesized from initial alloys with residual compressive stresses and generally showed no cracks. However, macroscopic cracks were observed on the free surface of two samples with the least amount of imposed residual compressive stress. Figure 2.3 shows SEM top and side views for two NP Pt samples with columnar morphology obtained from initial alloys with different levels of residual compressive stress that were dealloyed at the same high rate of 10 nm s^{-1}. The two samples have similar $\alpha/\rho * \sim 0.6$ but differ in the amount of dimensional change they have undergone: one exhibited a through-thickness change of 40%, while the other exhibited a change of 4%. The sample that has undergone minimal shrinkage exhibited a large density of macroscopic parallel cracks with average spacing of $\sim$35 μm as seen in Figure 2. 3(b) and (d).

Analysis of linear elastic isotropic films on substrates with same elastic mismatch has shown that there is a minimum crack spacing λ_{min} below which more parallel cracks cannot initiate. Following analysis of Tada et al. [76], we estimate

$$\lambda_{min} \approx -3h \log\left(1 - \frac{E'\Gamma}{2\sigma^2 h}\right) \quad (2.4)$$

where E' is the biaxial film modulus, Γ is the fracture energy of the film, σ is the mismatch stress and h is the thin film thickness. Since Γ is not known for NP metals, we estimate λ_{min} for three values of Γ representative of brittle (Γ = $1\ J/m^2$), moderate (Γ = $100\ J/m^2$),), and high-toughness materials (Γ = $10^4\ J/m^2$),). For a λ_{min}~$35\ \mu m$ the levels of mismatch stress that are needed to initiate parallel cracks simultaneously is 60 MPa for brittle, 600 MPa for intermediate and 6 GPa for high-toughness materials. Such stresses can easily form during the dealloying process. The fact that the network of parallel cracks did not penetrate through the entire thickness of the NP Pt sample (Fig. 2.3(d)) indicates that the combination of mismatch elastic properties and fracture toughness between the initial alloy and NP foam do not favor progression of cracks to the interface. This analysis shows that even if a material may have the tendency to form surface cracks their catastrophic progression through the entire film length can be averted by careful tuning of the initial alloy properties. In our work we have synthesized open-cell NP metal foams that have more than 60% shrinkage without forming any surface cracks. Our model can help differentiate between modes described above (see Figure in the Supplementary material).

As a final note, we point out that the mere fact that substantial dimensional changes occur under most conditions has interesting implications for understanding of dealloying and subsequent self-assembly of NP metal foams. Indeed, it is frequently assumed that dealloying and self-assembly occur in a narrow (a few atomic layers) near-surface region. It is hard to envision how a substantial dimensional change could occur under this constraint. Instead, self-assembly appears to proceed in a finite near-surface

region with thickness that must be at least comparable to the internal length scales of the foam (e.g. the size of pores, struts: 10 nm or above).

2.5 ***Conclusions***

In summary, we have presented a relation between sample shrinkage, relative density and remnant atomic fraction that agrees well with experiments. The relationship can be used to obtain the remnant atomic fraction from two tilt-view SEM images: one before and one after dealloying. This is particularly important in cases when the remnant atom fraction consists of more than one element and thus cannot be directly equated to the initial alloy composition.

CHAPTER 3

A RELATIONSHIP BETWEEN THE GEOMETRICAL STRUCTURE OF A NANOPOROUS METAL FOAM AND ITS MODULUS

3.1 ***Introduction***

Nanoporous (NP) metal foams possess high surface to volume ratios and show great promise as components of fuel cells [4, 77], as sensors and have been suggested for use in biological applications, for example as antimicrobial scaffolds [37] or platforms on which to explore biological material behavior [78]. NP metal foams are often synthesized by dealloying where the less noble elements in an alloy are selectively dissolved in the electrolyte leaving behind the more noble elements to self assemble into struts in the range 2-100 nm [4, 18, 19, 37, 79]. The struts are interconnected in space forming open cell foam.

At present, the structure-property relationship of NP metal foams is not well understood. For open cell foams of low density, such relationships have been examined using dimensional analysis [28, 40, 45, 80]. For example, the relative density, i.e. the solid fraction of the foam, relates to strut geometry as $\rho^* \propto (t/l)^2$ where t and l are the strut thickness and length respectively. In turn, the deformation of a single strut can be used to obtain information of the collective foam response. For example, under the assumption that a strut deforms mainly in bending, the relative foam modulus (E_f/E_s) can be found to scale with $E_f/E_s \propto (t/l)^4$ where E_f is the foam modulus and E_s is the

modulus of a solid strut. By noting that both the relative modulus and relative density are functions of the same geometric parameters, it has been shown that

$$E_f/E_s \propto (\rho^*)^2 \tag{3.1}$$

For low density foams ($\rho^* < 0.1$) Eq (3.1) agrees well with experimental measurements [45]. In contrast, validity of this scaling law has not been established for NP metal foams. Some researchers find reasonable agreement of Eq. (3.1) with experimental data (e.g.[25]), while other observe and enhancement in the modulus of NP metal foams that scales with strut thickness (e.g.[44]). To further illustrate this point, we summarize in Figure 3.1 available experimental measurements of the relative modulus and relative density for NP metal foams and compare them against the prediction of Eq. (3.1). It is immediately apparent that there exist little correlation between relative density and the relative modulus.

In principle, the deviation of the observed properties of NP metal foams from simple scaling relations of the type Eq. (3.1) may be expected. While NP metal foams possess some similarities with open cell foams at larger length scales, their properties are expected to be greatly influenced by the nanoscale size of their geometrical features (e.g. struts and pores). For example, the free surfaces in NP metals may be expected to be energetically important, hence playing a bigger role in controlling the properties of the foam compared to bulk foams [9, 81]. In addition, the free surfaces may serve as sources and sinks for defects. Another complexity may arise when nanosized geometrical features are the same scale as the material internal scales, e.g. grains [82].

While it is tempting to attribute the NP metal foam behavior summarized by Fig. 3.1 to size effects at the nanoscale, the validity of the scaling laws themselves to NP metal foams has not been firmly established. Indeed, as we discuss in this paper the relative density of NP metal foams is $\rho * > 0.4$ and occupies a different parameter space than the one occupied by bulk metal foams. It is important to establish scaling laws for the larger relative densities so as to correctly separate nanosize effects from those due to geometry. In this paper we set out to understand why the data for the relative modulus of NP metal foam exhibit no correlation with relative density and examine whether it originates from essentially nanoscale effects or whether the scaling relationship itself needs to be modified (see Section 4 for details).

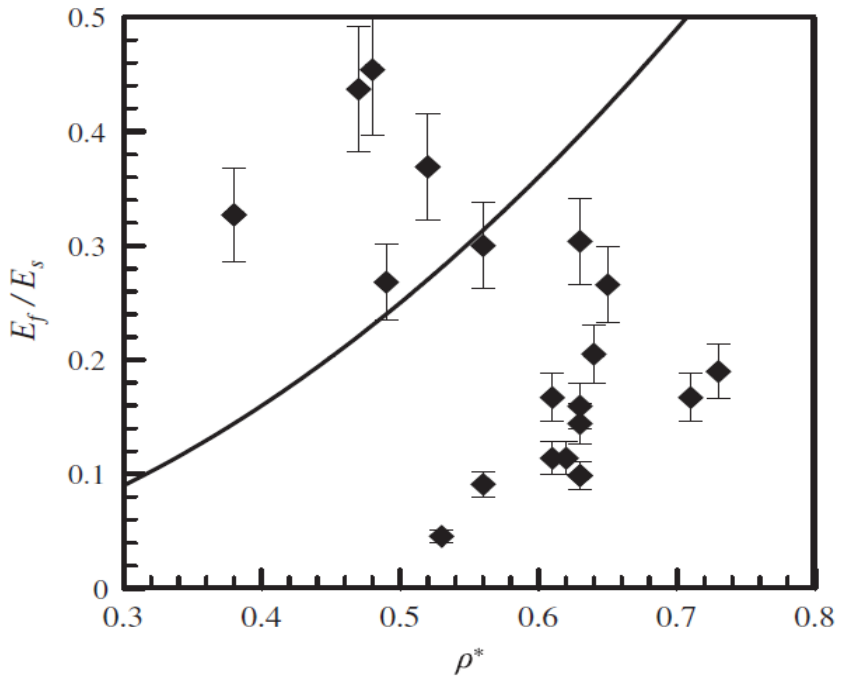

Figure 3.1 Relative modulus as a function of the relative density. The solid line represents scaling law (Eq. (3.1)). Symbols represent material systems of NP Au and NP Cu from the literature and our own data on NP Pt. Details of the experimental measurements can be found in Sections 3.2 and 3.3. The data are summarized in Tables 3.1 and 3.2.

In a recent work we demonstrated that inherent dimensional changes (shrinkage) occur during synthesis of NP metals by dealloying and may lead to underestimation of their relative density and thus erroneous correlation with properties. In this work we measure relative density using stereographic projections from electron micrographs and validate these measurements using Rutherford Backscattering Spectrometry (RBS). We also use the micrographs to obtain statistical information on the strut geometry (strut diameter, length etc). This allows us to closely examine the relation between relative density and strut geometry and hence the origin of the scaling relationships. We find surprisingly that the simple dimensional analysis derivation where $\rho^* \propto (t/l)^2$ does not describe the behavior of NP metal foams especially for low *t/l* ratios. Closer examination of NP metal structure reveals a possible cause for this discrepancy, namely agglomeration of mass at junctions.

We propose a modification to the dimensional analysis that includes a correction for mass agglomeration. We use this simple model to obtain an expression for the scaling of NP metal modulus with strut geometry. We note that the effect of mass agglomeration at junctions has been studied for low density foams using finite elements and was found to have little effect on the modulus [83]. In our analysis, we find that this effect becomes considerable for large t/l ratios and may lead to a 100% increase in modulus. We find good agreement between the model and experimental observations for single crystal NP metal samples with large junctions and large strut thickness. We then compare the modified scaling relationship to the measurements of modulus in more complex NP metal foams that have nanosized grains within the struts. We find that the observed relative modulus is greatly enhanced compared to the model prediction. This strongly indicates

that the enhancement of the relative modulus in these cases is not a geometric effect, but rather can be attributed to the effects of the internal structure.

This paper is divided into the following parts: Section 3.2 is a description of the experimental protocol followed for the relative density and modulus measurements for NP metal foams. Sections 3.3 and 3.4 present the results for relative density and the modulus as a function of thickness to strut ratio respectively.

3.2 ***Experimental Methodology***

We synthesized open cell NP Platinum (Pt) foam for a range of densities and examined the strut morphology. The sample preparation procedure and the characterization techniques are presented here. In addition to our own measurements, we include results that have been reported in the literature by utilizing published micrographs to obtain the relative density and strut characteristics. In this paper, density will always refer to the number density $\rho = N/V$, which is the number of atoms (N) contained in a control volume (V). We also define the relative density, $\rho^* = \rho_{NP\ metal}/\rho_s$, as the ratio of the average density in the assembled NP structure to the density of a solid strut. Relative density is a geometric parameter that quantifies the solid fraction in a porous medium. A brief summary of the synthesis procedure has been given in Ref. [69]. We present additional details here.

3.2.1 Sample synthesis

The initial alloy used in our work is amorphous platinum silicide that is co-sputtered using physical vapor deposition (PVD) method on (100) Silicon wafers. Different compositions of amorphous films were deposited (Pt_xSi_{1-x} where x=0.1, 0.2,

0.35) for two different thicknesses (1 μm and 10 μm), and sputtering conditions (0 V, 100 V, 300 V bias) [82]. Our amorphous films were deposited under varying amounts of residual compressive stress to ensure limited crack formation during dealloying. In this paper we examine only open cell structures.

The dealloying of the amorphous platinum silicide was done in 3% hydrofluoric acid in distilled water. A three electrode system consists of the initial alloy as the working electrode, a Pt counter electrode and a saturated calomel electrode (SCE) that acted as reference electrode. In order to produce samples with a range of relative densities, the externally applied voltage (V) ranged from 0.3 to 0.9 V. It has been well documented that a change in the externally applied voltage can produce changes in the morphology of the NP metal foam [10, 67, 68, 84]. To eliminate delamination of the thin film at the substrate/amorphous alloy interface, all but one side of each sample was coated with a thin polymeric film that did not react with the hydrofluoric acid.

3.2.2 Sample Characterization

The strut length and diameter were experimentally obtained from tilt images from several different locations and various magnifications of the dealloyed samples using a Zeiss Ultra 60 Scanning Electron Microscope (SEM). Representative samples before and after dealloying were also observed under a FEI Tecnai F30 Transmission Electron Microscope (TEM) to corroborate the strut dimensions that were measured from tilt SEM views and to describe the microstructure. TEM verified that the initial alloy was amorphous and that the resulting NP Pt foams were polycrystalline with 5 nm sized grains regardless of deposition or dealloying conditions [82].

In our dealloying experiments Si is completely removed [29], so that the remnant atom fraction α is determined by the initial alloy composition. For a selected number of samples, we have verified this by measuring α using Rutherford Backscattering Spectrommetry (RBS) as described below. RBS experiments were performed at the Ion Beam Laboratory (IBL) at Los Alamos National Laboratory (LANL) [85]. For most measurements a 3MeV ^{4}He beam was used. The samples were oriented at an angle with the incoming beam to avoid channeling effects on the substrate signal. For each thin film the experimentally obtained spectrum was compared to numerical simulations (RUMP) [86, 87] to provide either the atomic composition of the film or the atom density [88, 89]. The atomic composition was obtained by comparing the relative signal heights of the Silicon and Platinum spectra that are part of the Pt_xSi_{1-x} alloy [29]. The initial alloy composition for the samples that we synthesized varied from 10-37% [82]. RBS confirmed that during dealloying of the amorphous silicide, silicon is completely removed leaving behind only Pt to self assemble [29]. There are variations in the signals between experiment and simulation and in particular the tail end of the Platinum peak in experiments does not exhibit sharp step-wise drop. We use the extrema of the Platinum peak tail as estimates for the uncertainty in the density measurement (~2%).

The relative density ρ^* was obtained from further processing of the SEM images (see section 3.1). The density of a select number of NP Pt foam structures was found by combining RBS spectrum analysis with film thickness measurements from the tilt-view micrographs. For the density measurements only thin films were used (~1μm) to limit signal overlap between the platinum and silicon peaks. The density can be obtained by comparing the energy difference (ΔE) between backscattered particles from the free

surface of the thin film and backscattered particles from the foam/initial alloy interface. This energy difference relates to the film thickness and the atom density through, $\Delta E = [\varepsilon]\rho t$ where $[\varepsilon]$ is the stopping cross section factor, ρ is the density and t is the film thickness. The atom density is determined by combining energy difference using RBS with the film thickness measurement using SEM. The relative density is obtained by dividing the atom density to the atom density of dense platinum. The relative density from RBS measurements was compared to the measurements using stereographic projections (see Section 3).

3.2.3 Nanoindentation

The mechanical properties of open cell NP Pt foam of different morphologies were obtained via nanoindentation using a Triboindenter (Hysitron) equipped with a Berkovich tip. The indentations were performed on the free surface of the as synthesized samples under displacement control. To eliminate substrate effects, the maximum indenter displacement was within 10% of the overall foam sample thickness. For each sample 50 indents were performed that were 40 μm apart. The reduced stiffness of each sample was obtained from the unloading curve following the procedure outlined by Oliver and Pharr [90, 91].

Nanoindentation is a well-established technique forassessing mechanical properties of materials at the nanoscale. However, several factors can influence the measurements of the modulus during indentation:

1) If a small number of cells is sampled by the indenter, the modulus tends to be underestimated. It has been demonstrated that for low density porous materials, testing a

minimum of five cells in each direction is necessary to properly measure the modulus [55, 56]. On the other hand, if the indentation depth is too high, large scale densification can give an increase in the modulus. In our tests of NP Pt the modulus was obtained by averaging measurements up to an indentation depth of 100 – 150 nm (i.e. within 5 – 8 cells). Simple estimates utilizing existing models of indentation show that this procedure may underestimate the modulus by up to 30% (see Fig. 2 of Ref. [55]).

2) An equally challenging problem in testing thin films is properly accounting for the influence of a stiff substrate, which results in an overestimate of the modulus. For fully dense thin films the substrate effect is corrected using different models that account for the strain mismatch across the interface of the thin film and substrate [57, 59, 92]. However, the substrate effect in nanoporous films cannot yet be corrected using the above techniques since the modulus of NP foams is not constant with indentation depth. In order to make a qualitative assessment of the substrate effect, we employed the technique described in Refs. [57, 58] to analyze the NP Pt data by assuming that Poisson's ratio is zero and the modulus remains a constant throughout the indentation process. In this scenario we find that the substrate can cause the NP Pt modulus to be overestimated by up to 30%.

3) Residual stresses (compressive) can overestimate the modulus [63]. The amorphous alloy in our work is under compressive stress but after dealloying the residual compressive stress decreases significantly. For very small levels of residual stress, the modulus may change within a few percent. We therefore anticipate that residual stresses have a negligible influence on the modulus measurements of NP Pt foams.

3.3 ***Relative Density measurements***

The relative density of NP metal foams can be obtained using a variety of techniques suitable for materials with pores in the <100 nm range. Examples of techniques include: combining RBS spectra measurements for foams with known thickness [73], electron tomography of a representative volume of material [65, 93], imhibition methods and using 2D projections from micrographs to extract measurements of the porosity. The majority of the techniques require elaborate sample preparation and/or specialized equipment. Here we utilize electron micrographs to obtain the relative area of the different NP structures. As we discuss below, relative area is identical to relative density for "statistically" isotropic structures. We finally compare the relative density obtained from micrographs to the relative density derived from RBS spectra for a select number of samples.

3.3.1 SEM image processing

SEM micrographs are processed using Image J software package [94], to eliminate shadowing errors during acquisition prior to obtaining a measure of their relative density. Specifically, the images were processed with a bandpass filter that removes variation in brightness for length scales comparable to the image size and also smaller length scales (a few pixels). The average relative density is measured from the filtered images using the following expression:

$$\rho_M^* = 1 - \frac{\int \hat{I}(x,y)dxdy}{L_x L_y} \tag{3.2}$$

where ρ_M^* is the experimentally obtained relative density, $\hat{I}(x,y)$ is the thresholded image intensity, L_x and L_y are the width and height of the image. The thresholded intensity is defined as

$$\hat{I}(x,y) = \begin{cases} 0, & I \leq I_t \\ 1, & I > I_t \end{cases} \tag{3.3}$$

where I, the intensity of the grayscale micrograph image and I_t is a critical intensity value that segregates the image to features that correspond to a pore (assign a value of one) or a strut (assign a zero value).

An example of a processing sequence is shown in Fig. 3.2 for an SEM plan view micrograph of open cell NP Pt foam. Figure 3.2(b) shows the image processed with the bandpass filter. Figure 3.2(c) shows the image histogram that was used to set the critical intensity value, I_t, as the midpoint of the plateau region on the histogram. Figure 3.1(d) shows the binarized image with pores and struts clearly distinguished. Most images in our work exhibited similar histograms with the exception of Fig. 3.3(a) that exhibited three distinct slopes in its histogram. More sophisticated algorithms for edge detection may be necessary for images where the plateau in the histogram is absent. We estimated that the variation of relative density corresponding to choosing I_t between the two extrema of the plateau is within 4%. For Fig. 3.3(a) the density variation between two distinct slopes of its histogram is within 5%.

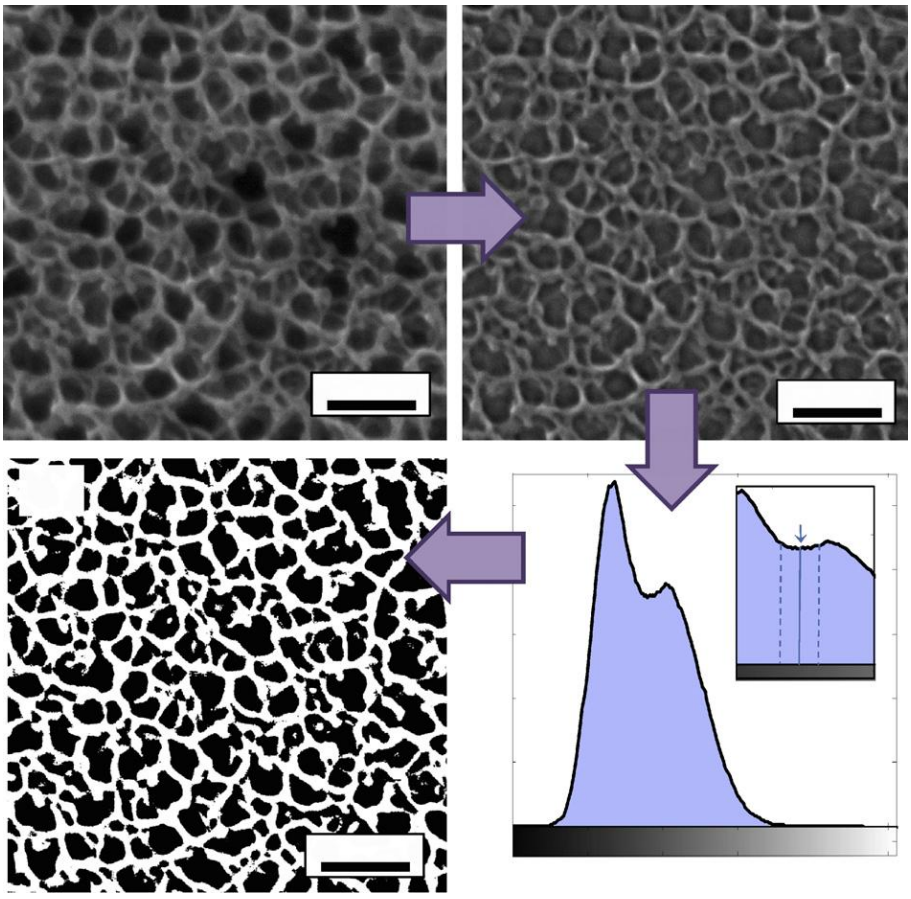

Figure 3.2 Image sequence showing how an SEM micrograph is converted to a binary image for relative density measurements: (a) plan view SEM micrograph of open cell NP Pt, (b) SEM image after bandpass filter and (c) the resulting histogram of the filtered SEM image. The insert shows an enlargement of the histogram plateau region. The midpoint of the plateau is set as the critical intensity value, It. (d) The critical intensity value is used as the criterion to convert filtered image to a binary image.

3. 2 Validity of the relative density measurements

In order to understand the conditions under which the relative density can be recovered from the two dimensional micrographs we assume that the foam is described by a microscopic density, *ρ(x,y,z)* i.e. the number of atoms in a microscopic volume element at coordinates x, y, z. Then we define the average relative density of the sample as $\rho^* = \frac{1}{V\rho_s}\iiint \rho(x,y,z)dxdydz$, where ρ_s is the density of the solid strut. Information

provided by the SEM micrographs using secondary electron (SE) contains mainly information about features near the free surface since signal detection probability exponentially decays when electrons travel in the out of plane direction. The thin layer near the surface is ~1nm for metals [95] and well within the diameter of a strut in NP metal foams. After processing sufficiently focused images, the relative density averaged over a narrow region close to the surface can be obtained. Specifically, the thresholded intensity of the image is $\hat{I}(x,y) \approx \overline{\rho(x,y,z)}/\rho_s$, where the overbar denotes average over a narrow surface layer. The quantity defined by Eq. (3.2) is an accurate representation of the average relative density when it is invariant in the out of plane direction, i.e. when $\iint \rho(x,y,z)dxdy$ is independent on z.

If a sufficiently large amount of struts and pores is captured in the micrograph view, then we can show that that the relative density from the micrograph is indeed independent in the out of view direction. In fact, for the images of NP metals that we have obtained, we can show that the average line density along any direction is independent of the other two dimensions. Figure 3.3(a) and (b) show plan view SEM and cross-section TEM images of open cell NP Pt foam. We identify the plan-view coordinates as x, y and the through thickness direction as z. Along each direction, the relative line density can be obtained from

$$\rho^*_{M_i} = 1 - \frac{\int \hat{I}(x_i)dx_i}{L_{x_i}} \tag{3.4}$$

where $\rho^*_{M_i}$is the relative line density, $\hat{I}(x_i)$ is the threshold intensity as defined in Eq. (3.3). Figure 3.3(c) shows a plot of the line density along three directions as a function of distance. The average line density along all directions is approximately the same: ~43±5%

for images with threshold at the midpoint of three distinct slopes of its histogram. The relative density for this sample was also obtained from RBS spectrum analysis using film thickness from TEM. The relative density using RBS was found to be ~46.6±2%.

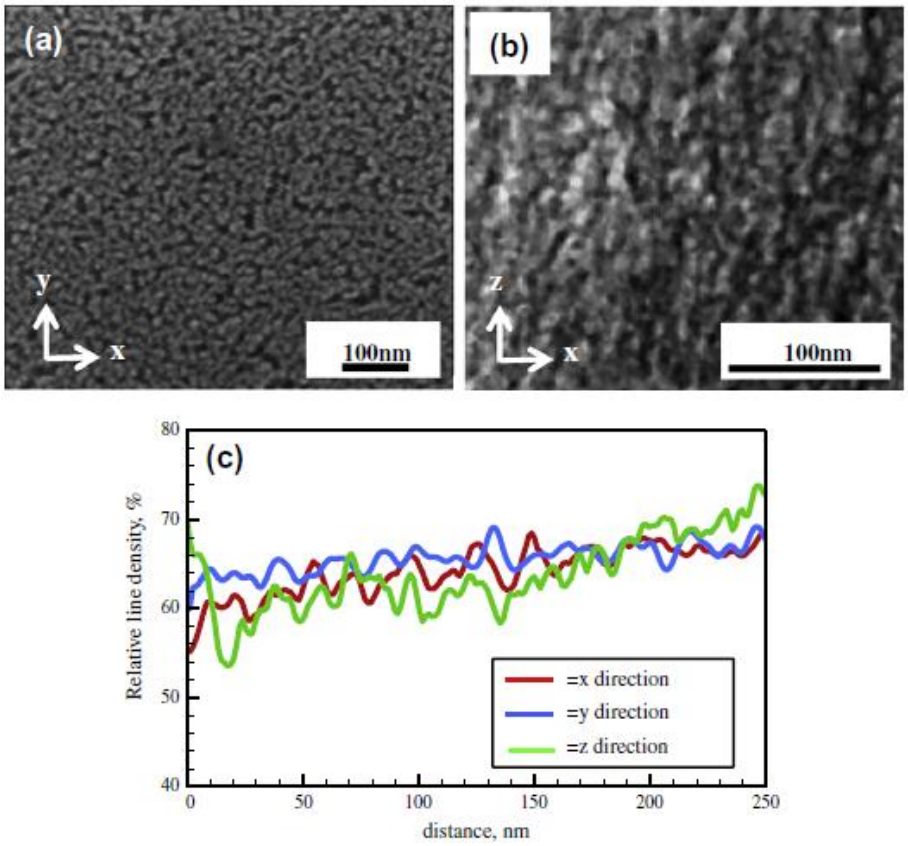

Figure 3.3 (a) Plan view SEM micrograph and (b) cross-section TEM micrograph of open cell NP Pt. (c) Line density plots with distance along the x, y and z directions. Axis directions are indicated in (a) and (b).

We note that similar analysis can be performed for transversely isotropic foams, e.g. columnar and voronoi type [10, 82]. Since the distribution of the columns and polyhedra is random then areal density is invariant in the out of plane direction when a large number of them are included in the relative area measurements.

Figure 3.4 shows a plot comparing relative density measured using micrographs and RBS. The error bars for the density obtained from SEM images are set by choosing I_t between the two extrema of the histogram plateau. We have included data from Ref. [73] in addition to our experimental data. For the SEM images of [73] there is greater variance (10%) in the plateau measurements since the micrographs we used were taken from the printed version of the publication and therefore are of relatively poor quality. We find that the relative density measured from stereographic projections and RBS are in good agreement as long as high quality SEM micrographs are used that capture a large enough number of struts and pores

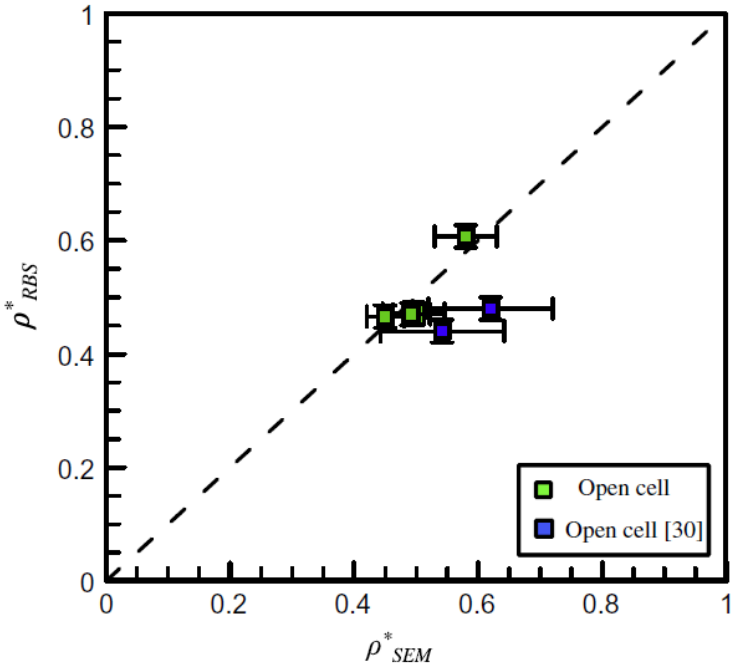

Figure 3.4 Comparison of relative density measurements using stereographic projections from SEM images and RBS measurements for known sample thickness. Data from Thorp [28] are included.

3.4 ***Scaling of relative density and strut dimensions***

3.4.1 Modified scaling relation of relative density with geometry

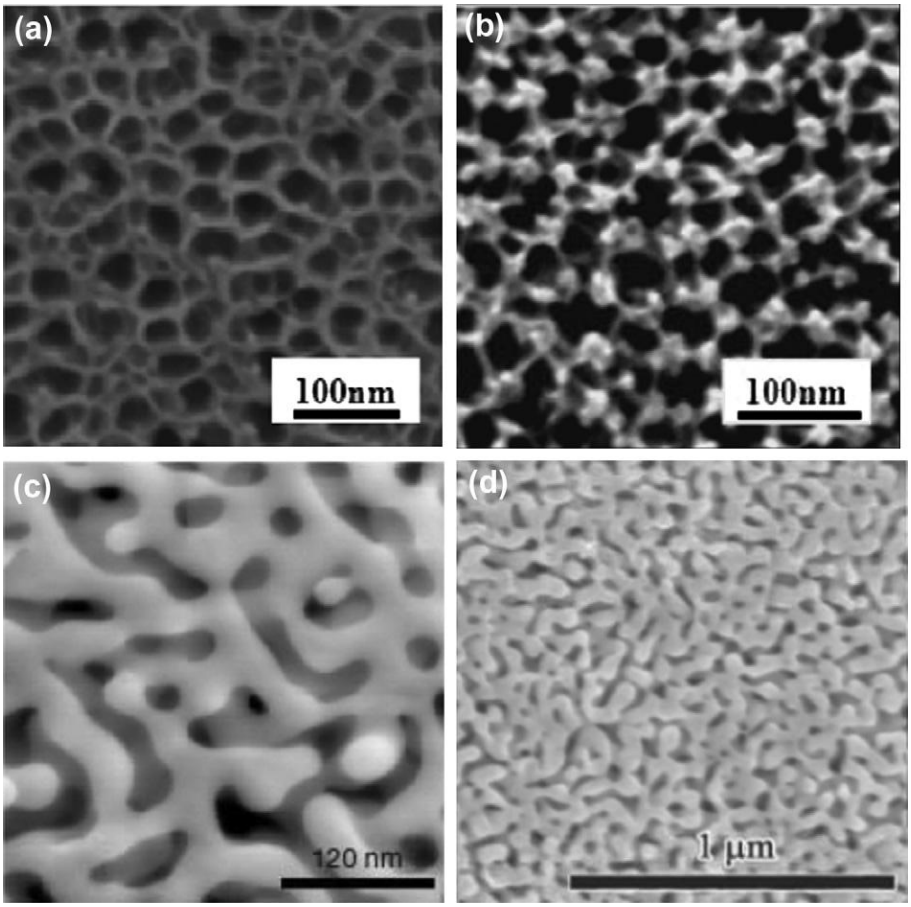

Figure 3.5 SEM micrographs of different open cell NP metal foams: (a) plan view SEM of NP Pt foam, (b) plan view SEM of NP Pt foam with greater joint sizes, (c) plan view of NP Au as reported by Erlebacher [9], (d) plan view of NP Cu as reported by Hayes [81].

Figure 3.5 shows a representative group of SEM plan view images of isotropic open cell NP metal foams of different materials. Two distinct strut morphologies of NP Pt assembled during dealloying of $Pt_{0.1}Si_{0.9}$ are shown: Fig 3.5(a) has longer strut lengths and 3.5(b) has larger joints. Figures 3.5(c) and (d) respectively show NP Au obtained by dealloying $Au_{0.26}Ag_{0.74}$ as described in the work of Erlebacher et al. [96] and NP Cu

obtained by dealloying $Cu_{0.3}Mn_{0.7}$ as described in the work of Hayes et al. [31]. By comparing the above SEM images we find that the strut thickness (t) and length (l) are the same order of magnitude (in the nm range). Similarly, the pore diameter (l_{pore}) is of the same order as the strut length, l, or in some cases is more elongated along a particular direction. The assembled struts and pores in open cell NP metal foams are different than those synthesized by other techniques such as sintering of metal powders and fibers, gas entrapment, direct foaming with gas, powder compact melting, casting methods, spray forming etc. [97].

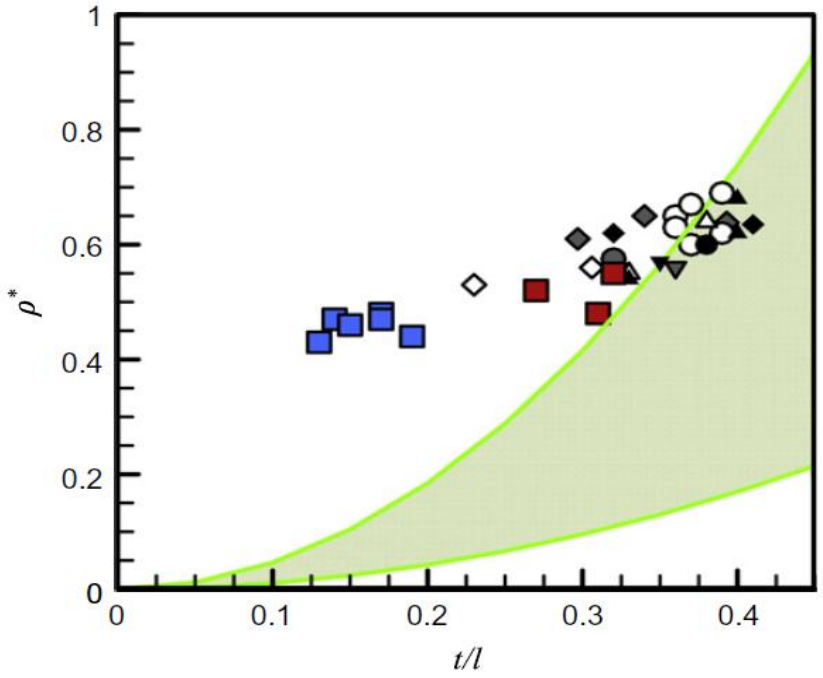

Figure 3.6 Relative density as a function of thickness to length ratio for isotropic open cell NP metal foams. The shaded region represents scaling predictions for density with $1 < C < 4.6$. Color data points are NP Pt. Data are in Table 3.1 (For interpretation of the references to color in this figure legend, the reader is referred to the web version of this article.)

Figure 3.6 shows a plot of relative density as a function of the strut-thickness-to-length ratio for NP metal foams with open cell morphology. Experimental results of NP

Pt are shown by color: red colored data are for samples conforming to large strut lengths similar to Fig. 3.5(a) and blue colored data are for samples with morphology similar to Fig. 3.4(b). Figure 3.6 also includes NP Au and NP Cu data using SEM images from the literature [11, 25, 29, 31, 35-37, 39, 41, 44, 71, 96, 98, 99]. The data are shown in Table 3.1. We emphasize that all the values of relative density used in this paper were obtained by us from SEM images through the procedure outlined in section 3.3. For the data points taken from the work of other researchers, we utilized SEM images from the respective publications. In many cases the resulting values of relative density disagree with the values reported by the authors. The reason for this discrepancy is that many researchers simply use the remnant atom fraction as the relative density. As we discussed in a recent publication [100], dealloying is associated with inevitable dimensional changes (with volumetric changes of up to 80%). Not properly accounting for these changes in the alloy volume can result in erroneous estimate of the relative density. As we have discussed in Section 3, measuring relative density from SEM images is a robust technique that has been verified by us and other researchers to yield values in excellent agreement with other well-established methods for direct measurements of relative density, such as RBS or electron tomography.

Table 3.1
Experimental measurements of geometric parameters (d/l, t/l) and the relative density for NP Au, NP Cu and our own NP Pt.

	Reference	*t/l*	*d/l*	P^*		Reference	*t/l*	*d/l*	P^*
◇	Volkert, 2006 [46]	0.31	0.06	0.56	▲	Thorp, 2006 [53]	0.4	0.1	0.47
	Biener, 2006 [45]	0.23	0.05	0.53			0.33	0.08	0.32
◆	Seker, 2007 [50]						0.4	0.08	0.46
		0.3	0.06	0.61	▼	Okman, 2011 [49]	0.35	0.08	0.57
	Seker, 2008 [51]	0.39	0.04	0.64	▽	Kucheyev, 2006 [48]	0.36	0.07	0.56
		0.34	0.11	0.65	●	Sun, 2008 [52]	0.32	0.06	0.58
♦	Erlebacher, 2001 [42]	0.41	0.06	0.64	■	NPPt	0.14	0.21	0.47
	Mathur, 2007 [13]	0.32	0.11	0.62			0.13	0.24	0.43
○	Hodge, 2009 [12]	0.36	0.11	0.63			0.15	0.27	0.46
		0.39	0.09	0.69			0.17	0.22	0.48
	Hodge, 2007 [47]	0.37	0.09	0.55			0.19	0.2	0.44
	Hayes, 2006 [43]	0.36	0.08	0.65			0.17	0.2	0.47
		0.39	0.08	0.62					
●	Liu, 2009 [54]	0.38	0.05	0.6	■	NPPt	0.32	0.09	0.55
△	Ding, 2004 [3]	0.33	0.09	0.6			0.31	0.08	0.48
		0.38	0.06	0.65			0.27	0.09	0.52

*Symbols correspond to those of Fig. 3.6. We note that the relative density for the literature data was obtained using SEM micrographs.

The solid lines on Fig. 3.6, represent simple scaling $\rho^* = C(t/l)^2$ for open cell foams that follows from dimensional considerations under assumptions of small thickness to length ratio, $t<<l$, and isotropic pores [40]. The regime of validity for the scaling relationship is for $t/l<0.1$ and is an upper bound for $t/l>0.1$ when several effects including double counting of corners in the unit cell become non-negligible [40]. The shaded region on Fig. 3.6 corresponds to $1 < C < 4.6$, the characteristic range of regular space-filling structures [40]. Remarkably, the experimentally measured relative densities of NP metal foams are significantly higher than the predictions based on scaling arguments. As can be seen in Fig. 3.6, ρ^* exhibits an almost linear rather than quadratic dependence on t/l across different open cell NP structures. The origin of the observed deviation of ρ^* from simple dimensional scaling likely lies in the morphology of the NP metal foams. For example, some of the NP foams have elongated pores, while others are characterized by high concentration of mass in the joints. The latter effect appears to have more pronounced influence on the deviation of NP metals from the relationship based on

scaling arguments. In the following section we extend the dimensional analysis arguments to investigate the effect of mass agglomeration using a regular rectangular unit cell.

3.4.2 Relative density of modified unit cell

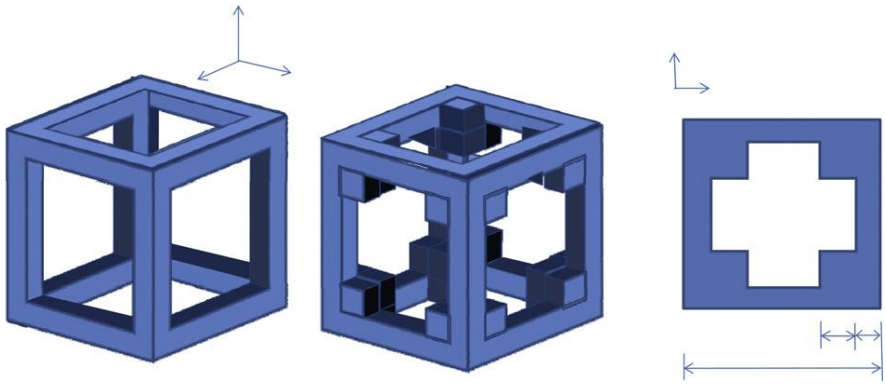

(a) (b) (c)

Figure 3.7 (a) A rectangular unit cell and (b) a modified unit cell with greater mass at corners. (c) Plan view of modified unit cell showing all relevant dimensions.

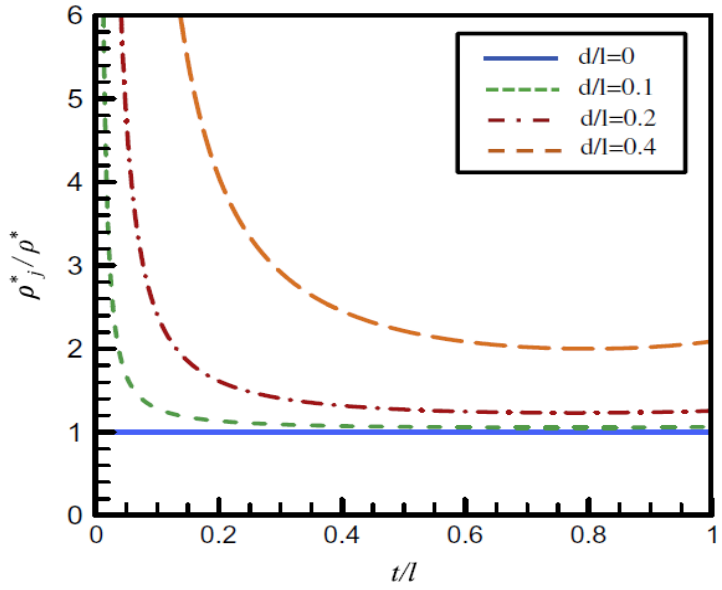

Figure 3.8 Relative density ratios of a rectangular unit cell with and without enlarged junctions as a function of strut-thickness-to-length ratios (t/l). The lines represent different joint-to-ligament-length ratios (d/l).

The effect of mass accumulation at the joints of a structure can be examined quantitatively in an ordered rectangular unit cell, shown on Fig. 3.7(a) with ligament length, *l* and thickness, *t*. Figures 3.7(b) and (c) show a modified unit cell with mass agglomerated at the joints, where *d* marks the increase in size of the joint. Simple dimensional consideration can give the ratio of the relative densities with and without junctions, as:

$$\frac{\rho^*_j}{\rho^*} = 1 + \frac{2(d/l)^2(t/l)+(2/3)(d/l)^3}{(t/l)^2-(2/3)(t/l)^3} \tag{3.5}$$

The effect for double counting of corners is accounted in the above ratio. Figure 3.8 shows a plot of the ratio of the relative densities with and without enlarged joints, ρ^*_j/ρ^*, as a function of the thickness to length ratio, *t/l*. The solid lines are predictions of Eq. (3.5) for different joint size to ligament length ratios, *d/l* =0, 0.1, 0.2 and 0.4. We observe that the effect of the added mass at corners becomes more pronounced for *d/l>0.1*. For example, when *d/l* = 0.2 and *t/l>0.2*, the relative density of a structure with large joints, shown on Fig. 7(b), is 20% greater than the relative density of a structure without enlarged junctions. The most dramatic change comes for structures where *t/l<d/l* that consist of thinner struts than joints. Then the increase in relative density for large joint structures grows exponentially with decreasing *t/l* ratio. Although NP metal structures have a random arrangement of struts in space, the unit cell equation (Eq. (3.5)) can be used to assess the effect of large joints on the relative density. For example, Eq. (3.5) indicates that a material with *t/l~0.15* and *d/l=0.2* will have ~1.9 times greater relative density than a structure with *t/l~0.15* and no added mass at joints. Indeed, NP Pt samples marked in blue in Fig. 6 have the greatest joint size (*d/l = 0.2*) and exhibit ~2

times higher relative density compared to the scaling law that does not account for mass agglomeration (solid lines in Fig. 3.6).

The likely reason for agglomeration of mass in the junctions is related to synthesis conditions during dealloying. The self-assembly is an agglomeration process and as such is controlled to a large degree by the mobility of atoms in the surface layer exposed to electrolyte [79]. In an instructive demonstration Li and Balk [101] showed that when the volume of the initial alloy is limited, the assembled structure will consist of a network of nanodots instead of an interconnected three dimensional (3-D) strut network. On the other hand, an interconnected strut network forms if sufficient mass exists. In this case, the struts can coarsen under exposure in the electrolyte [26, 37] or increased temperature [29, 35, 71, 98] at the cost of decreasing the overall dimensions of the sample [100]. The coarsening will result in NP metals with large t/l ratios. Based on our experimental observations we propose that in NP metal foams small t/l ratios are typically accompanied by an increase in joint size. Therefore, a correction similar to Eq. (3.5) should give a better measure of the relative density of NP metal foams with small t/l ratios. This is in contrast to bulk metal foams, which are synthesized by such techniques as gas injection in a melt.

Finally, we note that the relative density in Eq. (3.5) can be recast in the following convenient form:

$$\rho_j^* = \rho_f/\rho_s = C_1(t/l)^2 + C_2(t/l)^3 + C_3(d/l)^2(t/l) + C_4(d/l)^3 \qquad (3.6)$$

Where ($C_{1...}$ C_4) are proportionality constants. After a data fit with experimental data these constants are C = (10,13,19,20) for NP metal foams.

3.5 ***Effect on mechanical properties***

The unusual behavior of relative density as a function t/l has important implications on the mechanical properties of these structures. Indeed, for structures that obey scaling relations like $\rho^* \propto (t/l)^2$ the mechanical behavior can be expressed as a function of the relative density only [40]. In contrast, the mechanical behavior of NP metals is expected to depend more explicitly on the geometrical structure. In this section we describe how the Young's modulus can be affected by the presence of larger joints for decreasing *t/l* ratios. The comparison is made quantitatively for regular structures with unit cells shown on Fig. 3.7(a) and (b).

3.5.1 Influence of joint size on the Young's modulus

The stiffness of the overall porous structure is dependent on the manner with which individual struts deform. Typically, the dominant deformation mode is due to ligament bending especially as the *t/l* ratio decreases. The stiffness of a regular rectangular foam structure with unit cell shown on Fig. 7(a) can be obtained from the elastic deflection of a simply supported beam that is loaded at its midpoint [40]. In this modification, the dominant deformation mode is still due to strut bending. Then the stiffness of a rectangular unit cell with large joints can be easily obtained (Appendix A). The modified modulus scaling relationship is of the form

$$\mathrm{E}_{\mathrm{j}}^{*} = E_f/E_s = f(t/l, d/l) \tag{3.7}$$

where E_f is the stiffness of the NP metal with quantifiable joints, E_s is the stiffness of a solid strut and

$$f =$$

$$0.5\left[(t/l+d/l)^{-1}+1/8(t/l)^{-4}-[(t/l)^3+3(t/l)^2(d/l)+3(d/l)^2(t/l)+(d/l)^3](t/l)^{-4}\right]^{-1}$$

(3.8)

When *d/l=0*, Eq. (3.7) becomes the same as the Gibson-Ashby scaling relationship (e.g. E^*) with the correction for double corner counting [40]. The effect of enlarged joints is examined in Fig. 3.9, where E_j^*/E^*, the relative modulus ratio with and without enlarged joints, is shown as a function of the thickness-to-length ratio. The solid lines correspond to different joint-to-ligament-length ratios (*d/l* =0, 0.1, 0.2 and 0.4). In the regime where *t/l<0.1* there is minimal enhancement in stiffness for increasing *d/l* ratio as supported by FEM modeling of low density foams [83].

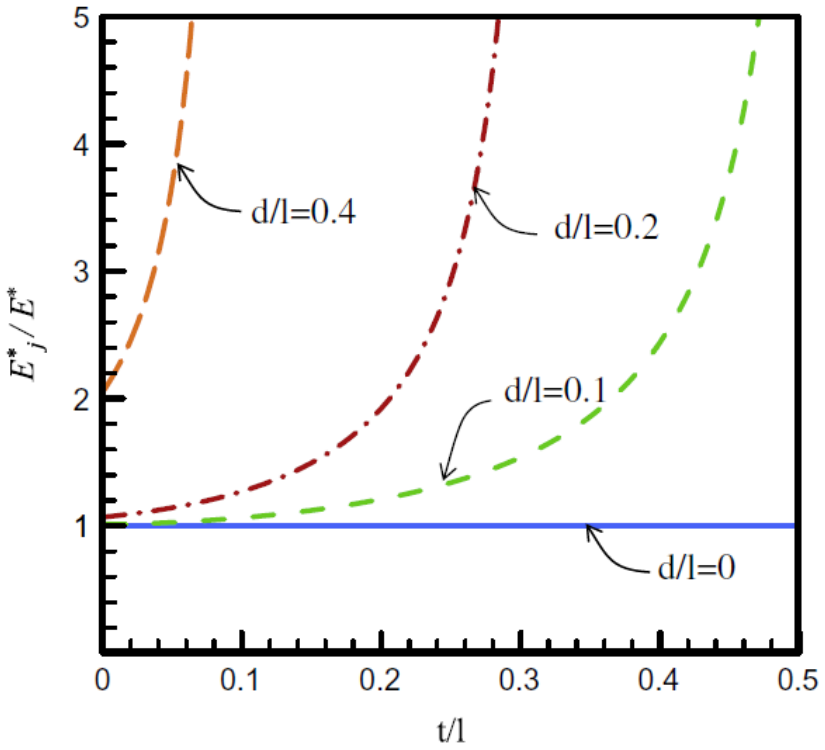

Figure 3.9 Ratio of relative Young's modulus for a rectangular unit cell with enlarged junctions as compared to a rectangular unit cell with regular size junctions. The ratio of relative moduli is plotted as a function of the thickness-to-strut ratio.

In order to test the predictions of the modified scaling relationship we have compiled a database of the values of E_f for a variety of NP metal foams. This includes our own measurements of polycrystalline NP Pt (grain size 5 nm) [82] as well as NP Au results published in the literature. For NP Au the polycrystalline structure of the initial alloy is preserved during dealloying with typical grain sizes larger than 10 μm [38]. Small-scale tests such as nanoindentation are typically conducted within a single grain, so that the data more closely correspond to single crystal NP Au behavior. All of the data are obtained using nanoindentation where the reduced modulus was directly measured. E_f is obtained from the reduced modulus by correcting for indenter compliance and accounting for the poisson's ratio of NP metal. While the poisson's ratio for NP metals has not been precisely determined, it can be expected to be within $(0 < \nu^P < 0.5)$ the bounds for low density foams and incompressible solids respectively.

Table 3. 2
Experimental measurements of geometric parameters (d/l, t/l) and the relative modulus for NP Au from the literature and our own NP Pt (these values are plotted in Fig. 3.10).

	d/l	t/l	E_f	E/E_s
Seker, 2007 [50]	0.04	0.39	16	0.20
Volkert, 2006 [46]	0.05	0.36	7	0.09
Biener, 2006 [45]	0.05	0.23	3.6	0.06
Hodge, 2009 [12]	0.05	0.45	24	0.40
Lee, 2007 [59]	0.08	0.39	8.8	0.11
Lee, 2007 [59]	0.08	0.39	13.2	0.17
NP-Pt foam	0.09	0.27	62	0.37
NP-Pt foam	0.11	0.32	55	0.33
Hodge, 2009 [12]	0.11	0.36	8	0.10
Seker, 2007 [50]	0.11	0.37	15	0.19
Mathur, 2007 [13]	0.11	0.35	9	0.11
Seker, 2007 [50]	0.12	0.38	13	0.16
Seker, 2008 [51]	0.12	0.37	21	0.27
Hodge, 2009 [12]	0.13	0.38	12.5	0.16
Biener, 2005 [58]	0.13	0.29	11.1	0.14
NP Pt-foam	0.13	0.21	48	0.28
NP Pt-foam	0.17	0.22	76	0.45
NP Pt-foam	0.2	0.19	50	0.30
NP Pt-foam	0.2	0.17	73	0.44

Figure 3.10 summarizes the experimental measurements of the relative modulus, E_f/E_s for NP metal foams of various geometries and compares them against the prediction of Eqs. (5-6). In the absence of reliable information on the value of solid strut modulus E_s we choose it to be the value of bulk modulus: 79 GPa for single crystal gold and 168 GPa for bulk polycrystalline platinum [102]. The error bars on the experimental data of Fig. 3.10 reflect the extrema of the plastic Poisson ratio. The error bars do not include possible systematic errors associated with nanoindentation (as discussed in Section 3.2.3) since the experimental conditions are not always documented by various authors. For our measurements of NP Pt, the maximum estimate of these errors is up to 30%. As we will discuss shortly, the conclusions of this work regarding Pt are robust against even the maximum possible errors. It is also important to emphasize that effects

associated with the influence of substrate and of the indented volume are systematic and do not affect relative magnitude of modulus in foams with different morphology, provided that the experimental conditions are the same.

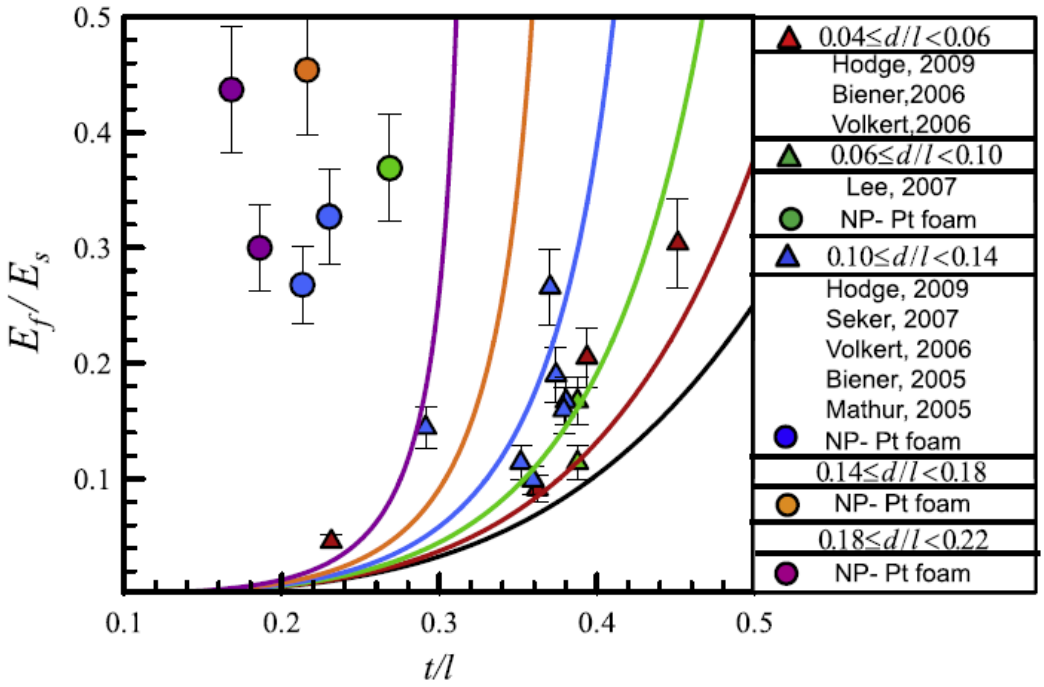

Figure 3.10 Relative modulus for NP metal foams as a function of strut thickness to length. Solid lines represent predictions based on Eqs. (3.7) and (3.8). Different colors represent different d/l ratios. The circles are NP Pt data.

Samples with the lowest *t/l* values correspond to NP Pt and samples with the highest *t/l* values correspond to NP Au. Under the employed assumption that the modulus of the strut is equivalent to bulk modulus values, all the experimental data show that the modulus of NP metal foams is greater than the simple scaling prediction (black line) that corresponds to *d/l=0* and corrects for double counting of corners. Overall, the stiffness response of NP Au data is well captured by the modified scaling predictions that account for the effect of large joints. We emphasize that these predictions have no free parameters. The agreement is better for data corresponding to foams with large joints (*d/l>0.1*). This

might be expected, since the predicted dependence of stiffness on *d/l* is quite steep and it is difficult to reliably measure the dimensions of joints with very small *d/l*.

1) The agreement with experimental observations validate the modified scaling law which predicts that large joints can cause up to 100% increase in the modulus when compared to the geometry with no joints for the same *t/l*.

2) This agreement gives clear evidence that the enhancement in stiffness seen in single crystal NP Au and NP Cu is more likely explained by the effect of geometry rather than the onset of effects at the nanoscale.

Remarkably, the scaling relationship cannot account for the high modulus of nanocrystalline NP Pt. The likely source of this discrepancy lies in the enhancement of modulus of struts compared to the assumed properties of bulk Pt. Indeed, apart from small *t/l* the overall geometry of the NP Pt does not exhibit any special features that would distinguish it from the other considered systems. For small *t/l* ratios struts deform in bending and other modes such as elastic buckling are very unlikely to occur in metal foams [45] and are even less likely in the presence of large junctions. On the other hand, simulations of such nanostructured metal systems as nanocrystaline solids and nanowires have shown that the modulus deviates from the bulk when the size of either the internal characteristic scale (e.g. grain size) or the size of the geometric features (e.g. nanowire diameter) is smaller than 10 nm [54, 103-105]. For NP Pt, both the internal characteristic scale and the geometric features are $\sim$ 5 nm so both effects are expected to influence the modulus. It is therefore natural to assume that the observed enhancement in the value of the relative modulus for Pt is not a geometric effect, but rather is explained by the

enhancement of the properties of individual struts compared to the assumed values of bulk Pt. Under this assumption, our data indicates *more than one order of magnitude* enhancement of the strut modulus compared to bulk Pt.

Since the existing data on NP Au does not deviate from the scaling predictions, it is instructive to compare and contrast NP Au with NP Pt. The struts and junctions of the NP Au analyzed by us are almost exclusively single-crystal with a typical size in the range 20-70nm. In contrast, our NP Pt has nano-crystaline struts and junctions with typical sizes smaller than 10nm. Thus our data appears to be consistent with the notion that the modulus of struts deviates from the bulk value when either the size of an internal scale (e.g. grains) or the size of the strut itself becomes less than 10 nm. We note that Mathur and Erlebacher experimentally observed a significant enhancement in the value of relative modulus of NP Au when the characteristic size of the struts was below 10nm [106].

3.6 ***Conclusions***

1) In porous media, the relative density is an important parameter that influences the relationship between geometry and material properties. For example, in low density foams ($\rho^* < 0.1$) the macroscopic material properties depend on the foam geometry *only* through the relative density. In contrast to low density foams, the modulus of NP metal foams does not exhibit a clear correlation with the relative density. We set out to understand whether the deviation is due to the onset of effects specific to nanostructured materials or can be explained by a new scaling relationship appropriate to NP metal foams.

2) We measure the relative density experimentally using carefully focused micrographs from SEM and validate these measurements using RBS. We find that the density of NP metals is much higher ($\rho^* \geq 0.4$) that has been assumed. Thus, it lies outside the regime of validity of the commonly used scaling laws. We then re-examine the scaling relationships for NP metals by looking at the relationship between relative density, strut geometry and modulus.

3) We find that the relative density exhibits an almost linear dependence with strut geometry and deviates from dimensional analysis arguments for low ratios of *t/l*. Close inspection of the morphology from SEM micrographs reveals that there is agglomeration of mass at junctions. We modify the scaling relationship for relative density to account for mass agglomeration and find good agreement with experimental observations.

4) We examine how mass agglomeration can influence the modulus of a porous medium. We formulate a modified scaling relationship between geometric parameters (*t/l* and *d/l*) that account for strut and junction effects respectively. The relationship shows that as junction size increases so does the modulus of the porous medium.

5) This modified scaling relationship for modulus is compared against experimental measurements of NP metal modulus obtained using nanoindentation. In order to make the comparison, we assume that the strut modulus for NP metals is the same as the modulus of bulk dense solid. We find that the model prediction agrees with single crystal NP Au data from the literature for large junction sizes (*d/l>0.1*). This

validates the modified scaling relationship and shows that enhancements in NP Au data are mainly due to geometric effects.

6) On the other hand, NP Pt exhibits more than an order of magnitude higher relative modulus than the modified prediction. We argue that the origin of this enhancement lies in the normalization of the experimental data with the modulus of bulk solid. Indeed, NP Pt has nanosized grains (~5 nm) within struts of comparable thickness. We note that simulations of other nanostructured materials, such as nanograined solids and nanowires, show deviation of elastic modulus from the bulk once the grain or wire diameter is below 10 nm.

7) We hypothesize that NP metal modulus is influenced by material effects once the strut diameter is less than 10 nm. If the modulus enhancement is mainly due to a change in strut properties, then NP Pt struts exhibit more than an order of magnitude higher modulus than bulk Pt. For struts higher than 10 nm enhancements in the modulus are mainly due to geometric effects. In contrast to NP Pt, the data we analyzed for NP Au have strut thicknesses in the range of 20-70 nm. Therefore, the fact that the inferred strut modulus for NP Au is the same as bulk modulus is consistent with this hypothesis. We anticipate that other NP metal foam properties such as strength and conductivity will be affected by the agglomeration of mass that affects the scaling between relative density and strut geometric parameters.

CHAPTER 4

MECHANICAL PROPERTIES OF NANOCRYSTALLINE NANOPOROUS PLATINUM

4.1 ***Introduction***

Nanoporous (NP) metals often exhibit highly unusual mechanical, thermal, and electronic properties that are thought to originate from the abundance of nanoscale structure with typical internal scales in the range 2-100 nm[9, 107-109]. Structurally, NP metals are open cell foams, i.e. they can be thought of as interconnected three-dimensional (3D) network of nm-sized struts and joints. These materials combine a high surface-to-volume ratio with desirable properties of metals (e.g. high electrical conductivity and strength), which makes them highly attractive in many applications. Indeed, NP metals have demonstrated great potential as electrodes in electrochemical energy storage devices [2, 4, 77], sensors [9, 110, 111], and nanoactuators [9, 81]. At the same time, a thorough understanding of the origin of the observed physical properties of NP metals is still lacking, especially for structures with complicated hierarchical internal structure, such as NP metals with nanocrystalline and/or nanotwinned joints and struts [10, 82, 112]. Here, we present a combined experimental and simulation study of the mechanical properties of one such system, nanocrystalline NP Pt.

It is well appreciated that mechanical properties of metals crucially depend on the processes of creation, interaction, and annihilation of defects, which in turn are greatly affected by presence of free surfaces and planar defects. Viewed in this context,

nanocrystalline NP metals are a distinct and fascinating class of metals, where *both* planar defects and free surfaces are volumetrically abundant. Moreover, the geometrical structure of the strut and joint network also plays a role in determining the macroscopic response of the system, as is well-known from the studies of bulk metals foams with much larger characteristic length scales [113, 114]. The influence of the free surfaces has been extensively investigated in the context of the size scaling for NP metals with grains in the micron and above range, where individual struts are effectively single-crystal [115, 116]. Such investigations typically find an increase in the inferred strength of individual struts with decreasing size, an effect that has been attributed to the increasing role of surfaces in inhibiting formation and/or promoting annihilation of certain types of defects (e.g. dislocations). While no systematic investigation into properties of nanocrystalline NP metals has been undertaken before, some pertinent information is available from the studies of nanowires and nanopillars. Indeed, nanocrystalline NP Pt has grains of comparable size to the strut diameter. In this regime, grain boundary sliding may become the dominant mode and significant *weakening* of the strut properties may be expected when tested in compression [117]. However, there is little experimental information on the effect of decreasing diameter on the properties of nanowires for the case when strut size is comparable to grain size. Moreover, it has been shown that in a configuration where grains have a preferential orientation with respect to the free surface, grain boundary sliding may be suppressed [118].

In this paper we report nanoindentation measurements of the strength of nanocrystalline NP Pt samples with strut dimensions in the 4-10 nm range. Transmission Electron Microscopy (TEM) and analysis of selected samples revealed the average strut

thickness to grain diameter ratio to be t/D~1. Since the surface-to-volume ratio scales inversely with the characteristic size of the struts, nanocrystalline NP Pt with characteristic strut thickness in the range below 10 nm is of great interest in many applications. Since the grain size may become comparable to the strut thickness, in principle one might expect that the mechanical properties of such NP metals are significantly degraded. Through a combination of scaling analysis, experimental observations, and atomistic simulations, we show that the individual struts do become somewhat weaker as their size decreases. However, the decrease in the properties of the overall network with decreasing t is rather gradual, so that NP Pt with the smallest struts t ~ 3 nm synthesized in this work is still characterized by hardness of H_f ~ 0.2 GPa. We argue that the geometrical structure of NP metals plays a more prominent role in controlling its properties than previously appreciated. Furthermore, the simulations reveal a significant tensile/compressive asymmetry in the properties of individual struts, which can influence the dominant deformation mode for struts with sizes of less than 10 nm. In this regime, the material and geometrical properties of NP metals thus profoundly interact with each other.

This paper is organized as follows: Section 2 is a description of the experimental and numerical protocol for the synthesis, mechanical testing of NP Pt as well as molecular dynamics simulations of struts. Section 3 presents the results on the morphology and hardness of hierarchical NP Pt and an estimate of the strut strength. Sections 4 and 5 present the discussion and conclusions respectively.

4.2 ***Experimental and Numerical Methodology***

4.2.1 Sample synthesis

NP Platinum was synthesized as follows: first, an amorphous platinum silicide alloy (Pt_xSi_{1-x}, x=0.1-0.35) was deposited on a silicon substrate (100) using sputtering or vapor deposition. The resulting amorphous alloy was electrochemically dealloyed in dilute hydrofluoric acid (3% in deionized water) under an externally applied potential in the range (0.3 - 0.9)V [82]. During the dealloying process, silicon was completely dissolved in the electrolyte while the platinum self assembled into a three dimensional network of struts [119]. The sputtering parameters were tuned so as to produce amorphous thin films with varying levels of residual compressive stress. The stress enables crack-free assembly of NP metal during dealloying [100] and, together with dealloying parameters, serves to control geometrical structure of NP metal [10, 82]. Vapor deposited amorphous samples were always under residual tensile stress, so that varying dealloying parameters controlled both NP Pt geometrical structure and enabled crack-free assembly.

4.2.2 Characterization

In this work we examine mostly isotropic NP Pt with varying strut thickness, length and junction size. Each NP Pt sample was examined with a Scanning Electron Microscope (SEM) under plan and tilt views. Statistical information on the strut length, strut thickness and junction size were obtained by analyzing SEM images [94]. For each sample, approximately 30 measurements of these parameters were made and the average values were used in the subsequent analysis. The distributions of the measurements

within each sample are relatively narrow, with typical standard deviation approximately (10-20) % from the average value. The relative density for each sample was obtained from SEM stereographic projections using a procedure outlined elsewhere [69]. Here we define the relative density $\rho*$ as the ratio between the volume occupied by solid to the total volume of the structure. A select number of samples were examined using Transmission Electron Microscopy (TEM). NP metal samples were encased in epoxy, cross-sectioned using a sandwich method, and thinned to electron transparency using a combination of mechanical polishing and ion milling techniques (Gatan PIPS™). The cross-section TEM samples were imaged using bright field, dark field and high resolution imaging using a Jeol 3000™ and Tecnai TF30™ TEM. TEM cross-section views of the initial platinum silicide alloy confirmed that it was amorphous [82].

4.2.3 Nanoindentation

The mechanical response of NP Pt samples was obtained from nanoindentation using a Hysitron Triboindenter equipped with a Berkovich tip with radius of 150 nm. Arrays of 25 indents were performed on each sample and the hardness was obtained from the unloading slope of each indent using the procedure outlined by Oliver and Pharr [91, 120]. The reported NP Pt hardness is obtained from unloading curves by averaging the values measured at indent depths within 30% of the foam thickness over a range of depths corresponding to two to five pore sizes. In that range of indentation depths both the effect of the substrate [121] and size effects due to limited contact with cell walls at shallow depths are minimized.

4.2.4 Molecular Dynamics (MD) simulations

The mechanical strength of individual single-crystalline and nanocrystalline struts with similar geometrical size as seen experimentally was assessed using MD simulations. The Large-scale Atomic/Molecular Massively Parallel Simulator (LAMMPS) [122] with a Pt embedded atom method (EAM) interatomic potential [123] was used to uniaxially deform 2-25 nm diameter struts. Single-crystalline struts, with diameters of 2, 5, 15 and 25 nm, aligned along the high-symmetry [100] and [111] directions were generated using LAMMPS. To create the nanocrystalline struts, bulk nanocrystalline structures were generated with grain size of 2.5, 5, 10, 15, and 22 nm using a modified Voronoi tessellation method that preserved the grain morphology/orientations and relative positions for all sizes. Five different cylindrical struts were then extracted from each bulk nanocrystalline structure with a diameter equal to the grain size – resulting in a total of 25 different struts (5 for each grain size). The resulting stress-strain behaviors shown below are averaged from the 5 different nanocrystalline struts of each grain size. We used multiple struts of each grain size to get more statistically relevant results of the mechanical behavior, as different grain morphologies/orientations have a more significant effect on the strength as D/t~1. Each strut was generated with an initial aspect ratio of 3:1. Periodic boundary conditions were employed in the axial direction with free surfaces in the transverse directions. Prior to the imposed uniaxial straining, the energy of each strut was minimized by a conjugate gradient scheme and then equilibrated to 300K under isothermal conditions to achieve zero axial stress and surface relaxation. For the nanocrystalline samples, a 100 ps equilibration was used to allow the grain boundary structures and surface facets to relax into lower energy states. Each strut was deformed at

a constant strain rate of 10^9 s^{-1} along the strut axis under both tension and compression at 300K. During straining simulations, atomic stress tensor calculations were performed and averaged over the entire structure to obtain a global stress-strain behavior. The crystallographic structure of each atom, based on its nearest neighborhood, was followed to distinguish lattice and interface atoms.

To analyze the deformation behavior within the struts, we leverage post-processing algorithms to compute non-local estimates of the strain field around each atom [124-126]. The initial atomic neighborhood of each atom is quantitatively tracked during deformation and an atomic formulation of various kinematic metrics and their application to nanoscale systems from continuum mechanics theory is obtained, as outlined by Tucker et al. [124-126]. In particular, the atomic strain tensor (**E**) is obtained from the deformation gradient tensor (**F**), as $\mathbf{E} = 1/2\,[\mathbf{F}^T\mathbf{F} - \mathbf{I}]$, where **I** is the identity tensor. Once the atomic strain tensor (**E**) is calculated for every atom with respect to the undeformed configuration and each atom's calculated nearest neighbors, the atomic deviatoric strain tensor (**E***) is calculated as $E^*_{ij} = E_{ij} - (E_{kk}/3)\delta_{ij}$, from the atomic strain tensor **E**. The second invariant of the deviatoric strain tensor (e*) is calculated from

$$e^* = (1/2)E^*_{ij}E^*_{ij} \tag{4.1}$$

providing an estimate of the effective shear strain in the neighborhood of each atom.

4.3 ***Results***

4.3.1 Hierarchical Structure of the nanoporous platinum

Figure 4.1(a)-(c) shows SEM plan views of open cell NP Pt morphologies with similar relative density (within 2%). Samples shown in Fig. 4.1(a)-(b) were synthesized from co-sputtered $Pt_{0.1}Si_{0.9}$ (atom percent) by electrochemical dealloying under an externally applied voltage of 0.6 V and 0.7 V respectively. The sample synthesized by dealloying vapor deposited $Pt_{0.2}Si_{0.8}$ at V = 0.7 V is shown in Fig. 4.1(c) plan view SEM. It is apparent that the geometrical structure of NP Pt can be manipulated by changing synthesis conditions. For example, the junction size increases as the externally applied voltage was increased from 0.6 to 0.7 for samples that were co-sputtered under identical conditions.

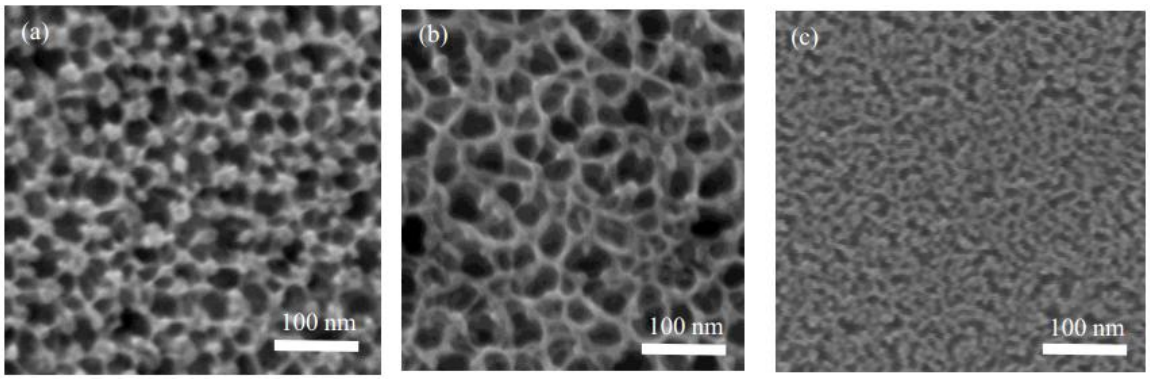

Figure 4.1 Plan SEM view of the various NP Pt morphologies synthesized from: co-sputtered amorphous Pt0.1Si0.9 films at (a) 0.6 V and (b) 0.7 V and NP Pt from co-evaporated amorphous Pt0.2Si0.8 at (c) 0.7 V.

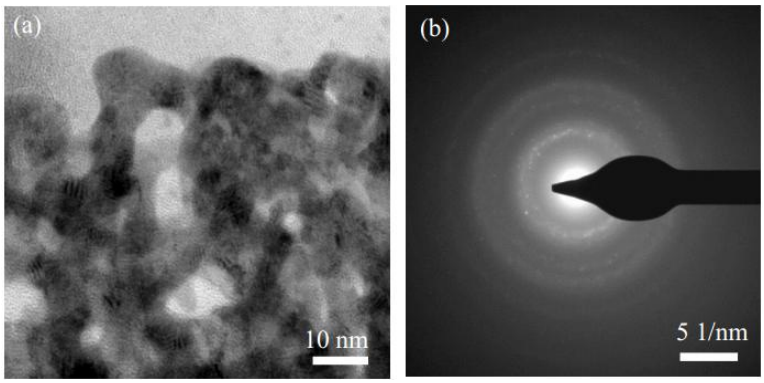

Figure 4.2(a) Bright field TEM cross-section view of multiple struts of co-evaporated NP Pt. (b) Selected area diffraction pattern of a region 470 nm^2 in size showing multiple nanocrystalline grains.

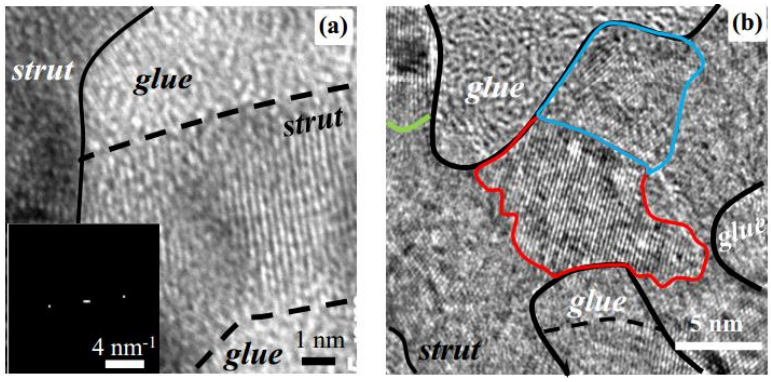

Figure 4.3 (a) HRTEM of a strut with diameter of 5 nm and length of 10 nm surrounded by glue. The insert shows the power spectrum of the strut with average interatomic spacing of 0.24 nm. (b) HRTEM image of a multi-grain strut. The strut outlines are marked in black and approximate grain boundaries are shown by the red, blue and green outlines. To enhance contrast, images have been processed with a band-pass filter.

The grain structure of the sample shown in Fig. 4.1(c) is illustrated in Figs. 4.2 and 4.3. Figure 4.2(a) shows a bright field TEM image of a cross section of the sample. The selected area diffraction pattern of an area of size 470 nm^2 from the same image is shown in panel (b). We conclude that the analyzed region consists of a large number of randomly oriented grains. Figure 4.3(a) shows a 30x30 nm High Resolution TEM (HRTEM) image with two struts each containing multiple grains, with their

corresponding power spectrum found in the inset. Figure 4.3(b) shows the HRTEM image of multiple struts surrounded by epoxy (glue). The lattice planes of three grains are clearly visible (0.23 nm spacing) and their approximate boundaries are marked by the red, blue and green lines, respectively. Since the average grain size is of the same order as the strut diameter for several samples that were analyzed, we deduce that along the strut diameter there is only one grain, i.e. the ratio of strut thickness to grain size $t/D \sim 1$. This was also confirmed from the dark-field TEM views of several samples analyzed in this work. Both of these images show that there may be multiple grains along the strut. From the TEM analysis of multiple struts in the foam, it is observed that the ends of a strut (i.e. the joints) are mostly marked by grain junctions where different struts with different orientations encounter each other. The Fast Fourier Transform (FFT) of Fig. 4.2(b) shows a relatively continuous ring of /111/ spots. This implies that there is no preferential orientation, since this is a random cross-section. The /111/ planes may appear more easily in the high resolution images because of the large distance between them, which makes them easier to image even at tilts away from the exact zone axis orientation, and also because of the high structure factor and relatively high multiplicity factor (amongst the low index planes). Indeed, an X-Ray Diffraction (XRD) scan of the NP Pt shows near-random-orientation intensities of the different planes. Furthermore, XRD scans of NP Pt from co-sputtered initial alloys also show that the strut thickness to grain size $t/D \sim 1$.

It is well known that many properties of porous media, e.g. stiffness, strength, conductivity, exhibit universal scalings with the relative density. For example, the strength of bulk low-density open cell foams is typically found to scale as $\sigma_f = C\sigma_s \rho *^{3/2}$,

where C is a constant and σ_s is the yield strength of individual struts[40]. Fundamentally, such relations arise because the relative density provides a convenient measure of the typical strut geometry, which is the parameter that ultimately determines the mechanical response of the individual struts. In the example of the low density open cell foam, $\rho * \sim (t/l)^2$. As we have examined previously [69], NP metals are often characterized by agglomeration of mass at the junctions, a geometrical feature that breaks the traditional relation between relative density and average strut geometry. This is illustrated in Fig. 4.4, which shows the relative density of NP Pt analyzed here as a function of (t/l). Since the latter is a ratio of two quantities characterized by significant variations across sample, the compound quantity has a rather large standard deviation as indicated by the corresponding error bars. Nevertheless, it is clear that the relative density of NP Pt cannot be described by the traditional scaling. This has important consequences for understanding the properties of the NP Pt, as described below.

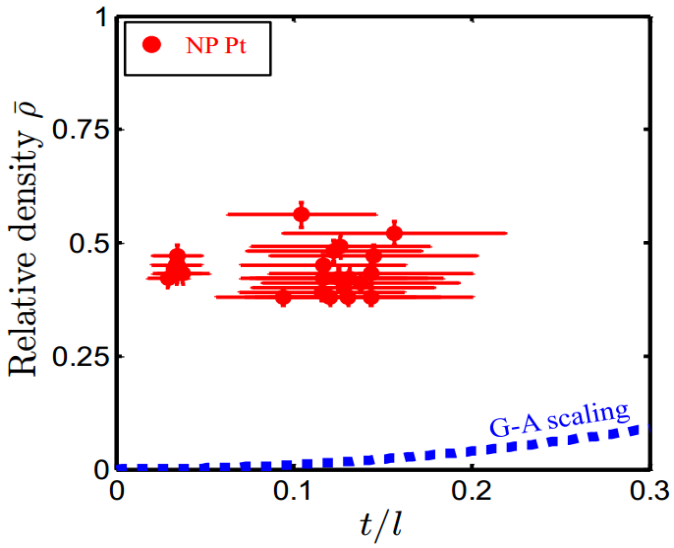

Figure 4.4 Relative density of NP Pt as a function of t/l ratio. Gibson and Ashby scaling relation ρ = (t/l) 2 is also shown. Due to accumulation of mass in junctions, the NP metal relative density deviates from this scaling by as much as two orders of magnitude. The error bars in t/l

correspond to a 40% deviation from the average, which is a typical standard deviation of the measured distributions. Similarly, the error bars in relative density are 5% of the average.

4.3.2 Hardness of the nanoporous platinum

The foam hardness is found to be in the range of 0.2 to 1.3 GPa for all NP Pt samples examined in this work. The corresponding strut thickness is in the 3-10 nm range, while the relative density is within 38-55%. In comparison, the hardness of nanocrystalline dense platinum with grain size 12 nm was found to be ~3 GPa [117], while a typical value of hardness for bulk fully dense platinum is ~0.7 GPa [102]. The measurements of the hardness are summarized in Fig. 4.5, which shows the measured hardness as a function of both the relative density and the average strut thickness *t*. It is clear that hardness does not exhibit a simple correlation with relative density. The NP Pt with very thin struts $t < 4$ nm is characterized by lower hardness compared to the samples with thicker struts, but overall the correlation between hardness and strut thickness is also rather poor.

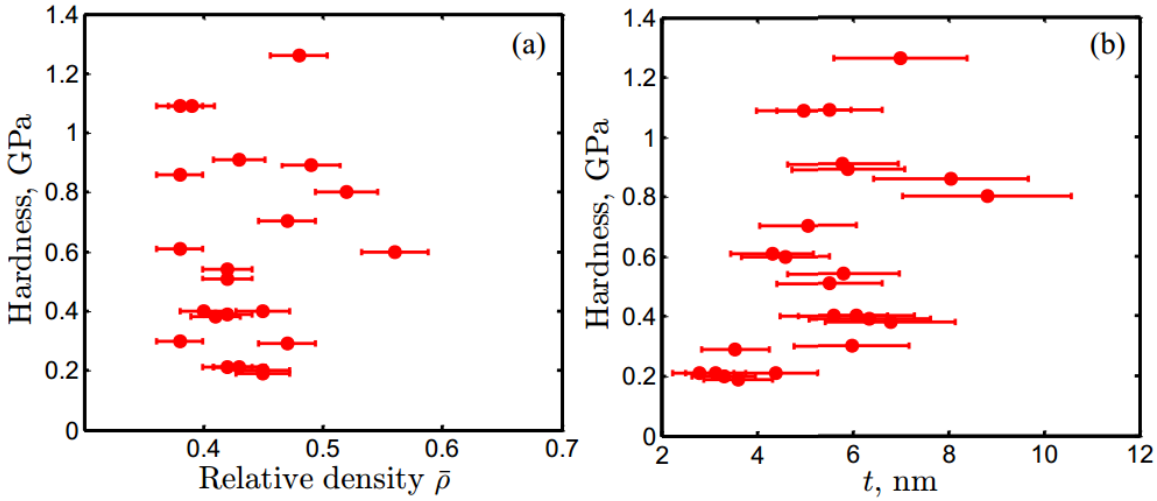

Figure 4.5 NP Pt foam hardness as a function of (a) relative density and (b) strut thickness, t. The , the error bars in relative density are 5% of the average whereas the error bars in t correspond to a 20% deviation from the average.

4.3.3 Molecular Dynamics Simulation of individual Struts

Figure 4.6 shows the deformed state of nanocrystalline struts tested in tension using MD simulations. In panels a) and c) atoms are colored according to their computed potential energy from the interatomic potential, while in panels b) and d) the color corresponds to calculated effective shear strain e^* defined in Eq. (4.1). The deformed struts in Fig 4.6(a)-(b) have $t = 5\ nm$ and struts in Fig. 4.6(c)-(d) have t = 15 nm. For all struts, there is approximately 1 grain across the strut thickness ($t/D \sim 1$) and $t/l = 1/3$. The effective shear strain e^* shown in Fig 4.6(b), (d) highlights the regions where the greatest shear (relative to the undeformed strut) has occurred due to the imposed tensile straining. Each strut was uniaxially strained beyond its elastic limit until extensive inelastic deformation had occurred. Clearly, the majority of strain accommodation has occurred within the necked region and along grain boundaries within the strut, as highlighted by the greatest atomic shear strain. The observed high strain regions correspond to deformation mechanisms of grain boundary sliding and local dislocation slip along the interface planes to accommodate the macroscopic imposed strain from the simulation conditions. It is interesting to note that negligible strain accommodation has occurred outside the necked region, especially within grain boundaries aligned vertically (parallel to strut axis). This is true for both the t = 5 nm and t = 15 nm struts. In the t=15nm strut, there is also evidence of local dislocation plasticity within the necked region and next to the highly strained grain boundaries (light blue/green atomic planes). The same nanocrystalline struts tested under compression are shown in Fig. 4.7 As compared to the resulting deformed nanocrystalline struts under tension, the struts under compression do

not display the same localized strain regions. Under compression, the shear strain appears to be accommodated along numerous grain boundaries throughout the sample. In addition, the t=15nm strut also shows evidence of higher dislocation plasticity, as compared to under tension, within numerous grains. Once again, grain boundaries that are more vertically aligned with the deformation axis show negligible strain accommodation. These same strain accommodation trends were observed in the other 4 nanocrystalline struts at each grain size as well.

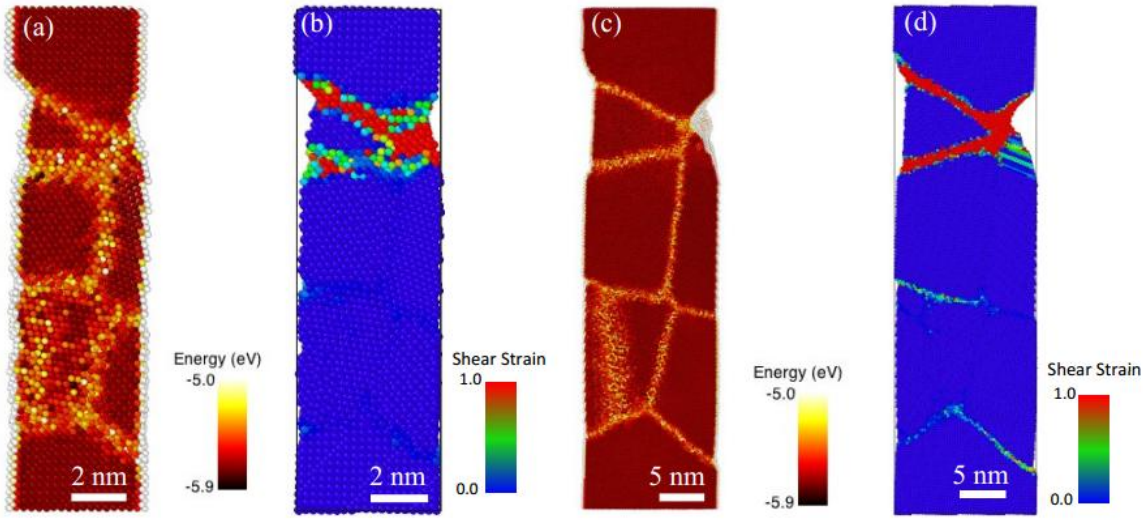

Figure 4.6 Nanocrystalline struts deformed under uniaxial tension (shown at 10% strain) in MD simulations with strut thickness (a-b) 5 nm and (c-d) 15 nm. For all cases D/t~1 and aspect ratio of t/l=1/3. Atoms are colored according to their (a)-(c) potential energy and (b),(d) shear strain.

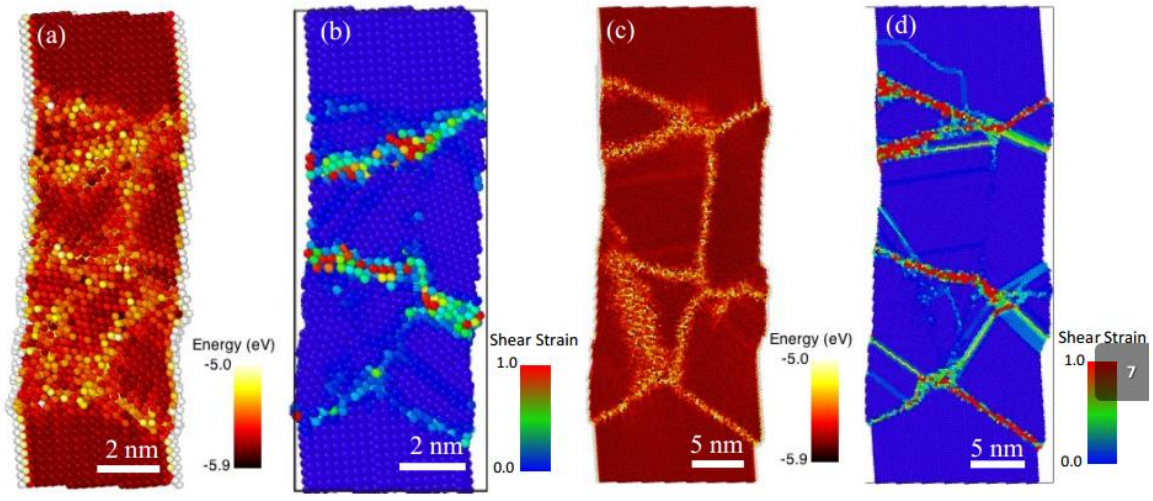

Figure 4.7 Nanocrystalline struts deformed under uniaxial compression (shown at 10% strain) in MD simulations with strut thickness t (a)-(b) 5 nm and (c)-(d) 15 nm. For all cases D/t~1 and aspect ratio of t/l=1/3. Atoms are colored according to their (a),(c) potential energy and (b),(d) shear strain.

Figure 4.8 shows the strength as a function of strut thickness for each set of nanocrystalline and single-crystalline struts tested in both tension and compression. The strength in the nanocrystalline struts was the averaged stress between 6 and 10 percent uniaxial imposed strain, while in the single-crystalline struts it was measured as the peak stress just following the elastic regime. Due to the high strain-rate requirement of these MD simulations, the calculated strength values of the struts are probably slightly higher than those that would be obtained from experiment on individual struts. However, the trends seen in the strength data provide tremendous insight into the deformation and mechanics of the individual struts. Figure 4.9 shows the strength asymmetry in tension and compression for the same struts. The asymmetry is large when struts are very small in diameter ($t = 2\ nm$) but the asymmetry decreases as the strut diameter is increased. For the case of t = 5 nm, nanocrystalline strut strength is nearly equal in tension and compression. The strength of the nanocrystalline struts decreases with decreasing *t* in

compression but increases slightly in tension. This trend is more pronounced in the single-crystalline nanowires, as displayed in Figure 4.8. Therefore, the single-crystalline struts with small values of *t* are characterized by more significant tension-compression asymmetry, than larger diameters and nanocrystalline struts as well. We note that the orientation of the single-crystalline struts plays a crucial role in determining their mechanical properties and the degree of tension-compression asymmetry. The [100] oriented grains exhibit a higher peak stress in tension than in compression, and the reverse is true for the [111] oriented grains. The single-crystalline struts tested in tension exhibit an increase in the peak stress with decreasing thickness. However, when tested in compression they exhibit a weakening with decreasing *t*. We note that these nanocrystalline simulations show a much higher strength than predicted by a model previously proposed for nanocrystalline platinum nanopillars [18] at D/t~1. Moreover, the simulations demonstrate presence of strut thickness effects independent of the relative grain size. Further research will be performed to fully understand the behavior of these struts at small sizes.

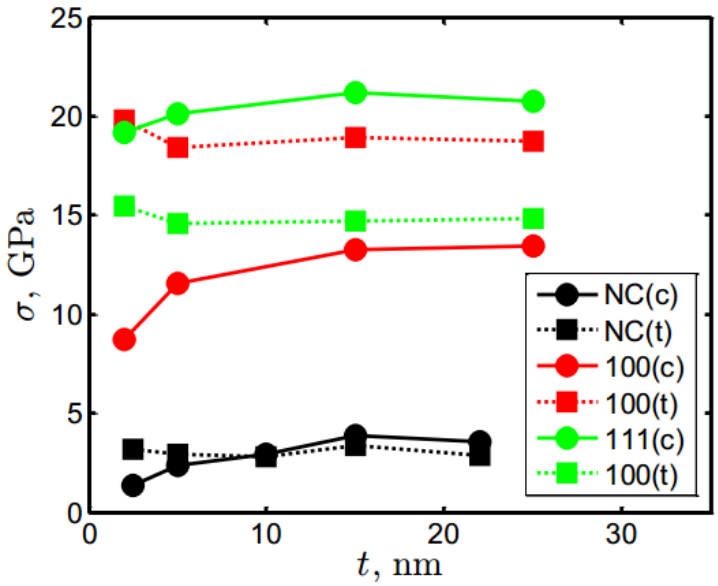

Figure 4.8 Strength calculated in MD simulations of nanocrystalline and single crystal struts tested under tension and compression. For all cases D/t~1 and aspect ratio of t/l=1/3. The peak stress is shown for the single crystalline struts. The flow stress is shown for the nanocrystalline struts.

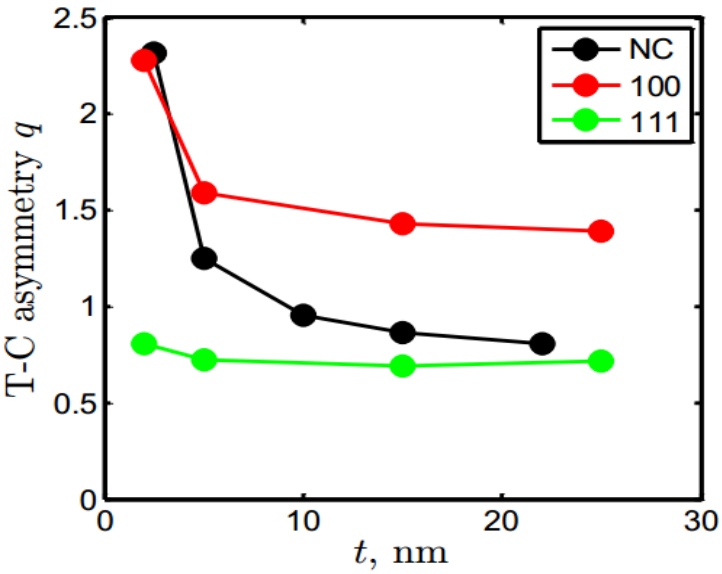

Figure 4.9 Tension-compression asymmetry from MD simulations of nanocrystalline and single crystal struts.

4.3.4 Estimates of strut strength

In the studies of NP metals, it is often assumed that the relation between the properties of individual struts and those of the overall network follow the same scaling relations as identified in low-density bulk foams. These scaling relations are then used to eliminate the contribution of the geometrical structure and to infer the properties of individual struts [15, 42, 116, 127]. As discussed in Section 3.1, the NP Pt is characterized by agglomeration of mass at the junctions, which breaks the traditional scaling relationship between strut geometry and the relative density. One way of interpreting this observation is that the use of traditional scaling relationships overestimates the strengths of the network for a given strut strength, since it effectively overestimates the strut aspect ratio (t/l). Conversely, when the scaling is used to infer the typical strut strength from measurements of the foam strength, the strength of the individual struts will be underestimated. As we will demonstrate shortly, this allows one to obtain non-trivial *low-bounds* on the strength of the individual nanocrystalline Pt struts.

For the purpose of completeness, we briefly review the dimensional analysis used to relate the mechanical response of the collective strut network to the deformation behavior of a single strut. In low density foams ($\bar{\rho}$ <0.1) the dominant deformation mode of struts is due to bending leading to [40]

$$H_f/\sigma_s = C\bar{\rho}^n. \tag{4.2}$$

where H_f is the foam hardness, σ_s is the strength of the solid struts, $\bar{\rho}$ is the relative density and $n = 1.5$ for bending mode. Such scaling relationships have been verified experimentally for a wide range of ordered and disordered bulk foams [40, 45]. For

simple ordered (periodic) structures one can also derive analytically the exact value of the proportionality constant C. At high relative densities ($\bar{\rho} \gtrsim 0.6$) theoretical arguments and experimental evidence suggest that the dominant deformation mode switches to axial strut yielding rather than bending [128]. At such high densities, strength scaling Eq. (4.2) is modified, so that $n \approx 1$.

Strut connectivity is another factor that can significantly affect the scaling Eq. (4.2). That is because in highly-connected networks the dominant deformation mode of individual struts switches to uniaxial compression/stretching even at low densities, leading to significantly enhanced weight normalized stiffness and strength[113]. While the mode switch to compression at lower densities is highly desirable, experiments and simulations have shown that random open cell, low density, isotropic foams are bending dominated due to the presence of defects e.g. missing cells, strut curvature, etc. that compromise overall mechanical properties [114].

In Eq. (4.2) the proportionality constant is defined as $C = C_H C_G$ and depends on a proportionality constant relating foam hardness to yield strength C_H and a constant that relates to the geometrical cell arrangement C_G, which may change depending on the deformation mode. The constants of proportionality are as follows:

(a) The hardness parameter C_H equals 1 for low density foams when the plastic poisson ratio is ~0 [129]. The hardness parameter is ~3 for a fully dense solid. In the case of NP metals with high relative density, experimental evidence suggests that $2 < C_H < 3$ [38].

(b) The geometrical parameter is well known for strut deformation under bending where $C_{GB} = 0.3$. [40] The value of the proportionality constant under compression is comparatively poorly understood, but existing data suggests that $0.3 < C_{GC} < 1$ [128].

The strut strength as inferred from the foam hardness measurements through Eq. (4.2) is shown in Figure 4.10 as a function of strut diameter for the NP Pt under assumption of strut deformation by (a) bending and (b) compression respectively. Data points in blue show the experimental data with the error bars showing the variation in strut thickness *t* and the variation in proportionality constant *C*. In Fig. 4.10(a) the experimental data are shown for the case where $C = 2.5 \times (0.3) = 0.75$ while the error bars show a 20% standard deviation. In Fig. 4.10(b) the experimental data are shown for the case where $C = 2.5 \times (0.65) \approx 1.6$; error bars show the range of possible *C* values in compression. For comparison, the flow stress and peak strength of nanocrystalline and single crystal struts from Molecular Dynamics (MD) simulations are included in Fig. 4.10. A fit to the experimental data shows that the inferred strength of NP Pt nanocrystalline struts scales with $t^{1.4}$.

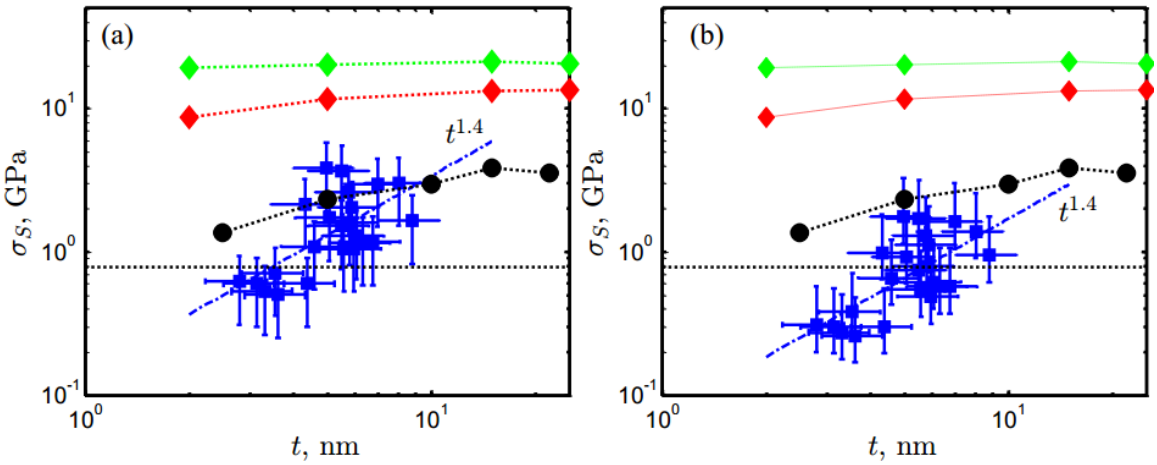

Figure 4.10 Inferred low bound on the strut strength of nanocrystalline NP Pt in comparison to the results of MD simulations. Prediction under assumption of strut deformation by (a) bending and (b) compression. For all cases, blue squares represent the experimental data, black circles are the MD simulations of nanocrystalline struts, green and red diamonds are the single crystal struts with (100) and (100) orientations respectively. The dashed horizontal line represents extrapolation of results in Ref. [81] to the thickness below 10 nm. Power law fits to the experimental data are shown.

*4.4 **Discussion***

The strength of NP metals is frequently assumed to follow a scaling of the type $\sigma_f \sim \rho^n t^m$, where ρ^n describes the influence of geometrical structure, while t^m captures the change in properties of individual struts with size. For example, an investigation of NP gold with micron-sized grains assumed $n = 1.5$ and inferred $m \approx -0.5$, indicating significant strengthening of the effectively single-crystal struts with decreasing diameter [71]. Another analysis of similar data suggested $n \approx 3.5$ and $m \approx -0.6$ [116]. In the analysis presented here, the assumption that the individual struts are deformed predominantly by either bending or compression ($n = 1.5$ and $n = 1$ respectively) yields a low-bound estimate of the properties of individual struts. In both cases, the fit of the dependence of the strength of individual struts yields $\sigma_s \sim t^{1.4}$. A direct fit of the hardness

of NP Pt to the scaling $H_f \sim \rho^n t^m$ yields $n \approx 0.35$ and $m \approx 1.4$, indicating a much weaker dependence on the relative density than is typically found, and a decrease in the properties of polycrystalline struts with decreasing thickness. This trend is well supported by molecular dynamics simulations that generally show a decrease in the properties of nanocrystalline struts under compression.

In principle, the relationship between the overall NP metals strength and that of individual struts could be expressed in terms of the geometrical parameters characterizing individual struts, such as their aspect ratio. For example, analysis of simple periodic structures finds $\sigma_f \sim \sigma_s (t/l)^3$ if the dominant deformation mode is bending and $\sigma_f \sim \sigma_s (t/l)^2$ if the dominant deformation is compression. However, we found that when such scalings are used to infer the strut strength of NP Pt struts with the direct measurements of *t* and *l*, they yield unrealistically high values that significantly exceed the results of simulations and even the theoretical strength limit for the very thin struts. Even more significantly, such analyses find that the inferred strut strength sharply *increases* with decreasing struts size. For example, under the assumption of compression $\sigma_s \sim t^{-2.1}$. This behavior is in clear contradiction to the results of MD simulations.

We conclude that the geometrical structure of the NP Pt plays a more complicated role in influencing its properties than previously appreciated. Indeed, the low-bound estimate of struts strength inferred from the hardness measurements under frequently used scaling hypothesis based on relative density predicts a somewhat sharper decrease in the properties of individual struts compared to the simulation results. In contrast, an estimate based on the direct measurements of (*t*/*l*) yields unrealistically high values and a sharp *increase* in the properties of struts with decreasing *t*, again in contradiction to the

simulations results. The true response describing the geometrical structure of NP Pt is therefore not captured by either of the scalings assumptions.

An interesting possibility to better understand the influence of geometrical factors is to accept the molecular dynamics simulation results as the property of polycrystalline struts and to infer the geometrical scaling by fitting experimental data to an assumed model. Towards this end, we have interpolated the simulation data points in Fig. 4.10 by a cubic polynomial and performed the fit of $H_f/\sigma_s^{MD}(t)$ to the function of the form $C_1(t/l)^2 + C_2\, td/l^2 + C_3(d/l)^2$. Here $\sigma_s^{MD}(t)$ is the interpolated strength in MD simulations and $C_{1\text{-}3}$ are fit parameters. This results in C_1=2.7, C_2=20.5, and C_3=-1.5. The rationale behind the choice of the fitting function is that due to the mass accumulation in junctions, the scaling should be a function of both strut thickness *t* and the junction thickness *d.* The chosen fit function is the first few terms of the expansion of the unknown scaling function in powers of (*t*/*l*) and (*d*/*l*). Including terms up to the second order in (t/l) implies that we are assuming that individual struts deform predominantly under compression. We have verified that the proposed model gives a better fit to the data than simple functions of the relative density or strut thickness alone, as assessed by the value of adjusted coefficient of determination R^2. The significance of the presented scaling is perhaps not in the precise value of the fitting constants or in the specific choice of the scaling function, but rather in the fact that it illustrates that mass agglomeration at the junctions needs to be accounted for in models describing the geometrical response of NP metals.

An interesting result of the simulations is a tension-compression asymmetry of individual struts. Such asymmetry can influence the scaling of foam properties, leading

for example to strengthening of the bending mode. Indeed, analysis of asymmetric yielding in beams demonstrated that the yield strength is modified by a factor of $2q/(q+1)$ in this configuration, where $q = \sigma_y^T/\sigma_y^C$ is the ratio of yield strength in tension to that in compression. As such, the struts made of materials exhibiting large asymmetry can be up to 2 times stronger compared to the ones where yield strengths under tension and compression are equal. When such factor is included in the analysis of the bending mode (Fig. 4. 10(a)), the inferred strength of the struts decreases even faster with the thickness, approximately as $t^{1.7}$.

4.5 ***Conclusions***

1) An amorphous platinum silicide alloy with residual compressive stress was dealloyed under different externally applied potentials. The resulting NP Pt was nanocrystalline with randomly oriented grains that are approximately equal to the strut thickness. The amorphous state of the initial alloy promotes the nucleation of the nanocrystalline grains within the struts. Furthermore, the combination of residual compressive stress and externally applied potential produces crack-free samples with struts that have varying spatial arrangement e.g. different length, junction size, etc.

2) NP Pt hardness assessed via nanoindentation is 0.2-1.25 GPa for struts in the 3-10 nm range. The hardness decreases with decreasing average thickness of the struts, but the dependence on aspect ratio (*t*/*l*) is much weaker than the expectations drawn from a simple dimensional analysis.

3) Atomistic simulations for 5-15 nm struts show that the flow stress weakly decreases with strut diameter for nanocrystalline Pt struts under compression, but remains in the range (2-4) GPa.

4) A low bound estimate of the individual nanocrystalline Pt struts produces somewhat lower values for the strut strength and predict and a stronger decrease in strength with decreasing strut thickness t that predicted by simulations. On the other hand, an estimate based on direct measurements of strut thickness (t/l) yields unrealistically high values of the strength that increase with t. With thus conclude that the effects of NP Pt geometry are not properly captured by existing scaling relationship and much more careful analysis is required. Since many of the parameters controlling properties of NP metals may be influenced by the synthesis mechanism, their identification will pave the path for informed design of NP metal with desirable characteristics.

CHAPTER 5

SYNTHESIS AND MECHANICAL BEHAVIOR OF NANOPOROUS NANOTWINNED COPPER

5.1 ***Introduction***

In this letter we report on the synthesis and mechanical properties of nanotwinned nanocrystalline nanoporous copper (NT/NC/NP Cu). It has long been recognized that nanoporous (NP) metals are characterized by an abundance of free surfaces that on the one hand makes them highly attractive in many applications [2, 4-6, 8-10, 77, 130-132] and on the other hand gives rise to a highly unusual combination of physical properties. For the most part, existing analyses of mechanical properties of NP metals ignore the influence of the internal structure of struts, in part because for such well-studied systems as NP Au the individual struts are effectively single crystal [11, 16, 41]. In contrast, NT/NC/NP Cu reported here is characterized by a highly complex internal structure with overlapping characteristic length scales for individual elements such as struts, grains, or twin boundary spacing. The presence of such intricate microstructure is intriguing both from the fundamental point of view and in light of the possibility that it can give rise to significant enhancement of global physical properties, as is known to be the case for other nanostructred metals. For example, experimental observations of bulk pure copper containing either grain or twin boundaries show that it attains high strength as the size of the grain (d) or the spacing between twin boundaries (λ) is in the nanometer range [133]. While decreasing grain size (d) severely affects ductility, a decrease of the spacing

between twin boundaries enhances both strength and ductility [133]. Similarly, atomistic simulations have shown that copper nanowires with twin boundaries exhibit considerably increased strength when compared to twin-free wires, independent of loading condition [134]. On the other hand, presence of a complex microstructure is not always beneficial. It has been known for some time that Hall-Petch scaling saturates as the system size becomes comparable to the grain size [135]. Recent experiments of single crystal copper nanopillars (diameter, D = 50 nm) with twin lamella (λ~1.2 nm) have demonstrated that strength can also decrease depending on the orientation of the loading axis with the crystallographic axes of the nanopillar [136].

In summary, it might be expected that the mechanical (and other physical) properties of nanotwinned nanocrystalline NP Cu significantly deviate from those of other NP metals opening possibilities for material design through optimization of the internal structure. The ability to manipulate properties of NP metals to suit specific applications (e.g. to enhance strength and ductility) is crucial for advancing applications of these intriguing materials. In this Letter, we experimentally assess the hardness of NT/NC/NP Cu and demonstrate that it is significantly enhanced compared to other NP Cu systems previously reported in literature. The origins of this enhancement are traced back to a combination of factors, including the geometry of NP Cu and the enhancement of properties of individual struts compared to bulk Cu.

5.2 ***Experimental Methodology***

The NT/NC/NP Cu was synthesized via a two-step process. First, amorphous copper silicide $Cu_{0.61}Si_{0.39}$ thin films (film thickness, t_f = 1.5 μm) were co-sputtered on

(100) silicon substrates. The deposition was performed with a base pressure of $5x10^{-8}$ Torr and a bias of 100 V. The deposition conditions were tuned to yield thin films under residual compressive stress of 160 MPa. The magnitude of the stress was measured using laser curvature measurement of rectangular silicon bars before and after deposition of the copper silicide film and was found to be 160 MPa. The composition of the initial alloy was determined using X-ray Photoelectron Spectroscopy (XPS) of films deposited on a carbon substrate using identical deposition conditions. NP Cu was synthesized from the amorphous silicide by dealloying, whereby silicon was preferentially dissolved in the electrolyte leaving behind copper that assembled into open cell foam, i.e. a three dimensional network of struts. All but one of the copper silicide samples were electrochemically dealloyed at room temperature in an aqueous solution of 3% HF under an externally applied voltage in the range of 0.1- 0.25 V. This results in samples with typical strut thickness in the range approximately 20-40 nm. NP Cu samples dealloyed at lower potentials have finer strut dimensions than samples dealloyed at higher potentials. The sample with the smallest strut thickness (t~19 nm) was synthesized at 0.1 V in an electrolyte bath cooled to approximately 0 ℃. The low temperature promotes smaller struts as examined previously for NP Au [137]. Finally, samples with average strut thickness 40-80 nm were obtained by first synthesizing NP Cu in the room temperature electrolyte at a V = 0.1 V and then allowing it to coarsen in the electrolyte bath for 10, 40 and 80 min. As synthesized NP Cu contained no silicon to within the resolution limit of the technique (0.1%). This is consistent with our prior results on NP Pt, which also demonstrated complete removal of Si during dealloying [28].

All samples were characterized using plan and tilt SEM views using a Zeiss Ultra60 FE-SEM. Strut dimensions were obtained by further analysis of the micrographs [69]. Analysis of the SEM micrographs revealed that struts were elongated in the through thickness direction as compared to the plan view. Figures 4.1(a) and (b) show 45 ° SEM tilt views of the free surface and side view respectively, of a representative sample of NP Cu synthesized at a potential of 0.25 V. The sample has an average strut thickness of 29 nm and length of 29 nm in the plan view and length of 95 nm in the through thickness direction. The elongation of strut through the film thickness was consistently observed in all samples regardless of dealloying conditions.

5.3 ***Results and Discussion***

Two samples were also examined using Transmission Electron Microscopy (TEM). Figure 5.1(c) and (d) show cross-section TEM micrographs of the NP Cu sample shown in Fig. 5.1(a) and (b). Figure 5.1(d) is an enlarged view of the dotted box shown on Fig. 5.1(c). Multiple nanocrystalline grains are visible within each strut with an average size equal to the strut thickness (~29 nm). It is apparent from Fig. 5.1 (d) that a large population of twin boundaries exists within the grains with average twin spacing (λ) of 7 $\pm$ 3 nm. TEM analysis did not show the presence of any oxide forming on the free surface. This is remarkable given that the samples were analyzed approximately two months after they were synthesized. We note however that other studies of NP Cu also did not find an

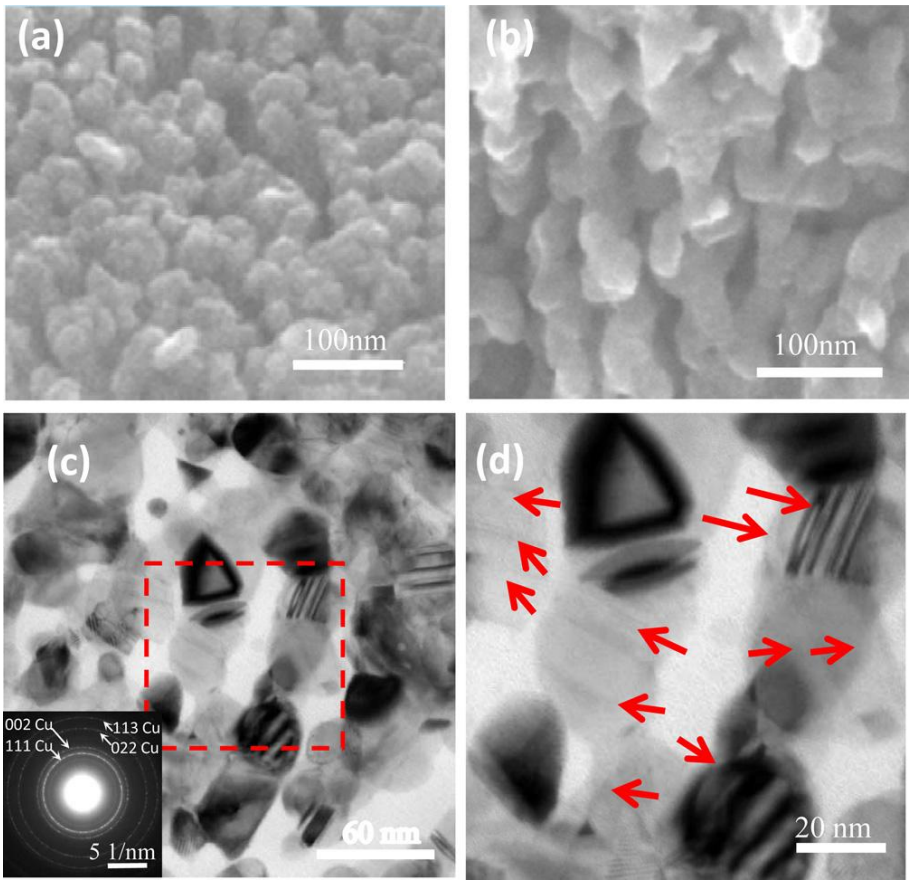

Figure 5.1 Micrographs of NP Cu with hardness of 370MPa obtained by dealloying Cu0.61Si0.39 at V = 0.25V. SEM 45° tilt views (a) of the free surface and (b) cross-section. (c) and (d) Cross-section TEMmicrographs showing multiple grains with twin boundaries. Grain size is ∼29nm and average twin spacing is ∼7 nm. The inset of Fig. 5.1(c) shows the corresponding SADP. The TEM of Fig. 5.1(d) is a close-up of the box highlighted in Fig. 5.1(c).

oxide layer in as-synthesized samples [138]. An insert in Fig. 5.1(c) shows the Selected Area Diffraction Pattern (SADP) of a region the size of afew micrometers. The TEM images indicate that the grain and twin orientation is random since the selected area diffraction pattern (SADP) shown in the insert of Fig. 5.1(c) is comprised of rings of uniform intensity. However, it is not possible to conclude from SADP analysis if the random orientation of grains is a geometrical effect related to random arrangement of struts or if grains are truly randomly oriented within struts. A preferential orientation of grains may significantly increase the strength of individual struts. For example, it has

recently been shown that Cu nanopillars with twin boundaries oriented perpendicular to the loading axis exhibit higher yield strength than their single-crystal pillar counterparts [134, 136].

The mechanical response of NP Cu was obtained by nanoindentation using a Hysitron Triboindenter equipped with a Berkovich tip with radius of ~150 nm. Arrays of 25 indents of varying depth 40 μm apart were performed on each sample and the hardness was obtained from the unloading curve slope of each indent using the procedure outlined by Oliver and Pharr [90, 91]. The reported NP Cu hardness is the average hardness obtained from unloading curves of indents with indentation depth within 30% of the NP Cu thickness and equivalent to two to five pore sizes so as to avoid underestimating the hardness at shallow depths. Within that indentation range the effect of the substrate should be minimized [121]. Figure 5.2 shows a plot of NP Cu hardness as a function of strut thickness for samples synthesized using the procedure reported here. The datasets in red are NT/NC/NP Cu with diamond symbol denoting samples that underwent further coarsening in the electrolyte. For comparison, we also included results on NP Cu published by other researchers [31, 138, 139]. None of the previous studies of NP Cu reported presence of grains and/or twin boundaries within the struts. Our NT/NC/NP Cu has hardness in the range of 0.3 to 1.3 GPa, depending on strut thickness. The NT/NC/NP Cu exhibit at least one order of magnitude increase in the hardness when compared to previously reported NP Cu with struts in the similar thickness range of 40-80 nm [31, 138, 139]. Therefore, the order of magnitude enhancement observed for NT/NC/NP Cu is not due to variations in the relative density[22].

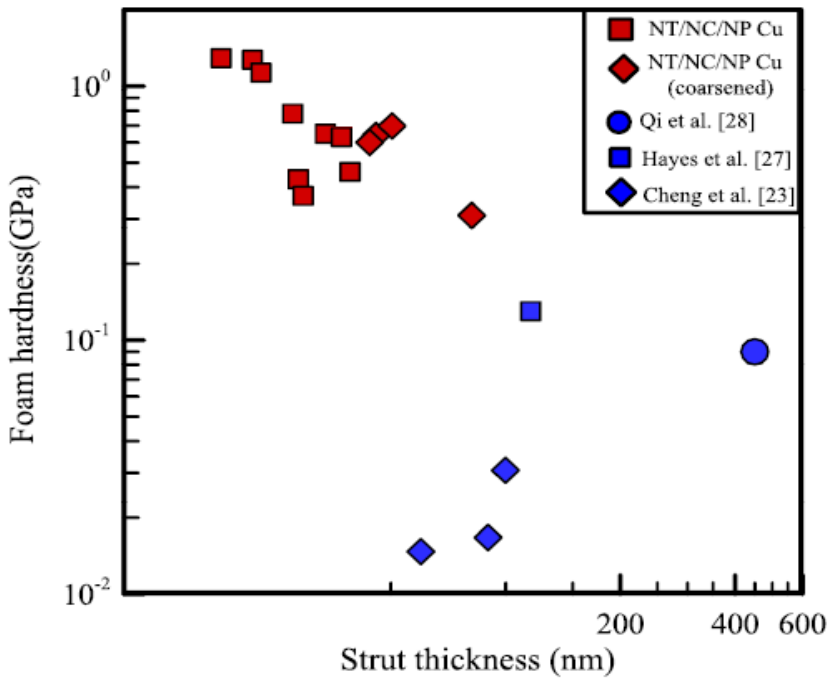

Figure 5.2 Foam hardness of NP Cu as a function of strut thickness. NT/NC/NP Cu from $Cu_{0.61}Si_{0.39}$ exhibits at least one order of magnitude greater foam hardness when compared to the data in existing literature [31, 138, 139].

At least partially, the relative high hardness of NP Cu is due to the geometric structure of the NT/NC/NP Cu discussed here. As is apparent from SEM images shown in Fig. 5.1(a) and (b), our synthesis procedure results in NT/NC/NP Cu with struts and pores elongated in the through thickness direction. Several studies that examined the effect of cell shape on the properties of large-scale foams indicated that such anisotropic structures have higher strength. For example, Gibson and Ashby reported that elongated cells such as those found in cork are stiffer and stronger when loaded along the long axis of the cell than when loaded across it [40]. While the material deforming underneath the indenter is under a complex state of stress, it is well documented that the overall hardness measurements for an isotropic material are related to the yield strength under uniaxial compression [40, 140].

In order to infer the properties of individual struts from the hardness measurements, we use dimensional analysis that correlates the mechanical response of the collective strut network to the deformation behavior of a single strut. A crucial distinction of the analysis outlined below from many similar investigations is the assumption regarding the dominant deformation mechanism. Using results well-established for irregular *low-density* foams, most of the previous investigations of the mechanical properties of NP metals assumed that the structure deforms and fails by strut bending. However, at high relative densities (>50%) compressive mode [40, 128, 141] dominates over bending. The NP Copper has a density in the range of 45%–65%, corresponding to the transition between the two modes so that the dominant mode is a mixture of the two pure deformation mechanisms. Assuming purely compressive mode of strut failure therefore yields a low bound estimate of the strut strength.

Under the assumption of strut yielding by compression and an anisotropic unit cell with larger strut length in one direction (as shown in Fig. SM 4.3), the ratio of foam hardness to dense solid strength, H_f/σ_s becomes

$$H_f/\sigma_s = C(\mathrm{t/l})^2 \tag{5.1}$$

where H_f is the hardness of NP Cu, σ_s is the strength of the solid strut, *t* and *l* are the strut thickness and length in the in-plane direction. The proportionality constant $C = C_G C_H$, takes into account both the geometry of the unit cell (C_G) as well as the ratio of strut hardness to strength (C_H). Briefly, we use dimensional analysis [40] to derive an expression for H_f/σ_s in terms of the ratio of strut length *(t/l)*. Eq. (5.1) is then obtained from the scaling of relative density with (t/l). A large body of existing work on porous

media of different scales has utilized this approach in order to obtain semi-empirical scaling of various physical properties with relative density. This work both confirmed the validity of the basic approach and provided insights into the typical range of values of the constant C. We use Eq. (5.1) in order to estimate the strength of individual struts ersT from the foam hardness. Since the exact value of the empirical constant C is not known for the NP Cu foam, we assume that the geometric constant lies in the same range as found in multitude of previous investigations $0.3<C_G < 1$. Typically, random foams have $C_G \sim$ (0.3 - 0.4) [40, 45]. The other constant is assumed to take values $1 < C_H < 3$, where 1 corresponds to the case for low density foams with plastic poisson ratio of 0 and $C_H \sim 3$ corresponds to dense solids [16, 40]. Thus, the overall constant C in Eq. (5.1) is assumed to be in the range $0.3 < C_G < 3$. We provide an estimate of rs by taking a reasonable choice of C = 0.6 with error bars corresponding to extreme values of C = 0.3 and C = 3. Note that $C \sim 3$ is highly unlikely for this system, since this would correspond to a perfectly periodic structure with minimal porosity. While such inversion of Eq. (5.1) is subject to considerable uncertainty, it suffices to place non-trivial bounds on the strut strength. Similar procedures have been used by other researchers in the work of NP metals [11, 41, 71], often without giving consideration to the fact that value of C may vary. Finally, it has been noted by several authors that the relation between relative density and t/l is often more complicated by what is assumed by simple dimensional analysis. Indeed, we find that NP Copper hardnessHowever, we find that estimating rs from a direct measurement of (t/l) yields very similar range of values to the one reported here, largely due to considerable uncertainties in both measured (t/l) and the

corresponding constant C. We note that the estimate of rs from (t/l) explicitly takes into account the anisotropy of the structure.

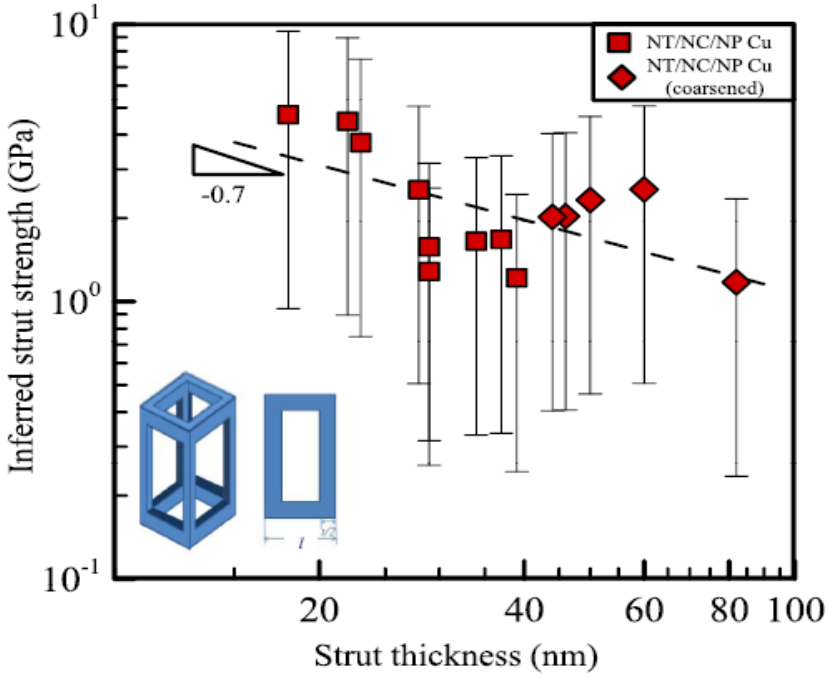

Figure 5.3 Inferred strut strength of NP Cu as a function of average strut diameter using dimensional analysis. The inset shows the type of elongated unit cell used in the analysis. The error bars show the range of possible strut strength for proportionality constant C in the range of 0.3 to 3 and the dotted line shows the exponent of a power fit of the data.

Figure 5.3 shows the NP Cu strut strength as a function of strut thickness inferred from the foam hardness measurements using Eq. (5.1). The error bars denote the extrema of the constant *C*. The strut strength for the smallest (18 nm) and largest (82 nm) strut diameters are found to be 2.8 GPa and 0.3 GPa respectively. A power fit to the data gives,

$$\sigma_s = t^n \tag{5.2}$$

with $n \approx -0.7$. It is instructive to compare the inferred properties of struts to those reported for other copper nanostructured systems, including nanopillars [136, 142], nanowires [143, 144] or even bulk nanograined [133, 135, 145] and nanotwinned [145] copper. This comparison is reported in Figure 5.4. The dashed line for bulk Copper is reported for grain size of 100μm [133]. The extracted strut strength values are within the same range as reports in the literature for single crystal copper nanopillars and nanowires. For the same characteristic size in the range of 20-80 nm, the strut strength of NP Cu decreases somewhat sharper than the atomistic simulation prediction of bulk nanograined copper but it is well within the range of other bulk nanotwinned systems [133] and well above the strength of bulk copper. It is important to emphasize again that the assumption of strut failure by compression produces a low bound estimate on the strut strength properties.

While the precise role of the nanotwin boundaries and grains on the strut and foam network properties cannot be precisely obtained from nanoindentation experiments alone the work presented here demonstrates that the more than one order of magnitude enhancement in foam hardness is likely due to a combination of the geometric structure and the enhanced strength of the nanotwinned, nanograined struts. Since the extracted properties of the NP Cu struts are within the same range as the properties of other nanostructured copper systems and especially of nanotwinned systems, we anticipate that the presence of twins may indeed enhance other properties of NP metals such as ductility. Enhancing ductility of NP metals is of great interest in light of the frequently reported presence of nano- or micron-sized cracks that may be inherently associated with the synthesis technique and can adversely affect the tensile behavior of NP metals.

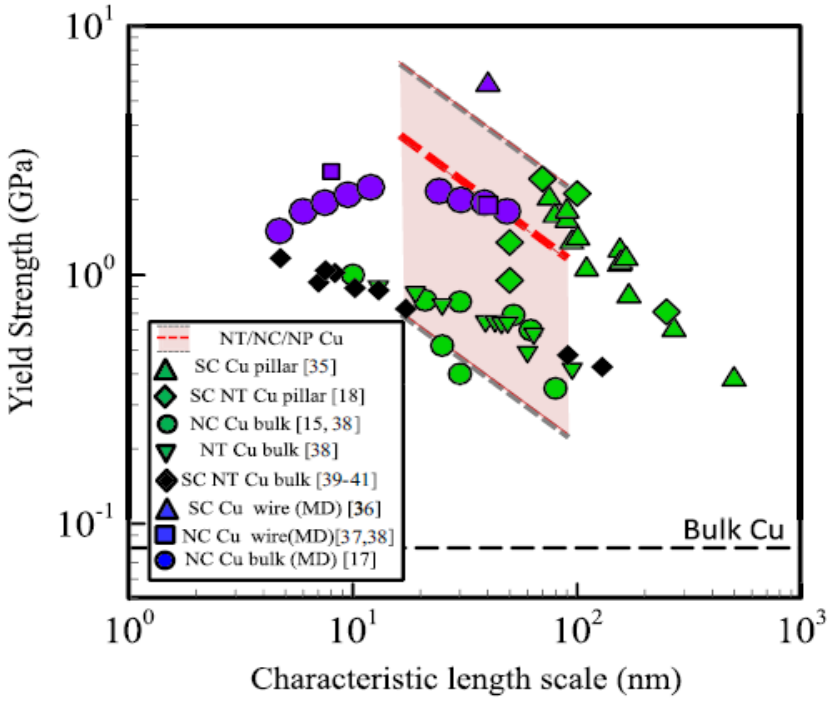

Figure 5.4 Inferred strut strength σ_s of NT/NC/NP Cu (shaded region) compared to other nanostructured copper systems (symbols). The shaded region is bound by power-law fits to the estimated minimum and maximum values of rs (corresponding, respectively, to C = 0.3 and C = 3 in Eq. (5.1)). The dashed red line is a power-law fit to σ_s obtained with C = 0.6. Symbols of green color represent electrodeposited samples, black corresponds to sputtered and blue to MD simulations. Characteristic scale is diameter for NP Cu struts, nanopillars, nanowires; grain size for bulk nanocrystalline copper; and twin spacing for bulk nanotwinned copper. The horizontal dashed line shows the strength of polycrystalline copper with grain size of 100 μm from Ref. [133].

5.4 ***Conclusions***

In summary, this work reports the synthesis of NP Cu from a copper silicide alloy with a residual compressive stress. The resulting nanotwinned, nanograined nanoporous copper exhibits a sixty-fold increase in foam strength when compared to the reports in literature. The yield strength of individual struts inferred through dimensional analysis greatly exceeds yield strength of bulk copper and compares well with other nanostructured copper systems that have been reported in the literature. While no

unequivocal conclusion regarding the role of grain structure and the presence of twins can be reached at this time, these results suggest that internal structure of struts is a least partially responsible for the observed increase in mechanical properties of foam. It remains to be seen if other favorable properties of nanotwinned systems, such as high ductility, are also present in this NP Cu system.

CHAPTER 6

ELECTROCHEMICAL DEALLOYING SYNTHESIS AND CHARACTERIZATION OF NANOPOROUS COPPER BY NANOINDENTATION

6.1 ***Introduction***

Nanoporous (NP) metal foams are a unique class of materials composed of a three-dimensional network of nanosized struts. They are characterized by extremely high surface-area to volume ratio and possess desirable properties such as high electrical conductivity, catalytic activity and ultrahigh strength. This unusual combination makes them ideal candidate for many scientific and engineering applications including catalysts [77, 146], sensors [8, 147], supercapacitor [2, 130], electrodes of batteries [131] and small-scale actuators [110, 148]. It has been previously shown that the formation of nanoporous copper retaining its original lattice structure can be created through a dealloying process so that the individual struts are effectively single crystal; however, few studies have been conducted on NP copper with nanocrystalline structures. Moreover, the morphology of NP metal and ligament sizes can be tailored by the dealloying potential and time [10, 13, 67, 69], election of electrolyte [31], post-annealing [35, 36] and immersion [112]. However, the synthesis of NP metal usually involves many factors so that it is difficult to study the effect of single factor while excluding the interaction effects of other factors. J.R. Hayes et al. reported the fabrication of monolithic

nanoporous copper from a single phase $Mn_{0.7}Cu_{0.3}$ under electrochemical dealloying and free corrosion with different electrolyte. They observed a strong influence of dealloying electrolyte on the final pore structure and demonstrated porous copper with ligament as small as 16nm was obtained at applied potential [31]. Compared to free corrosion, application of such potential to the alloy in the dealloying process enhances the less noble element dissolution rate relative to the more noble element diffusion rate, leading to finer ligament sizes [44]. E. Desti et al. reported the size of ligament and pore sizes decreases with increasing applied potential [13]. However, in their studies, different dealloying time takes 1 hour for high potential, whereas 15 hours was employed for low potential. Coarsening of porous structure driven by surface energy reduction occurs at the same time as dissolution [67]. Therefore, the decrease in ligament\pore size is a result of a reduction of the dealloying time so that the atoms will not have enough energy or time to diffuse and aggregate into bigger clusters. In this chapter, we demonstrate that nanocrystalline/nanotwinned/nanoporous (NC/NT/NP) copper with strut sizes 20nm to 110nm can be synthesized by dealloying from amorphous alloys obtained by magnetron sputtering and compare the results of NP Cu from $Cu_{0.41}Si_{0.59}$ (set A) and $Cu_{0.45}Si_{0.55}$ (set B) by atomic ratio. Additionally, we employed a range of different potentials to synthesis crack-free NP Cu with the same period of time. The experiment results show the morphology and ligament size of NP Cu are highly depend on the initial alloy composition as well as the overpotentials.

Moreover, mechanical properties including hardness and modulus were characterized with nanoindentation and their correlations with strut dimensions were discussed. The abundance of free surfaces and the nanoscale size of gains and struts give

rise to the unexpected properties of NP metals. Most studies have been focused on study the structure-property relationship of NP metal foams with isotropic open cell structure [11, 38, 42, 44, 71]. The relative foam modulus relates to the relative density as $E_f/E_s \propto (\rho^*)^m$. The relative foam strength can be found to scale as $\sigma_f/\sigma_s \propto (\rho^*)^n$. When the deformation mode shifts from bending-dominated to compression-dominated, the exponent m and n decreases from 2 to 1 and 1.5 to 1, respectively. Therefore, good estimation of the properties of struts needs precise measurement of relative density as well as exponent, which are normally difficult to do so because the complexity of geometry such as cell arrangement, irregularity, connectivity number. By noting that even with the same geometry, the deformation mode can shift from bending dominated to compression dominated with increasing in the relative density. Here, we demonstrate the fabrication of NP Cu composed of nanosized clusters. Such distribution of mass is distinct different from conventional foams since they don't have long struts which are prone to bend under loading. Unlike isotropic nanoporous metals which are most widely studied, the deformation of NP Cu synthesized using our method is compression dominated rather than bending dominated. We proposed a modification to the dimensional analysis that can infer the properties of those clusters.

*6.2 **Experimental Methodology***

NP Cu was synthesized via a two-step process. First, $Cu_{0.41}Si_{0.59}$ (Set A) and $Cu_{0.45}Si_{0.55}$ (Set B) by atom percentage with a thickness of 1.7-2.2 μm were co-sputtered using pulsed DC magnetron sputter on silicon substrate with Argon gas pressure of 5 x 10^{-8} Torr. Substrate bias 100V was applied during the deposition and average compressive residual stress in the order of 100MPa was introduced. As discuss in our

previous paper [100], this compressive stress is very important to reduce the tensile stress generated during the dealloying and thus reduce the cracks formation. Then NP Cu was synthesized via electrochemical dealloying with 3% hydrofluoric acid as the electrolyte using a three-electrode electrochemical cell at room temperature. The composition of initial amorphous thin film alloy was determined by using X-ray Photoelectron Spectroscopy (XPS). After dealloying, Si was completely removed. We note that TEM analysis did not show the presence of any oxide layer in as-synthesized samples [112]. The film thickness was measured by profilometer. Critical potential was determined by the Voltammetry and then different applied potentials beyond the critical potential were selected in the work to study the influences of potential on the nanostructures and mechanical properties of NP Cu. Finally, 4-6 samples of NP Cu dealloyed at the same condition from each alloy (0.1V for set A and 0.25V for set B) were coarsened by immersion into the electrolyte for 10-90 mins.

Both top view and cross section view of each sample were obtained using a Zeiss Ultra60 FE-SEM to characterize the morphology and microstructure of NP Cu. Strut diameter and length were measured taken directly from SEM images. Detailed procedures of the measurement were described in our previous work [69]. The film thickness and struts dimensions measured based on tilted images were corrected. The mechanical properties of NP Cu were obtained by nanoindentation with a Berkovich tip with radius of 150 nm. Arrays of 25 indents with 40 μm apart were performed on each sample. The reported NP Cu modulus and hardness is the average value obtained from unloading curves of indents with indentation depth within 30% and equivalent to two to five pore sizes so as to avoid underestimating of the NP Cu thickness.

6.3 ***Results and discussion***

6.3.1 Physical and structure characterization

Both alloys were electrochemically dealloyed in 3% HF solution. Voltammetry study with a linear potential sweep of 30 mV/s was performed on each sample. A corresponding potential sweep for a pure copper film is shown for reference. Results show the critical potential equals -0.46 V and 0.2V for set A and set B, separately. As can be seen in Fig. 6.1, the current density and dealloying rate is much higher for set A than set B for the same applied potential. For example, at V=0.2V, the current density for set A is 10 times larger than set B. The critical potential increases as the composition of noble element increases, in agreement with other people's observations [149]. But it is unlikely the only reason to explain such difference in critical potential. Other factors such as residual stress and strain may affect the kinetics of dealloying. The dissolution of Zinc and copper from 70/30 brass can be accelerated considerably with increasing tensile stress [150]. For the same conditions such as gas pressure and substrate bias, the compressive stress in deposited films is a function of film thickness. Dector et al. [151] reported that residual tension stress increases by approximately 0.5GPa when the film thickness increases from 1.6 μm to 2.1 μm. This stress state may cause the difference in the ease of electrochemical dealloying through mechanisms such as stress assisted corrosion [150, 152]. Additionally, we observed cracks formation and peeling off of thin film from its substrate when the applied potential reaches 0.55 V. This value is close to the standard oxidation potential for pure planar Cu (0.58 V). This indicates any potential larger than that value may result in dissolution of copper into the electrolyte. Hence, in order to synthesis NP Cu with consistent and good quality, the potential we can apply on

the sample varies between its critical dealloying potential and 0.55V. As a result, the range of overpotential V_r that can employed to generate crack-free nanoporous copper is 1 V and 0.35V for set A and set B, separately.

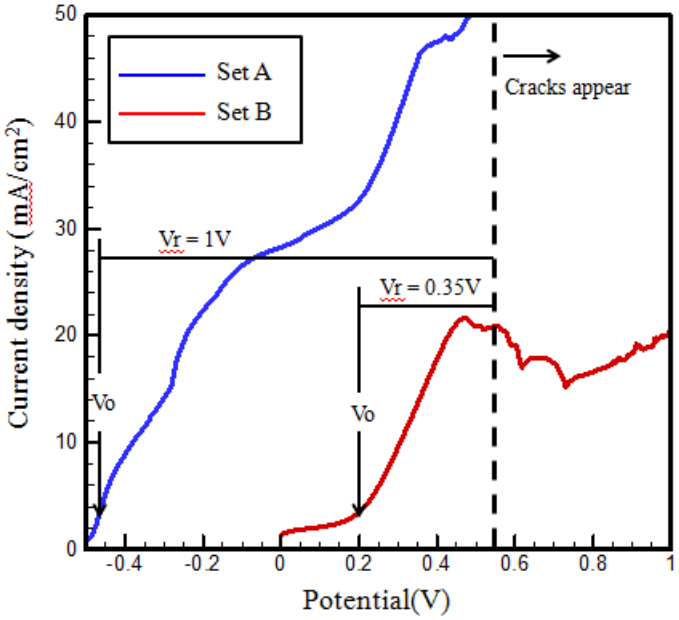

Figure 6.1 Electrochemical dealloying of NP Cu using a linear sweep at 30 mV/s. The critical potential is about 0.22 V and -0.5 V for $Cu_{0.45}Si_{0.55}$ and $Cu_{0.41}Si_{0.59}$ separately. The dashed line corresponds to V=0.55V. When V > 0.55V, cracks and dissolution of copper into electrolyte may occur.

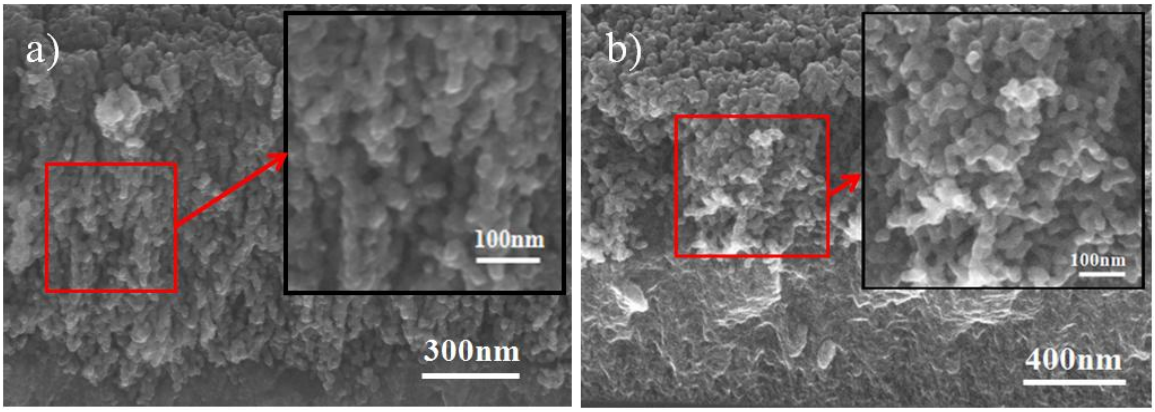

Figure 6.2 SEM 45° tilted images of NP Cu. (a) sample from set A dealloyed at 0.1V, b) sample from set B dealloyed at 0.25V. Dealloying time for both samples are 100s.

NP Cu with different microstructure could be synthesized by electrochemical dealloying from Set A and B. The morphology of the dealloyed NP Cu was investigated in detail using SEM. Figure 6.2(a) shows the SEM image of NP Cu from set A at applied voltage of 0.1V. The inset of Fig. 6.2(a) shows the nanoscale structure of long ligaments enlongated through thickness direction. By contrast, no such structure was found for Set B. Figure 6.2(b) shows nano-sized clusters metal clusters randomly formed on the surface instead of having long ligaments with specific orientation. Additionally, the ligaments length of set B is close to its width, usually below 40 nm, whereas long ligaments as long as 120 nm are observed in Set A. For all samples, the average grain size within the ligament is approximately equal to the ligament width. A large amount of twins were found in those grains which are believed to play an important role in the enhancement of plasticity.

In addition, EDS/XPS were employed to characterize the elemental and chemical compositions of nanoporous copper foams. Our results demonstrate that all of silicon was removed during dealloying. As can be seen from Fig. 6.3(b), the counts of O1s drop dramatically after 60s of Ar+ sputtering and the chemical composition becomes independent of depth. If the presence of oxide is attributed to the formation of copper oxide, the XPS results gives the atomic ratio of copper and its oxide (Cu: 89.4%, Cu_2O: 10.6%). The presence of copper (II) oxide is very unlikely because no strong Cu2+ satellite is observed. However, the binding energy of copper and copper (I) oxide are sitting in a narrow range (932.6-933.1eV) so it could be difficult to differentiate the chemical states only from XPS results. Additionally, oxygen will always be present on samples exposed to the atmosphere, either due to contamination, oxidation or water.

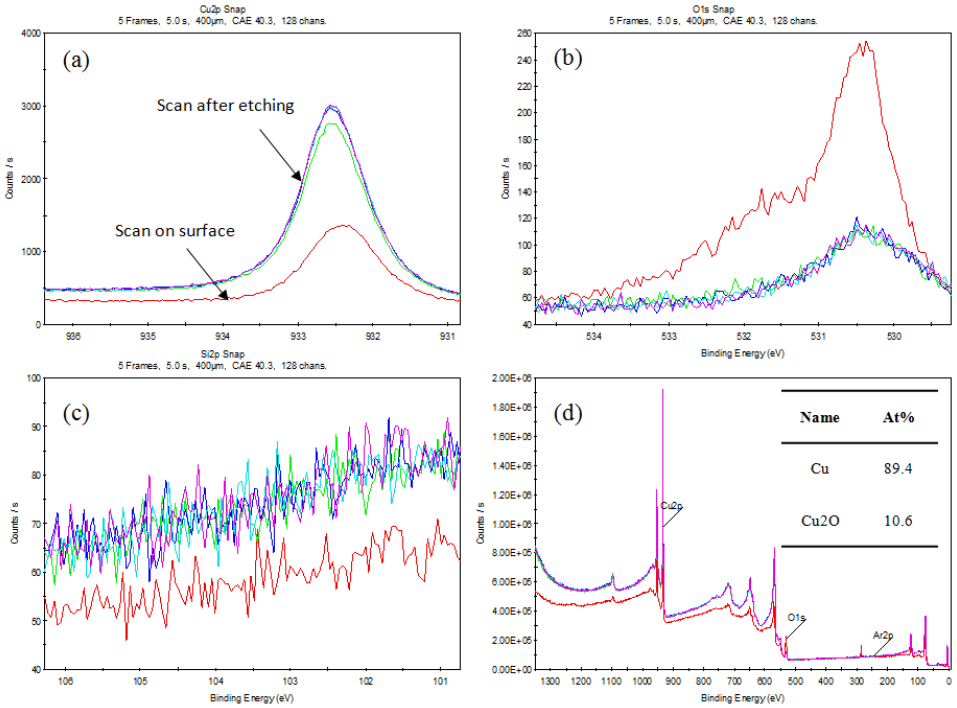

Figure 6.3 XPS spectra of NP Cu after 0, 60, 120, 180, 240s of Ar+ sputtering. (a) Cu2p3/2, (b)O1s, (c)Si and (d) survey scan

To investigate the voltage dependence of the geometry of ligaments during dealloying, samples were subjected to a range of applied constant potential over the same period of time (100s). After the dealloying process, all samples were characterized using SEM. The corresponding changes in the average ligament length, diameter and aspect ratio as a function of overpotentials are displayed in Fig. 6.4(a), (b) and (c), respectively. The data set in green circle are samples from set A. The data set in red square are samples from set B. For each specimen, the clusters sizes were measured manually by randomly selecting at least 30 clusters and making measurement and then averaging. Fig. 6.4 (a) shows that the strut diameter as a function of overpotentials. For both alloys, the ligament diameter increases considerably with increasing in overpotential. Moreover, Fig. 6.4(b) shows the ligament diameter of both alloys increases considerably with increasing

overpotential. During the coarsening process, average grain size increases with smaller particles shrink and disappear, resulting in densification and reduction in surface area [153]. For set A, ligament length increases from ~ 35 to ~ 105nm when the overpotential is increased from 0.1 to 0.75V. This trend was observed also for set B. However, the maximum overpotential of set B is smaller than set A so that set B has narrower range of strut size.

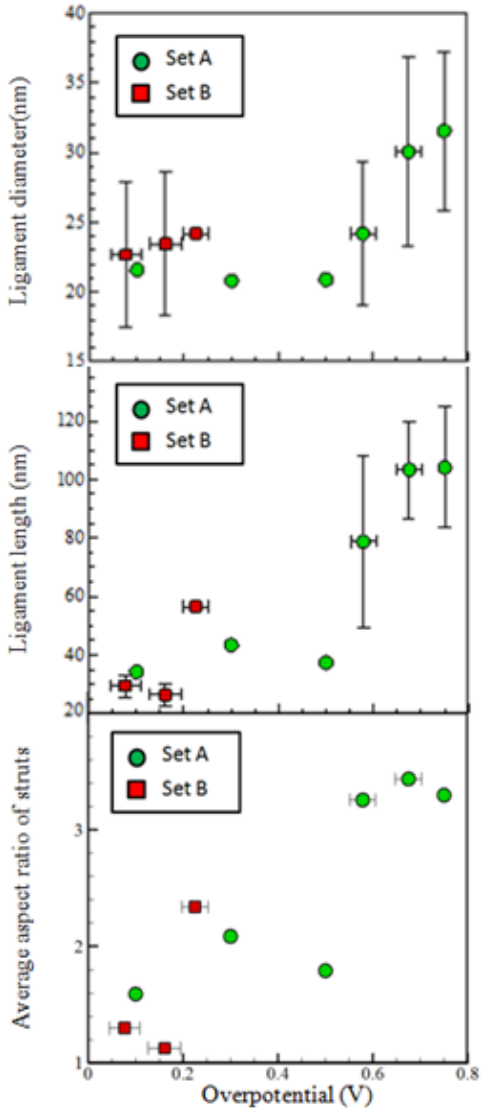

Figure 6.4. (a) Ligament diameter (b) ligament length and (c) aspect ratio of struts vs. overpotential. Ligament diameter and length were directly measured from SEM images. The error bars show the range of possible ligament sizes

Fig. 6.4(c) shows the aspect ratio of ligament (length over width) as a function of overpotentials. The aspect ratio increases from ~ 1.5 to ~ 3.5 when the overpotential is increased from 0.05 to 0.75. We observed that the small clusters tend to aggregate to form bigger and longer geometry to reduce the surface area when larger chemical energy is available, good agreement with previous work [17, 44, 73]. The largest overpotential we applied for set B is 0.25, as we found any potential higher than this value will lead to cracks and delamination during dealloying. This is in agreement with the fact that higher applied potential leads to the dissolution of copper into the electrolyte. In other words, the lower critical potential gives us much bigger room to tailor the sample. The cluster/strut size can be also tailored by immersion into 3% HF electrolyte for a few to tens of minutes.

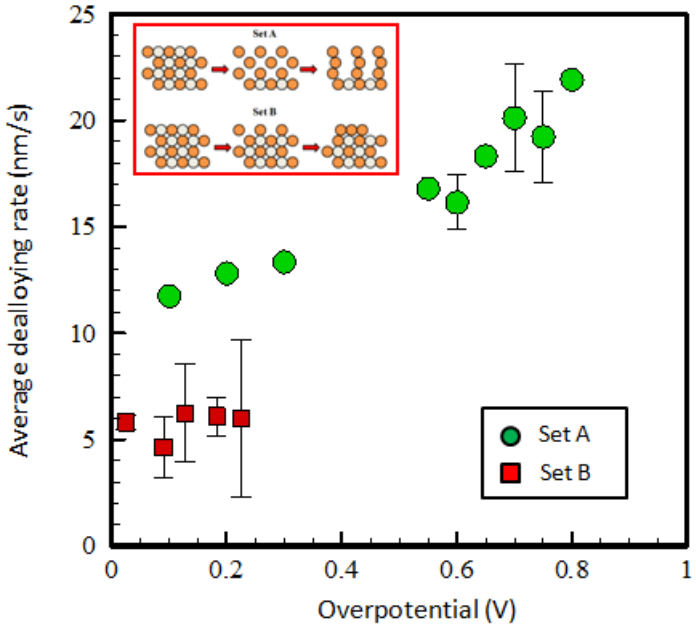

Figure 6.5. Dealloying rate as a function of overpotential.

Another important parameter that affects the structure size is dealloying rate which is proportional to the amount of silicon removed after the dealloying process. The

dealloying rate is determined by the applied potential and can be calculated from the film thickness before and after dealloying. Figure 6.5 shows the dealloying rate for NP Cu with different compositions as a function of overpotential. The data set in green circle are samples from set A. The data set in red square represents samples from set B. As can be seen from the figure 6.5, the dealloying rate increases by 2 times (from ~12 to ~22 nm/s) with increasing in overpotential. However, the dealloying rate for set B is smaller, below 10 nm/s even at highest overpotential. This indicates that nanosized clusters with low aspect ratio of ligaments of samples from set B may not solely due to the composition but may due to the limited of overpotential of set B since lower dealloying rate means slower dissolution of silicon and allowing more time for diffusion of copper atoms [39]. This can explain the clustering structure of set B. Meanwhile, higher overpotential resulted from lower critical potential can cause fast etching of the less noble element and promotes surfaced diffusion of the more noble element which accelerate size growth of the pore and ligament [154]. The more anisotropic structure of set A is also due to its faster etching rate in thickness direction than set B. This indicate copper atoms released due to the dissolution of its neighboring silicon may not combined with its neighbors in the lateral direction but can aggregate with atoms from its underneath. It is much more difficult to do so for set B because the slow dealloying rate of set B could not release the copper atoms from underneath fast enough to form those elongate ligaments (inset of Fig. 6.5). In other words, copper atoms from set B are more limited to aggregate with other copper atoms in the lateral direction rather than in thickness direction. This can also explain why the aspect ratio of NP Cu increases rapidly with the overpotential (Fig. 6.4 (c)).

Fig. 6.6 shows the SEM tilted cross-sectional images of NP Cu after immersion in electrolyte for 10 mins from a) sample from set A dealloyed at V=0.1V) and b) sample from set B dealloyed at V=0.25V, which involves surface diffusion of copper atoms to reduce the surface area and thus minimize the surface energy. After the immersion, the ligaments of both alloys were dramatically coarsened. The average ligament diameter increases from 20 nm to 70nm for set A and from 23 nm to 100 nm for set B with aspect ratio is about 2-3. We note that, for both alloys, the orientations of struts or clusters were randomly distributed, indicating the clusters aggregate to their neighbors not only from the underneath direction but also from neighbors at the same height.

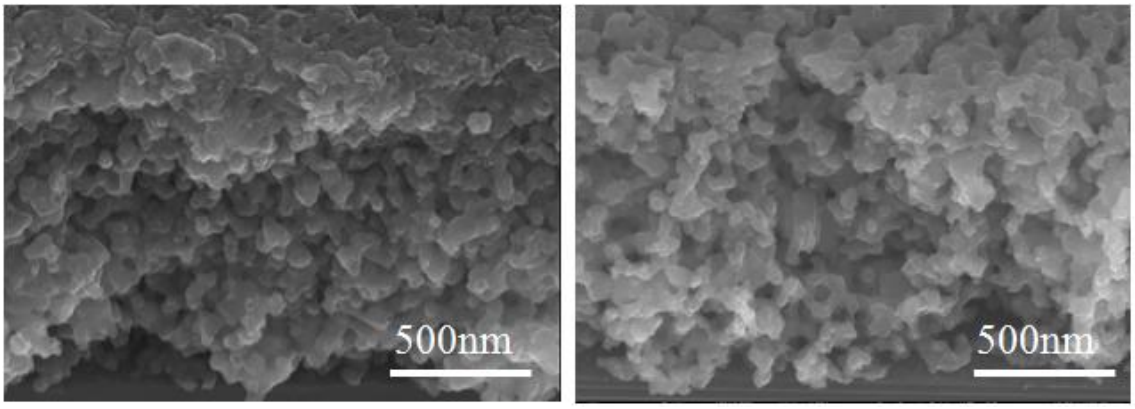

Figure 6.6 SEM 45^{o} tilted images of NP Cu after immersion in electrolyte 10mins a) based on foams with elongated ligmanents, and based on b) metal clusters

6.3.2 Indentation test

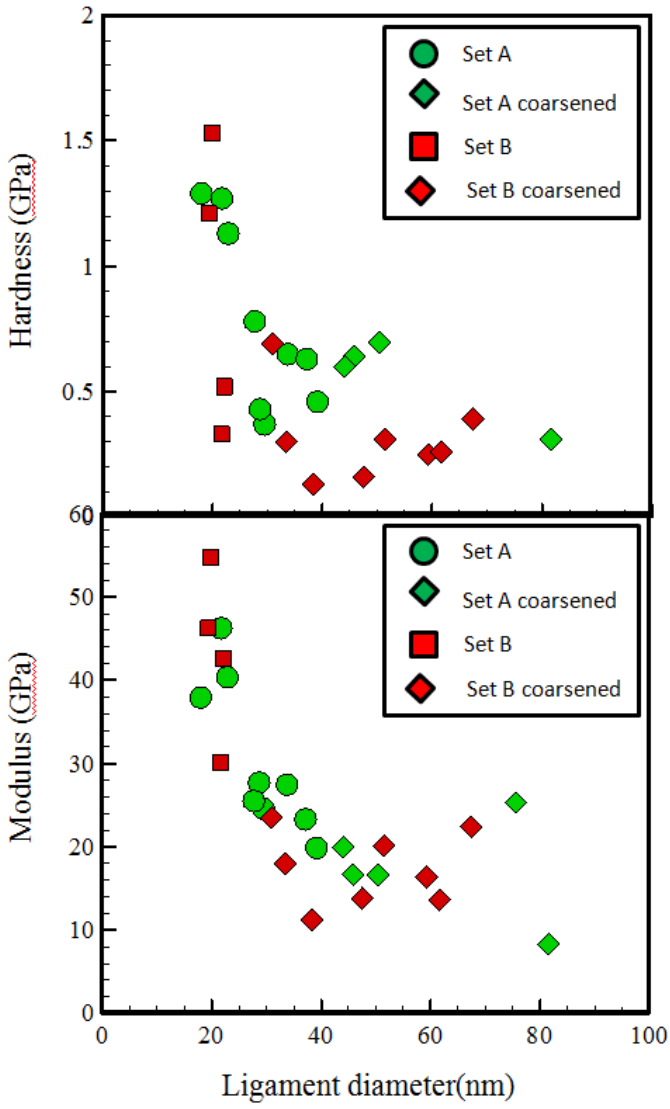

Figure 6.7 Plot of elastic modulus/ hardness vs. ligament sizes. Symbols in green color represent set A and red corresponds to set B.

Fig. 6.7(a) shows the hardness of NP Cu with different composition as a function of strut thickness. The data set in circle and square are samples as synthesized and the data set in diamond are samples undergo coarsening. For each specimen, in order to limit substrate effects, only the data points within the 30% of foam thickness are used to calculate the average value. The results show that hardness of both compositions

decreases as strut thickness increases. The significant decrease in hardness may be attributed to the strut thickness size effect, which has been discussed in our previous paper [112]. In addition, the extremely high mechanical properties were found for both hardness and modulus. This may partially due to the remaining silicon. Surprisingly, the Young's modulus also shows a similar trend as hardness (Fig. 6.7(b)). The dependence of modulus on strut size has been discussed in following papers. For each specimen, in order to limit substrate effects, only the data points within the 30% of foam thickness are used to calculate the average value. The results show that hardness of both compositions decreases as strut thickness increases. In addition, the ultrahigh mechanical properties were found for both hardness and modulus. Surprisingly, the Young's modulus also shows a similar trend as hardness. The dependence of modulus on strut size has been discussed in following papers.

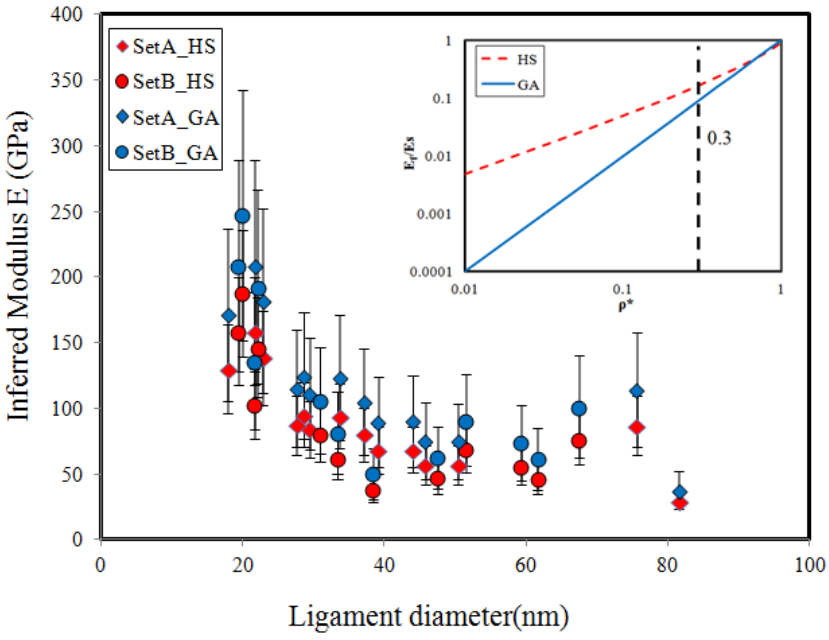

Figure 6.8 Plot of inferred elastic modulus vs. strut diameter. The error bar shows the range of possible strut strength for relative density in the range of 0.4-0.6.

The relative modulus of the nanoporous structure, Ef/Es given by Gibson-Ashby (G-A) scaling equation is expressed as

$$Ef/Es = \rho^{*2} \tag{6.1}$$

where Ef is the stiffness of the NP metal, Es is the stiffness of a solid strut. This equation is derived from unit cell which assumes the dominate deformation mode is due to strut bending. However, because the structure of NP copper is apparently different from the isotropic open cell foams, the dominated-deformation mechanism for such structure is still unclear. Hence, it is instructive to compare results the G-A scaling equation with Hashin-Shtrikman (H-S) upper bond which gives prediction for the tightest bonds for a two-phase material. The relative modulus of NP metal can be obtained (Appendix B)

$$Ef/Es = f(\rho^*, v) \tag{6.2}$$

Where E* is the foam modulus measured from nanoindentation, v is the Poisson's ratio of a solid strut. The inferred modulus of a solid strut was calculated from Eq. (6.1) and Eq. (6.2) and the comparison in reported in Fig. 8, where the inferred elastic modulus of struts of NP Cu dealloyed from set A and Set B as a function of ligament diameter. The data set in red diamond (set A), red circle (set B) are data calculated from H-S model and the data set in blue diamond (set A), blue circle (set B) are from sample G-A scaling equation. The error bar represents the variation due to the relative density (0.4-0.6). For both alloys, the inferred modulus decreases as increasing in ligament diameter. For as synthesized sample strut size varying from 20 to 80 nm, the inferred results from G-A scaling equation gives value in the range of 38 – 210 GPa; whereas H-S model gives 30-160 GPa, which is about 24% lower than the result from G-A scaling equation. This

estimation agrees well with the modulus of nanocrystalline copper which is typically 30-130 GPa [155]. In order to analyze the difference between these two models, a comparison was plotted in the insert which shows the ratio of relative modulus, Ef/Es as a function of relative density. Solid blue line corresponds to G-A scaling equation and the dotted red line corresponds to H-S model. There is a significant difference in the predication of relative modulus when relative density < 0.3. However, with in the relative density range of 0.4 to 0.6, the value obtained from G-A scaling equation is close to the H-S bond. This result indicates the deformation mode of nanoporous foams is compression-dominated since the HS bond is supposed to give the optimized estimation for any given relative density of cellular solids. Moreover, the quality of foams is dependent on the dealloying conditions and highest mechanical properties were found for those samples dealloyed with lowest overpotentials for both alloys. We suspect that other than strut size, the internal defects, randomness of structure, density of twins which could be influenced by the dealloying process may also play a role in the finally mechanical properties. Further study and more experimental data is needed to quantify the influence of the contamination on the mechanical properties.

6.4 ***Conclusion***

This work has focused on three aspects synthesis of novel nanoporous copper foam from two different compositions, investigation the correlation between the overall potential and strut sizes, and the study of mechanical behavior of NP Cu under the effects of strut size and composition. It gives us a better understanding of the underlying mechanisms behind the formation of struts and factors that control the mechanical properties.

CHAPTER 7

EXPERIMENTAL AND NUMERICAL ANALYSIS OF NANOINDENTATION OF NANOPOROUS METAL USING FLAT PUNCH INDENTER

7.1 ***Introduction***

The mechanical behavior of nanoporous (NP) metals has received much attention in recent years. Similarly to other nanostructured materials, NP metals exhibit physical behavior markedly different from their bulk counterparts. Large scale tests, such as uniaxial tension or compression experiments, are often not feasible for nanoporous metals due to the challenges of synthesizing macroscopic crack-free samples. In fact, the majority of crack-free nanoporous metals have been synthesized on thin films. For such systems, mechanical properties are frequently assessed by nanoindentation, a convenient and fast technique that requires minimal sample preparation. In nanoindentation experiments the reduced modulus is typically obtained from the unloading curve, using the procedure outline by Oliver and Pharr [90, 91]. The hardness can be calculated from the projected contact area after unloading. In order to achieve consistent results over different systems, considerable amount of research has been focused on improving the accuracy of such measurements by adding to the models additional parameters that account for the effect of the substrate or the porosity change. On the other hand, uniaxial compression experiments of micropillars with flat-ended punch were used as an

alternative way to measure uniaxial stress [41, 156, 157]. The data analysis is comparatively easier to carry out and the true stress can be obtained from the loading curve. However, this technique requires nontrivial effort to fabricate the pillars with special care needed to minimize the damage during FIB processing [158, 159].

In order to overcome the limitations mentioned above, we have utilized an alternative way to measure the mechanical properties from nanoindentation that is based on the analysis on the loading curve. In this SEM *in-situ* indentation experiment, the indentation is performed at the free edge of the sample using flat punch and SEM images are simultaneously acquired. This methodology has several crucial advantages compared to the earlier methods. First, no special sample fabrication is needed, which greatly reduces both the sample preparation effort and the risk of affecting the properties of the material during nanofabrication. Second, the material can be observed during deformation, allowing identification of dominant deformation modes. Moreover, if a suitable pattern can be imposed on the surface, full-field displacement and strain maps can be obtained using Digital Image Correlation (DIC). Finally, an important (and well appreciated) advantage of using flat punch over frequently utilized Berkovich indenters that the transition from elastic-dominated to plastic-dominated processes can be readily identified.

In this Chapter, the methodology is described in details. First, the framework for the analysis is established using finite element and analytical models. Then the technique is demonstrated in experiments on NP Cu. We demonstrate that non-trivial surface morphology of NP metals allows DIC analysis to be performed without additional

patterning, assuming one is interested in large-scale deformations (with characteristic scales significantly larger than unit cell).

7.2 ***Experimental Methodology***

Amorphous $Cu_{0.41}Si_{0.59}$ by atomic ratio with a thickness of 2.2 μm was co-sputtered on to (100) silicon substrate using DC magnetron sputter with Ar pressure of 5 x 10^{-8} Torr. Substrate bias 100V was applied during the deposition, which introduced compressive residual stress on the order of 100 MPa. A three-electrode electrochemical cell was employed for the electrochemical dealloying that was performed with applied potential of 0.1V (vs. SCE) in 3% hydrofluoric acid at room temperature. The composition of thin film before and after dealloying was determined by using X-ray Photoelectron Spectroscopy (XPS). The results show that silicon was completely removed from its original alloy after the dealloying process. The resulting NP Cu thin film was tested using the Hysitron TI-85 PicoIndenter with a flat-ended cube corner tip with circle of 1 μm in diameter. The specimen was compressed at a constant displacement rate of $\dot{h}$ = 2nm/s. The indentation was performed on the edge of the thin film and SEM images were obtained during the loading. The centerline of the cylindrical indenter is at the free surface of the specimen. The SEM images were recorded at 1frame/s and later synchronized with the load displacement curve. The approximate width of the field of view is approximately 2 x 2 μm. Each image is obtained with a camera with size of 1024 x 943 pixels.

7.3 ***Indentation Theory***

The problem of the contact between two elastic bodies has been developed by Hertz[160]. Unlike Berkovich or spherical indenter whose contact radius is a function of indent depth *h*, the contact radius of plat-ended punch is essentially equal to the radius of indenter *a*. The mean contact pressure is given by the equation [161]:

$$p_m = \frac{2Eh}{\pi(1-\nu^2)a} \tag{7.1}$$

where E is the reduced modulus and ν is the Poisson ratio. The total load is

$$F = \frac{2Eah}{(1-\nu^2)} \tag{7.2}$$

In this work, we define the mean indentation strain is $\varepsilon_m = h/a$, thus the effective modulus E^* during compression is equal to $E^* = 2E/[\pi(1-\nu^2)]$. Since the experiment is performed at the free edge, only half of the indenter will come into contact with the specimen. The required force for the same displacement is proportional to its corresponding contact area, which is $0.5(\pi a^2)$ instead of πa^2. Hence, Eq. (7.2) should be replaced by the following equation:

$$F = \frac{Eah}{(1-\nu^2)} \tag{7.3}$$

The relationship between mean pressure and mean strain is mainly determined by the material properties E and *v*. The changes associated with positioning the indenter away from the mid-point are discussed in section 7.4.

7.4 ***Numerical simulation***

Three-dimensional finite element simulations were performed using the commercial finite element code ABAQUS/Standard. Contact between an analytical rigid

flat-ended punch indenter and a homogenous elastic-plastic specimen was established using a hard contact formulation in the direction normal to the surface and a finite sliding formulation in the transverse direction. The specimen was built as a rectangular prism with a total of 38880 eight-node C3D8R elements. Finer meshes near the contact region were designed to ensure the accuracy of the calculation. Figure 7.1(a) shows the overall mesh design for the computational model. Fig. 7.1(b) schematically shows the setup of the experiment. The region of contact has a higher element density than the other area. The model assumes frictionless contact and ignores the surface roughness. The indenter has a flat-ended surface with assigned circle of 1 μm in diameter. Similarly to the indenter used in the experiments, the indenter has an overall conical shape with a 60^o angle (see Fig. 7.1(b)).

The mechanical behavior of material was modeled as pure elastic. The values of $E = 25\ GPa$ and $\nu = 0.3$ were chosen to compare the simulation to the nanoindentation experiment. In order to examine the transition from elastic-perfectly plastic regime, we also analyzed elastic-perfectly plastic models with σ_Y of 200~600 MPa. The FEM model was employed to study the effects of off-center contact with the free edge. As can be seen in Fig. 7.1(b), the portion of indenter within the specimen can be related to variable x, which represents the coordinate of the edge of the indenter relative to the sample edge. In that case, x=a denotes the only half of indenter is inside the specimen, while x=0 denotes that the indenter is totally inside the edge.

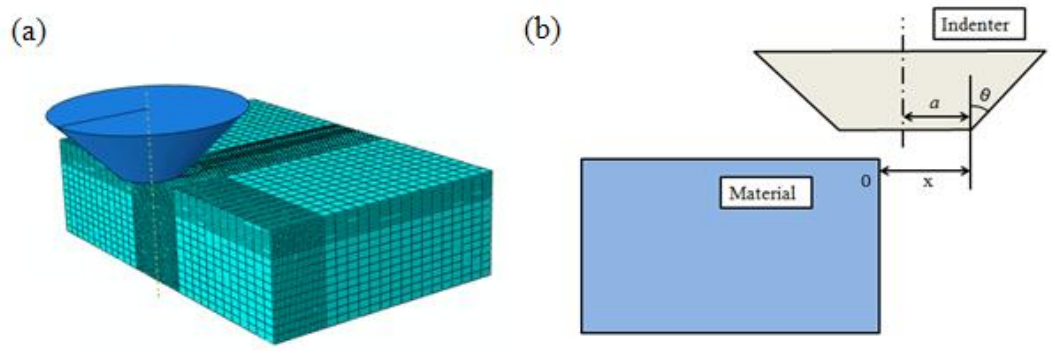

Figure 7.1 Computational modeling of plat punch indentation. (a) Mesh design for finite element analysis, (b) Schematic drawing of the setup of the indentation

7.5 ***Results and discussion***

7.5.1 Comparison between Hertz and FEM model

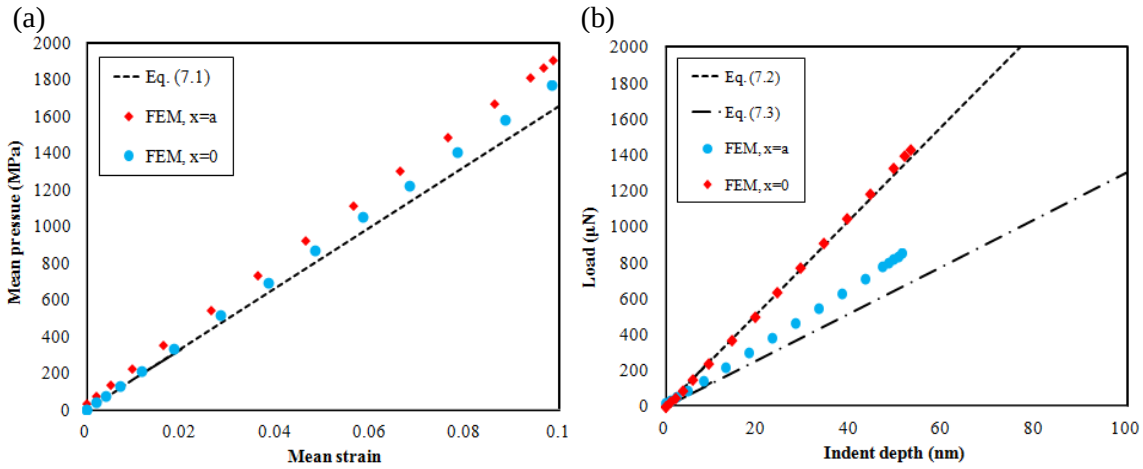

Figure 7.2 Comparison of results from analytical solution and FEM elastic models: (a) mean pressure as a function of mean strain (b) Total load as a function of indent depth. Color data points are results from numerical simulations.

Figure 7.2(a) shows a plot of mean pressure as a function of mean strain. The dotted line is prediction of Eq. (7.1). Blue colored circle are for the model with the whole indenter contact with the specimen and red colored diamond are the model with only half of the indenter contact with the specimen. The mean pressure from FEM models are

obtained from dividing the reaction force by its real time contact area. We found the difference between models is within 10%. On the other hand, the total load can be severely affected by the contact area as can be seen in Fig. 7.2(b). Eq. (7.3) has a much better agreement with results from the FEM model with x=a. The deviation of the FEM results from the analytical prediction may be due to the combination of factors, such as the presence of free surface and the conical geometry of the indenter in FEM model.

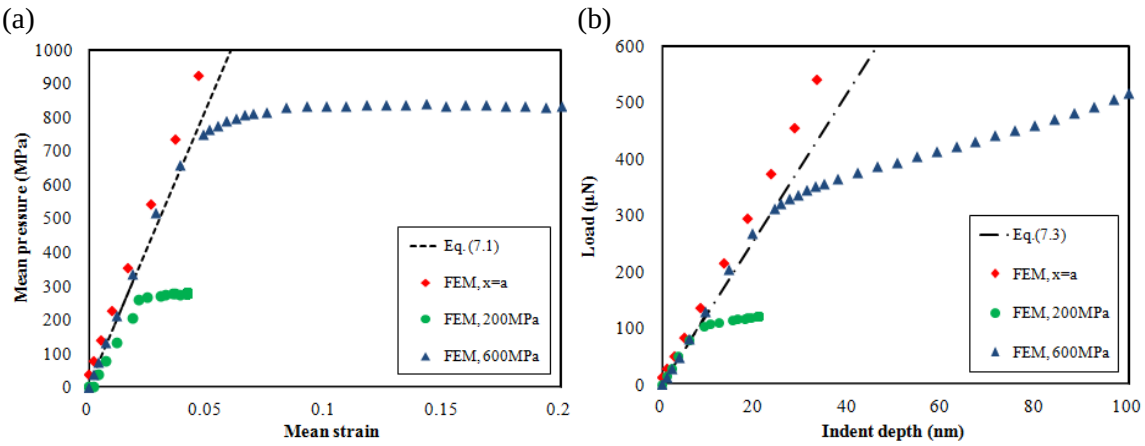

Figure 7.3 Comparison of results from analytical equation and numerical models. (a) mean stress-strain curve, (b) load-indent depth curve from different models.

Figure 7.3(a) shows a plot of mean pressure from elastic model and elastic perfectly-plastic model as a function of mean strain. The dotted line is prediction from Eq. (7.1). Symbols marked with blue triangles are for the model with yield strength of 600 MPa and Symbols marked with green circles are from the model with yield strength of 200 MPa. As can be seen from Fig. 7.3(a), data from elastic pure-plastic FEM models start to deviate from the analytical solution at some values, which are dependent on the yield strength. The mean pressure reaches 260 MPa for σ_y =200MPa, and 800 MPa for σ_y =600 MPa. Hence, for the flat-ended cylindrical indenter, the mean pressure can be related to the yield strength by $H/\sigma_y \sim 1.3$. Although material can have different values of

yield strength, the Eq. (7.1) can used to predict the mean pressure if the Young's modulus is known, or the vice versa. The transition from elastic deformation to plastic deformation can be identified from the slope of pressure vs. strain curve. Similar trends were also found for the curve of total load vs. indent depth as shown in Fig. 7.3(b). This is in contrast to the nanoindentation with a sharp Berkovich indenter, which normally has a continuous increasing slope of the loading curve and the elastic properties can be only abstracted from the unloading curve.

7.5.2 Experimental results

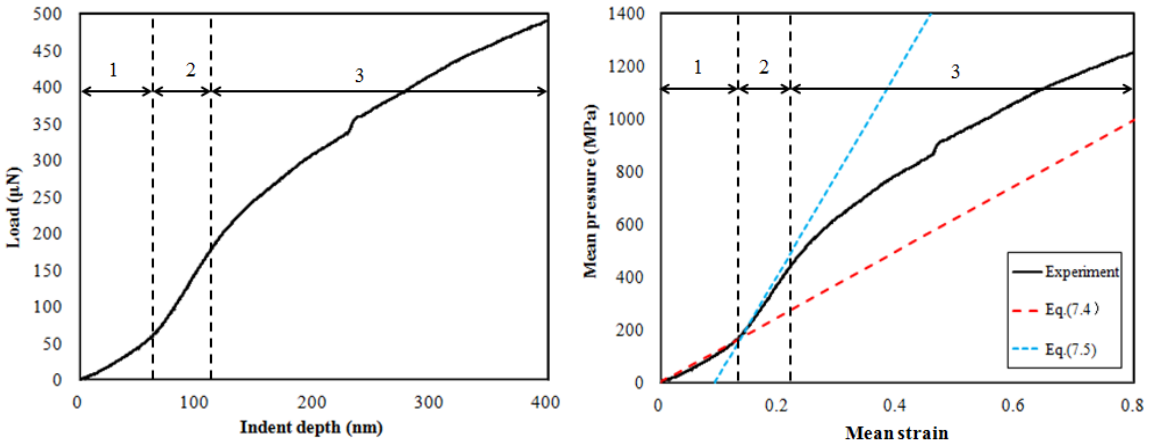

Figure 7.4 (a) Experimental response of load-indent depth curve on NP Cu, (b) experimental versus analytical results of mean pressure-strain curves. The blue and red dotted lines are predictions from Eq. (7.4) and Eq. (7.5), respectively.

Figure 7.4(a) shows a plot of load as a function of indent depth from the nanoindentation experiment on NP Cu. This curve can be divided into three regions: 1) Region 1 will be shown to be establishment of contact between the sample and the indenter. 2) Region 2 is characterized mostly by the elastic deformation. 3) Region 3 corresponds to transition from elastic to inelastic deformation. Figure 7.4(b) shows a plot of mean pressure as a function of the ratio between indent depth and contact area. In

region 2, the slope of the curve is 3.5 GPa, which is only one fifths of the value of approximately 17 GPa calculated from Eq. (7.1) assuming the mechanical properties of NP Cu as assessed by nanoindentation with standard Berkovich indenter ($E{\sim}25\ GPa, H{\sim}600\ MPa$). A close inspection of the SEM images revealed that this difference may be attributed to a gap at the interface between the silicon substrate and the NP Cu that formed during dealloying (see Fig. 7.5).

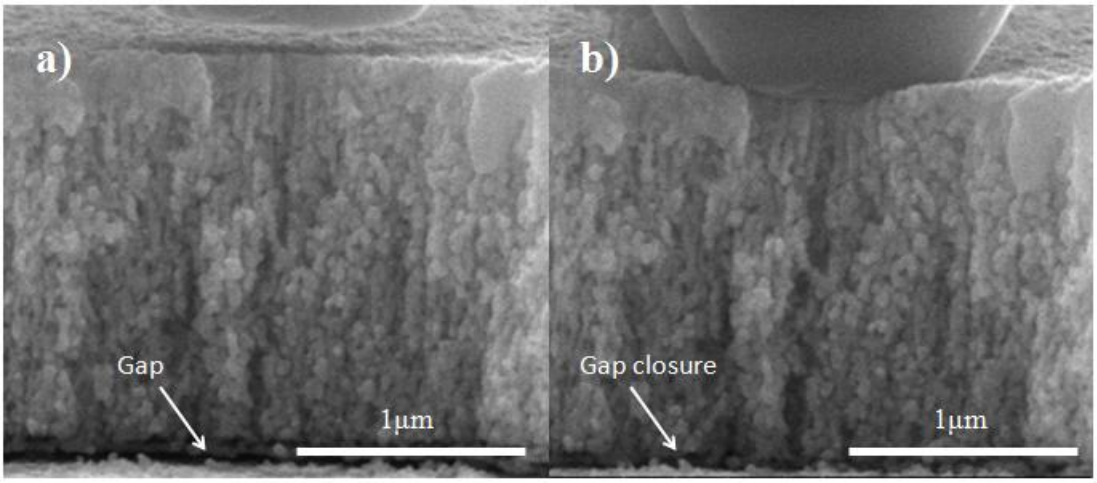

Figure 7.5 SEM images at (a) before come into contact and (b) after deformation at 60s. The displacement of the gap closure was measured from these two images.

Figure 7.5 shows the cross section view of NP Cu (a) before deformation and (b) after loading at 164 μN. At that load the gap is completely closed and the total indent depth is 106 nm. In order to extract the material properties from the mean pressure curve, we have adopted a phenomenological model that assumes that the processes of the gap closing can be modeled as linear elastic with an average stiffness K. From Fig. 7.6, the average stiffness can be calculated as $\mathrm{K} = 164\mu\mathrm{N}/42.6\mathrm{nm} = 3.904\mu N/nm$. Hence the total indent depth of stage 1 can be expressed as

$$h_{tot} = h_{intial} + h_{gap} = \frac{\mathrm{p_m}}{\beta \mathrm{E}^*} a + \frac{F}{K} \tag{7.4}$$

Here $\beta < 1$ is a numerical constant introduced to account for establishment of contact between the indenter and the sample. When compared the prediction from Eq. (7.4) to the experimental data, $\beta = 0.1$ was found to have a good fit.

Eq. (7.4) should be valid until the full contact is established, resulting in a sudden slope increase. The transition occurs when $h_{tot} = 60\text{nm}$, F=56μN. From Eq. (7.4) the inferred $h_{intial,1} = 46nm$ and $h_{gap,1} = 14nm$. We should note that these values also agree well with the measurement directly from SEM images. After full contact was established, the total indent depth h_{tot} can be expressed as

$$h_{tot} = h_{intial,1} + \frac{\mathrm{p_m}}{\mathrm{E^*}} a + \frac{F}{K} \tag{7.5}$$

We find a good agreement between Eq. (7.5) and experimental data. This indicates the possibility of extracting Young's modulus from the nanoindentation with flat-ended cylindrical indenter.

The main advantage of the flat punch indenter however is in the considerably less ambiguous (compared to the Berkovich indenter) determination of the yield strength. In the present experiment, the mean pressure is about 450MPa when the slope changes (transition from Region2 to Region 3). Using $H/\sigma_y \sim 1.3$ obtained from FEM simulations, the inferred yield strength of NP Cu can be estimated as σ_y~350 MPa, which is within the (wide) range of the inferred yield strength $\sigma_Y = 200\sim600MPa$ from nanoindentation with Berkovich indenter.

7.6 ***In-plane strain maps***

One of the main benefits of the edge indentation lies in the fact that the deformation underneath the indenter could be monitored. The utility of the images has already been demonstrated in the previous section, since they allowed unambiguous identification of the loading stages where the full contact between the indenter and the sample and the sample and the substrate is established. Here we demonstrate that the SEM images could be used to obtain full-field average displacement and strain maps. The analysis is performed using Digital Image Correlation (DIC) that compares the relative movement of subsets of an undeformed and deformed image. For this analysis to be successful, an appropriate pattern needs to be present on the surface. In the case of the porous copper foam, the contrast of the pores with the solid struts provides a suitable pattern. We emphasize that deformation within individual struts may not be quantified using this method. However, it suffices for quantitative analysis of average deformations with characteristic spatial scales exceeding the dimension of the individual struts and pores.

Figure 7.6 shows the effective strain obtained by DIC analysis at various levels of loading during the NP Copper experiment. The effective strain is defined as $E_{eff} = \sqrt{2/3(e_{ij}e_{ij})}$, where $e_{ij} = E_{ij} - E_{kk}\,\delta_{ij}/3$ is the deviatoric component of the Langrangian strain. The analysis was performed using a subset window radius of S_R = 60 pixels (~140 μm), an overlap of 1 pixel, and a strain window size of 15 pixels. Scanning Electron Micrographs often have high levels of noise since sample charging imposes a tradeoff between image resolution and the noise level. In order so suppress the

characteristic speckle noise, prior to analysis the images were denoised with a median filter of radius 2 pixels using ImageJ software. Figure 8 indicates that deformation is localized at a short distance below the indenter (Figure b-d) in agreement with Hertz theory. The deformation is highly localized along the center of the deformation zone where a combination of compressive (along the vertical direction) and tensile strains (along the horizontal) are present. The material tears along the mid-section of the sample indicating that it may be more susceptible to tensile strains than compressive. This is in agreement with behavior of other porous metals at larger scales.

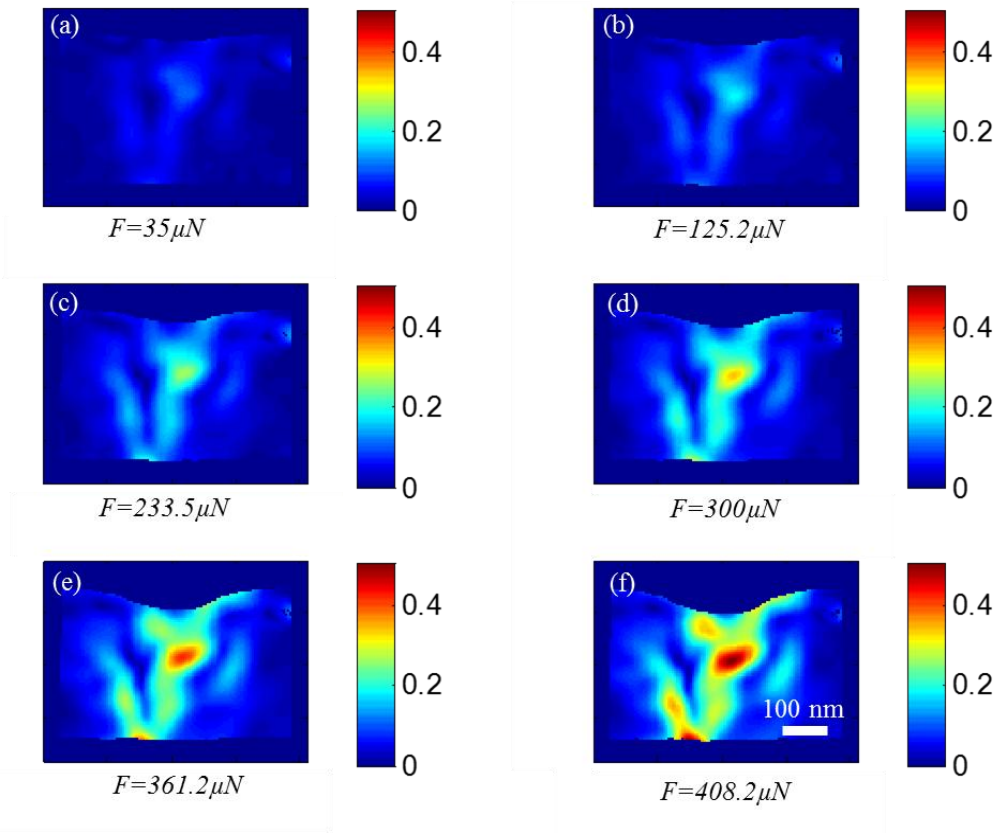

Figure 7.6. (a-f) In-plane effective strain of NP Copper indentation at increasing levels of loading. The material yields when F~230 μN (panel c).

7.6 Summary

The flat-ended cylindrical indent near the sample edge can be used to obtain the Young's modulus as well as a better estimate of the yield strength of the material. Ability to observe the deformation of the sample during indentation provides several crucial benefits, including unequivocal identification of various characteristic regimes. Moreover, full-filed strain and deformation maps can be obtained if the material can be patterned or posses an inherent pattern as is the case for NP metals. We demonstrated the application of this technique to in-situ experiment of NP Cu. In-plane strain maps of the material can complement the force-displacement dataset to provide a more detailed understanding of the deformation mechanisms of this material.

CHAPTER 8

CONCLUSIONS AND FUTURE DIRECTIONS

8.1 ***Conclusions***

Nanoporous (NP) metals are high density, open cell foams that retain such important properties of their metal constituents as catalytic activity, mechanical strength, and conductivity, while exposing a large surface area per volume. At the same time, understanding of their physical properties is often lacking, especially for hierarchical NP metals where individual struts and joints that make up open cell 3D network are nanocrystalline. This work employed a dedicated experimental campaign to understand the structure property relation of nanostructured nanoporous metals. Towards this goal, NP Pt and NP Cu have been synthesized for a range of strut sizes and their mechanical properties (modulus and hardness) have been investigated via ex-situ and in-situ nanoindentation experiments. NP metals synthesized during this work demonstrated catalytic activity comparable or significantly higher than the best available alternative systems, while offering superior stability. The main results of this work have been presented in a series of publications, the summary of which is given below.

Ran Liu and Antonia Antoniou. "A relation between relative density, alloy composition and sample shrinkage for nanoporous metal foams." ***Scripta Materialia*** **67.12 (2012): 923-926.**

NP metals synthesized by dealloying of amorphous silicide alloys often have nanosized grains within the struts. During dealloying, the silicon dissolves in the electrolyte while the remaining element self assembles into a 3D network. Dealloying

needs to be carefully controlled to yield homogeneous crack-free structures with highly optimized properties. For example, the sample volume is not preserved during dealloying. The substantial change in dimensions (up to 70%) can create a mismatch strain between the dealloyed and undealloyed material that can be further exacerbated for thin films deposited on a substrate. Tensile stresses of up to $\sim 15\ GPa$ were estimated to develop during dealloying. Such high values of stress are unsustainable, so the system will either shrink into a structure of higher density or will develop cracks. In order to combat the effects of tensile stresses and synthesize crack free foams, amorphous alloy films under residual compressive stress can be deposited. We have developed and experimentally verified a relationship between shrinkage volume, relative density and atomic fraction. Ignoring the effect of shrinkage can severely underestimate the measurements of relative density, causing up to an order of magnitude error in weight-normalized properties.

Ran Liu and Antonia Antoniou. "A relationship between the geometrical structure of a nanoporous metal foam and its modulus. " ***Acta Materialia*** **61.7 (2013): 2390-2402.**

Physical properties of a porous material typically exhibit correlation with its relative density. For example, the modulus and strength of large-scale foams follow well-established scaling laws that have been verified across many systems. In NP metals, material effects associated with the nanoscale structure contribute significantly to the overall properties of the material. In practice, the contribution of these effects is often estimated by first accounting for the influence of the relative density by using the classical scaling laws established in porous materials of larger scale. At the same time, dealloying was found to result in high density foams (>30% by solid volume fraction),

which is a relatively unexplored transition regime where the traditional scaling laws may no longer be applicable. An experimental investigation into the modulus of NP metals showed that it does not exhibit a clear correlation with the relative density. We trace this apparent disagreement with existing scaling laws to the agglomeration of mass in the junctions and derive and verify a scaling relationship. We find good agreement between our model and experimental measurements for single crystal gold NP foams with large junction sizes. In contrast, polycrystalline NP Platinum with nanosized grains within the struts showed an enhancement in the modulus that could not be attributed to the foam geometry only. Based on this analysis, we inferred more than an order of magnitude enhancement of the modulus of the nanograined Pt struts compared to bulk Platinum.

Ran Liu, Jacob Gruber, Drhriti Bhattacharyya, Garritt J. Tucker, and Antonia Antoniou. "Mechanical Properties of Nanocrystalline Nanoporous Platinum." (Under review)

The yield strength of NP metals and its scaling with the characteristic internal scales (such as strut thickness) has been the subject of intense investigation in the last decades. Most of these investigations focused on NP metals with grain sizes significantly exceeding the characteristic dimensions of the porous structure. At the same time, dealloying of amorphous silicides often results in structures where the grain size D is comparable to the strut dimensions t. This regime is virtually unexplored in NP metals, but is of great practical and theoretical interest. Some insights could be drawn from investigation of nanocrystalline nanowires, another system with overlapping scale length for geometrical features and grain structure. The yield strength is not directly measured in the experiments, but rather inferred from measurements of hardness (which is estimated

to be within 1 to 3 times greater than yield strength) that can be obtained from nanoindentation. We measured the hardness of NP Pt using nanoindentation with a Berkovich indenter. In addition, properties of individual struts with grain structure similar to that observed in the NP Pt synthesized by dealloying of amorphous silicide were examined using molecular dynamics simulations. Surprisingly, the NP Pt with struts in the t=3-10 nm range and grain size equal to the strut diameter has a hardness in the 0.2-1.25 GPa range. Therefore, the hardness of nanostructured NP Pt is not significantly different than that of NP metals with larger t and $D>>t$, where individual struts are effectively single crystal. The hardness is found to weakly decrease with decreasing average thickness of the struts, but the dependence on aspect ratio (t/l) is much weaker than the expectations drawn from a simple dimensional analysis. Atomistic simulations for *t=5-15 nm* struts show that the flow stress weakly decreases with strut diameter for nanocrystalline Pt struts under compression, but remains in the range (2-4) GPa. This agrees fairly well with the strength of individual struts inferred from the indentation experiments using dimensional analysis.

The catalytic activity of NP Pt described in this work during the butadiene hydrogenation reaction was examined in Ref.[7]. Butadiene hydrogenation is a very fast and exothermic reaction. It was found that a bimodal network of pores and the columnar NP Pt structure facilitated reaction throughout the entire film depth and likely contribute to the absence of ignition. The very high surface area (350 m^2 catalyst per m^2 substrate) resulted space time yields two to three orders of magnitude greater than other Pt based catalysts and exceeded performance of the more ideally suited Pd based catalysts. Moreover, the NP Pt catalysts were found to be stable up to 200 ℃.

Ran Liu, Shijian Zheng, Jon Kevin Baldwin, Mary Kuthuru, Nathan Mara, and Antonia Antoniou. "Synthesis and mechanical behavior of nanoporous nanotwinned copper." ***Applied Physics Letters*** **103, no. 24 (2013): 241907.**

Another system examined in this work was NP Copper by dealloying amorphous copper silicide thin films. The resulting NP Copper was nanocrystalline with struts in the *20-80 nm* range and grain size equal to the strut thickness. A significant population of twins with spacing *~7 nm* is present within each imaged grain. Two distinct geometrical arrangements of struts were found by changing the initial alloy composition and the applied dealloying potential. The strut length and thickness scaled with increasing potential so that the aspect ratio of strut length to thickness ranges from 1.5 to 3.5 times when the overpotential increases from 0.05 to 0.75 V. The modulus of NP Copper is found to increase with decreasing strut thickness. The hardness of this nanocrystalline, nanotwinned NP Cu is approximately one order of magnitude greater than reports on NP Cu in the literature. Under the assumption of strut yielding by compression and anisotropic unit cell the strength of individual struts is approximately an order of magnitude greater than bulk copper and compares well with other nanostructured copper systems.

Ran Liu, Jon Kevin Baldwin, Mary Kuthuru, Nathan Mara, and Antonia Antoniou. "Electrochemical dealloying synthesis and characterization of nanoporous copper by nanoindentation." (Under preparation)

Here, we report synthesis of nanoporous copper (NP Cu) through electrochemical dealloying of two initial amorphous alloys $Cu_{0.41}Si_{0.59}$ and $Cu_{0.45}Si_{0.55}$ by atomic ratio. After the dealloying process, distinct different morphologies including nanosized clusters

and elongated ligaments were observed from SEM micrographs. We found that the geometry of ligaments can be largely affected by the critical potential and the applied potential. Finally, we also made a comparison of results from different models based on different deformation mechanisms to study the mechanical properties of NP Cu.

Ran Liu, Bill Mook, Nathan Mara, and Antonia Antoniou. "Experimental and numerical analysis of nanoindentation of nanoporous metal using flat punch indenter." (Under preparation)

While the mechanical properties of nanostructured NP metals could be obtained from widely used Berkovich nanoindentation, inferring the uniaxial yield strength from hardness measurements is nontrivial. The corresponding proportionality constant can have values between 1 and 3. This places a large uncertainty in the inferred mechanical properties. Nanoindentation with a flat or spherical indenter is an alternative technique that allows a much more constrained determination of the yield strength. At the same time, these types of experiments possess present their own challenges. We have proposed an *in-situ* nanoindentation experiment using a flat punch positioned at the edge of the sample that overcomes many of the previous limitations. The positioning of the indenter allows the deformed area to be directly imaged in SEM during the deformation. First, the flat punch indentation force-displacement relationship was examined using analytical and numerical models. Nanoindentation with flat punch results in a clear elastic deformation stage which has much sharper slope than the following inelastic deformation stage. This may be attributed to the much larger volume under compression than the sharp Berkovich indenter. For all the tested models, the ratio of the hardness to the uniaxial yield strength (H/σ_Y) for this flat-ended indenter was found to be ~ 1.3. Subsequently, an *in-situ*

experiment was performed on NP Cu that demonstrated the utility of the proposed technique. The strength of NP Cu was found to be 350MPa, a much more accurate estimate than previously obtained using Berkovich indentation. One of the main benefits of edge indentation is that the deformation of the material could be analyzed using digital image correlation (DIC) and in-plane strain maps could be obtained. We demonstrate that inherent surface morphology of NP metals provides a suitable pattern for DIC analysis. Combined with the force-displacement measurements the strain maps could provide a more robust analysis of heterogeneous deformation of nanostructured materials. We anticipate that this technique can become particularly useful to study some delicate or soft materials which are susceptible to damage due to the FIB process.

8.2 ***Future directions***

The microstructure of NP metals is quite complex and a comprehensive understanding of their structure-property relation remains elusive. However, we anticipate that predictive models can be established capable of capturing the dominant factors controlling the material properties. Specifically, better understanding of the role of geometrical structure of NP metals can be established through a dedicated effort targeting the challenging regime of relative densities of the order of 50%. The geometrical effects such as the connectivity (average number of struts per node), anisotropy, irregular strut geometry and randomness of overall foam can be further studied by establishing finite element models and carrying out experimental mechanical tests on the macroscopic foams made by a 3D printer. Besides, since the modulus is a size insensitive property especially when struts thickness above 10nm, the relative modulus is good indicator of how stiff the structure is. Once such models which can capture the

geometrical effects are established, much more accurate information regarding the role of nanoscale structure can be inferred from the experiments and compared with numerical simulations. More work is needed to understand the small-scale deformation mechanisms of NP metals. Towards this end, *in-situ* experiments on micropillars combined with edge indentation and *in-situ* TEM tests could provide crucial information.

On the other hand, different mechanical experiments including nanoindentation with plat punch, cylindrical indenter or pillar compression can be carried out on NP metals. These techniques are not only compatible with in-situ experiments but may improve the accuracy of the measurement especially the yield strength of foams when compared to the Berkovich indenter. More work is needed to establish the correlation between the mechanical response and material properties for different types of experiments.

The large surface area of NP metals can be utilized in a range of applications from sensors to electrochemical energy storage devices and catalysts. One particularly promising direction appears to be the use of processing to optimize the geometrical arrangement and/or strut surface texture of NP metals. Our preliminary results demonstrated that order of magnitude enhancements in activity could be achieved while maintaining the stability of the structure. Since metal catalysts are used in multitude of applications from petroleum refinement to fuel cells, the design of highly efficient NP metal based catalysts can have a dramatic impact on many in many fields.

Appendix A. Mechanical properties for rectangular unit cell with large joints

The modulus and strength of a unit cell shown in Fig. 3.7 (b) are derived here. Each strut has length l and square crosssection of dimension t. The unit cells form a three-dimensional structure by being stacked at an offset so that a load can be applied at the midpoint of each strut. The threedimensional assembly is similar to the unit cell Gibson and Ashby used to derive properties for open cell foams [10].

A strut of such structure will deform by bending due to force *P* applied at the midpoint of the strut length. This force can be related to the remote compressive stress σ, by $P = \sigma l^2/2$.

$$\delta_c = \int_0^{l/2} \left(\frac{M}{EI}\right)\left(\frac{\partial y}{\partial x}\right) dx = \int_0^{t+d} \left(\frac{Px}{2EI_1}\right)\left(\frac{x}{2}\right) dx + \int_{t+d}^{\frac{l}{2}} \left(\frac{Px}{2EI_2}\right)\left(\frac{x}{2}\right) dx \qquad \text{A.1}$$

The moment M is related to the force P, by $M = Px/2$. It follows that the displacement

$$\delta_c = \frac{P}{12EI_1}(t+d)^3 + \frac{P}{12EI_2}\left[\left(\frac{l}{2}\right)^3 - (t+d)^3\right] \qquad \text{A.2}$$

In the above equation, $I_1 = (t+d)^4/12$, $I_2 = t^4/12$. The strain ε can be related to the displacement δ_c by $\varepsilon = \delta_c/l$. The relative Young's modulus for a rectangular unit cell with large joints is:

$$E_j^* = \frac{2}{(t/l + d/l)^{-1} + 1/8(t/l)^{-4} - [(t/l)^3 + 3(t/l)^2(d/l) + 3(d/l)^2(t/l) + (d/l)^3](t/l)^{-4}} \qquad \text{A.3}$$

The ratio of the relative moduli of rectangular unit cells with and without large joints, E_j^*/E^* can be obtained by dividing Eq. (A.3) with $E^* = 16(\frac{t}{l})^4$, the relative modulus of a rectangular unit cell without large joints (Fig. 3.6(a)).

$$E_j^*/E^* = \frac{1/8\,(t/l)^{-4}}{(t/l + d/l)^{-1} + 1/8(t/l)^{-4} - [(t/l)^3 + 3(t/l)^2(d/l) + 3(d/l)^2(t/l) + (d/l)^3](t/l)^{-4}} \quad \text{A.4}$$

Appendix B. Relative modulus for nanoporous metals based on H-S upper bond

The relative modulus of solid are derived here. From H-S, the bulk modulus K*, shear modulus G* of cellular solids can be related to the property of the solid

$$K_f = K_{solid} + \frac{1-\rho^*}{-K_{solid}^{-1}+3\rho^*(3K_{solid}+4G_{solid})^{-1}} \quad \text{B.1}$$

$$G_f = G_{solid} + \frac{1-\rho^*}{-G_{solid}^{-1}+(6\rho^*/5)(K_{solid}+2G_{solid})(3K_{solid}+4G_{solid})^{-1}} \quad \text{B.2}$$

After combine above two equations with $G_{solid}=E_{solid}/[2(1+v)]$ and $K_{solid}=E_{solid}/[3(1-2v)]$, the Modulus of NP foam E_f can be expressed as a function of relative density, ρ^* and the modulus of solid, E_s as

$$E_f/E = -\frac{2\rho^*(5v-7)}{15(\rho^*-1)v^2+2(\rho^*-6)v-13\rho^*+27} \quad \text{B.3}$$

The inferred modulus of solid can be obtained

$$E = -E_f\frac{15(\rho^*-1)v^2+2(\rho^*-6)v-13\rho^*+27}{2\rho^*(5v-7)} \quad \text{B.4}$$

REFERENCES

[1] Zhang S, Xing Y, Jiang T, Du Z, Li F, He L, Liu W. Journal of Power Sources 2011;196:6915.

[2] Lang XY, Hirata A, Fujita T, Chen MW. Nature Nanotechnology 2011;6:232.

[3] Mao-Sung W, Yu-An H, Chung-Hsien Y, Jiin-Jiang J. International Journal of Hydrogen Energy 2007;32:4153.

[4] Snyder J, Fujita T, Chen MW, Erlebacher J. Nature Materials 2010;9:904.

[5] Chen LY, Fujita T, Ding Y, Chen MW. Advanced Functional Materials 2010;20:2279.

[6] Bryce C T, Stephen A Iii S, Luther EP. Angewandte Chemie - International Edition 2010;49:4544.

[7] Kraehnert R, Ortel E, Paul B, Eckhardt B, Kanis M, Liu R, Antoniou A. Catalysis Science & Technology 2015.

[8] Xinyi Z, Dan L, Bourgeois L, Huanting W, Webley PA. ChemPhysChem 2009;10:436.

[9] Biener J, Wittstock A, Zepeda-Ruiz LA, Biener MM, Zielasek V, Kramer D, Viswanath RN, Weissmuller J, Baumer M, Hamza AV. Nature Materials 2009;8:47.

[10] Li Y, Antoniou A. Scripta Materialia 2012;66:503.

[11] Biener J, Hodge AM, Hayes JR, Volkert CA, Zepeda-Ruiz LA, Hamza AV, Abraham FF. Nano Letters 2006;6:2379.

[12] Crowson DA, Farkas D, Corcoran SG. Scripta Materialia 2009;61:497.

[13] Detsi E, Van De Schootbrugge M, Punzhin S, Onck PR, De Hosson JTM. Scripta Materialia 2011;64:319.

[14] Dongyun L, Xiaoding W, Manhong Z, Xi C, Seong CJ, Hone J, Jeffrey WK. Modelling and Simulation in Materials Science and Engineering 2007;15:181.

[15] Hakamada M, Mabuchi M. Scripta Materialia 2007;56:1003.

[16] Jin H-J, Kurmanaeva L, Schmauch J, Rosner H, Ivanisenko Y, Weissmuller J. Acta Materialia 2009;57:2665.

[17] Yi D, Young-Ju K, Jonah E. Advanced Materials 2004;16:4.

[18] Li R, Sieradzki K. Physical Review Letters 1992;68:1168.

[19] Forty AJ. Nature 1979;282:597.

[20] Wagner K, Brankovic SR, Dimitrov N, Sieradzki K. Journal of the Electrochemical Society 1997;144:3545.

[21] Dursun A, Pugh DV, Corcoran SG. Journal of the Electrochemical Society 2003;150:B355.

[22] Biener J, Hodge AM, Hamza AV. Applied Physics Letters 2005;87.

[23] Forty AJ, Durkin P. Philosophical Magazine a-Physics of Condensed Matter Structure Defects and Mechanical Properties 1980;42:295.

[24] Forty AJ, Rowlands G. Philosophical Magazine a-Physics of Condensed Matter Structure Defects and Mechanical Properties 1981;43:171.

[25] Hodge AM, Doucette RT, Biener MM, Biener J, Cervantes O, Hamza AV. Journal of Materials Research 2009;24:1600.

[26] Sun Y, Balk TJ. Metallurgical and Materials Transactions a-Physical Metallurgy and Materials Science 2008;39A:2656.

[27] Pugh DV, Dursun A, Corcoran SG. Journal of Materials Research 2003;18:216.

[28] Antoniou A, Bhattacharrya D, Baldwin JK, Goodwin P, Nastasi M, Picraux ST, Misra A. Applied Physics Letters 2009;95.

[29] Thorp JC, Sieradzki K, Tang L, Crozier PA, Misra A, Nastasi M, Mitlin D, Picraux ST. Applied Physics Letters 2006;88.

[30] Sun L, Chien CL, Searson PC. Chemistry of Materials 2004;16:3125.

[31] Hayes JR, Hodge AM, Biener J, Hamza AV, Sieradzki K. Journal of Materials Research 2006;21:2611.

[32] Min US, Li JCM. Journal of Materials Research 1994;9:2878.

[33] Pickerin.Hw, Wagner C. Journal of the Electrochemical Society 1967;114:698.

[34] Pryor MJ, Fister JC. Journal of the Electrochemical Society 1984;131:1230.

[35] Seker E, Gaskins JT, Bart-Smith H, Zhu J, Reed ML, Zangari G, Kelly R, Begley MR. Acta Materialia 2007;55:4593.

[36] Seker E, Gaskins JT, Bart-Smith H, Zhu J, Reed ML, Zangari G, Kelly R, Begley MR. Acta Materialia 2008;56:324.

[37] Ding Y, Kim YJ, Erlebacher J. Advanced Materials 2004;16:1897.

[38] Jin HJ, Kurmanaeva L, Schmauch J, Rosner H, Ivanisenko Y, Weissmuller J. Acta Materialia 2009;57:2665.

[39] Sun Y, Balk TJ. Scripta Materialia 2008;58:727.

[40] Gibson LJ, Ashby MF. Cellular solids : structure and properties. Cambridge ; New York: Cambridge University Press, 1997.

[41] Volkert CA, Lilleodden ET, Kramer D, Weissmuller J. Applied Physics Letters 2006;89.

[42] Biener J, Hodge AM, Hamza AV, Hsiung LM, Satcher Jr JH. Journal of Applied Physics 2005;97.

[43] Lee D, Wei X, Chen X, Zhao M, Jun SC, Hone J, Herbert EG, Oliver WC, Kysar JW. Scripta Materialia 2007;56:437.

[44] Mathur A, Erlebacher J. Applied Physics Letters 2007;90.

[45] Gibson LJ, Ashby MF. Proceedings of the Royal Society of London, Series A (Mathematical and Physical Sciences) 1982;382:43.

[46] Woesz A, Stampfl J, Fratzl P. Advanced Engineering Materials 2004;6:134.

[47] Wang AJ, McDowell DL. Journal of Engineering Materials and Technology-Transactions of the Asme 2004;126:137.

[48] Roberts AP, Garboczi EJ. Proceedings of the Royal Society of London Series a-Mathematical Physical and Engineering Sciences 2002;458:1033.

[49] Petch NJ. Journal of the Iron and Steel Institute 1953;174:25.

[50] Hall EO. Proceedings of the Physical Society of London Section B 1951;64:747.

[51] Thompson AW. Metallurgical Transactions a-Physical Metallurgy and Materials Science 1977;8:833.

[52] Young CM, Sherby OD. Journal of the Iron and Steel Institute 1973;211:640.

[53] Chokshi AH, Rosen A, Karch J, Gleiter H. Scripta Metallurgica 1989;23:1679.

[54] Schiotz J, Di Tolla FD, Jacobsen KW. Nature 1998;391:561.

[55] Onck PR, Andrews EW, Gibson LJ. International Journal of Mechanical Sciences 2001;43:681.

[56] Andrews EW, Gioux G, Onck P, Gibson LJ. International Journal of Mechanical Sciences 2001;43:701.

[57] Zhou B, Prorok BC. Experimental Mechanics 2010;50:793.

[58] Zhou B, Prorok BC. Journal of Materials Research 2010;25:1671.

[59] Doerner M, Nix W. J Mater Res 1986;1.

[60] Miller RE. International Journal of Mechanical Sciences 2000;42:729.

[61] Gioux G, McCormack TM, Gibson LJ. International Journal of Mechanical Sciences 2000;42:1097.

[62] Weissmuller J, Newman RC, Jin HJ, Hodge AM, Kysar JW. Mrs Bulletin 2009;34:577.

[63] Tsui TY, Oliver WC, Pharr GM. Journal of Materials Research 1996;11:752.

[64] Detsi E, Punzhin S, Rao JC, Onck PR, De Hosson JTM. Acs Nano 2012;6:3734.

[65] Rösner H, Parida S, Kramer D, Volkert CA, Weissmüller J. Advanced Engineering Materials 2007;9:535.

[66] Mukherjee S, Carmo M, Kumar G, Sekol RC, Taylor AD, Schroers J. Electrochimica Acta 2012;74:145.

[67] Erlebacher J. Journal of the Electrochemical Society 2004;151:C614.

[68] Zhang Q, Wang XG, Qi Z, Wang Y, Zhang ZH. Electrochimica Acta 2009;54:6190.

[69] Liu R, Antoniou A. Acta Materialia 2013;61:2390.

[70] Parida S, Kramer D, Volkert CA, Rosner H, Erlebacher J, Weissmuller J. Physical Review Letters 2006;97:035504.

[71] Hodge AM, Biener J, Hayes JR, Bythrow PM, Volkert CA, Hamza AV. Acta Materialia 2007;55:1343.

[72] Custer JS, Thompson MO, Jacobson DC, Poate JM, Roorda S, Sinke WC, Spaepen F. Applied Physics Letters 1994;64:437.

[73] Thorp JC. Nanoporous electrode formation by electrochemical dealloying of platinum-silicon and gold-silicon thin films. Arizona: Arizona State University, 2006.

[74] Li WC, Balk TJ. Scripta Materialia 2010;62:167.

[75] Okman O, Lee D, Kysar JW. Scripta Materialia 2010;63:1005.

[76] Tada H. The stress analysis of cracks handbook. New York :: ASME Press, 2000.

[77] Zeis R, Mathur A, Fritz G, Lee J, Erlebacher J. Journal of Power Sources 2007;165:65.

[78] Barth JV. Annual Review of Physical Chemistry 2007;58:375.

[79] Erlebacher J, Sieradzki K. Scripta Materialia 2003;49:991.

[80] Buckingham E. Physical Review 1914;4:345.

[81] Hai-Jun J, Xiao-Lan W, Parida S, Ke W, Seo M, Weissmuller J. ACS Nano Letters 2010;10:187.

[82] Antoniou A, Bhattacharrya D, Baldwin JK, Goodwin P, Nastasi M, Picraux ST, Misra A. Applied Physics Letters 2009;95.

[83] Simone AE, Gibson LJ. Acta Materialia 1998;46:2139.

[84] Detsi E, van de Schootbrugge M, Punzhin S, Onck PR, De Hosson JTM. Scripta Materialia 2011;64:319.

[85] Ning Y, Nastasi M, Levine TE, Tesmer JR, Hollander MG, Evans CR, Maggiore CJ. In-situ capability of ion beam modification and characterization of materials at Los Alamos National Laboratory. vol. B99. Netherlands, 1995. p.566.

[86] Doolittle LR. Nuclear Instruments & Methods in Physics Research Section B-Beam Interactions with Materials and Atoms 1986;15:227.

[87] Doolittle LR. Nuclear Instruments & Methods in Physics Research Section B-Beam Interactions with Materials and Atoms 1985;9:344.

[88] Chu W-K. Backscattering spectrometry. New York :: Academic Press, 1978.

[89] Feldman LC, Mayer JW, Picraux ST. Materials analysis by ion channeling : submicron crystallography. New York: Academic Press, 1982.

[90] Oliver WC, Pharr GM. Journal of Materials Research 1992;7:1564.

[91] Oliver WC, Pharr GM. Journal of Materials Research 2004;19:3.

[92] Gao H, Chiu CH, Lee J. International Journal of Solids and Structures 1992;29:2471.

[93] Biermans E, Molina L, Batenburg KJ, Bals S, Van Tendeloo G. Nano Letters 2010;10:5014.

[94] Abramoff MD, Magalhaes PJ, Ram SJ. Biophotonics International 2004;11:36.

[95] Seiler H. Journal of Applied Physics 1983;54:R1.

[96] Erlebacher J, Aziz MJ, Karma A, Dimitrov N, Sieradzki K. Nature 2001;410:450.

[97] Banhart J. Progress in Materials Science 2001;46:559.

[98] Kucheyev SO, Hayes JR, Biener J, Huser T, Talley CE, Hamza AV. Applied Physics Letters 2006;89.

[99] Okman O, Kysar JW. Journal of Alloys and Compounds 2011;509:6374.

[100] Liu R, Antoniou A. Scripta Materialia 2012;67:923.

[101] Balk TJ, Li WC. Thin Solid Films 2011;519:2393.

[102] Smithells CJ. Smithells metals reference book. Oxford: Butterworth-Heinemann, 1983.

[103] Dingreville R, Jianmin Q, Cherkaoui M. Journal of the Mechanics and Physics of Solids 2005;53:1827.

[104] Adams JB, Wolfer WG, Foiles SM. Physical Review B (Condensed Matter) 1989;40:9479.

[105] McDowell MT, Leach AM, Gall K. Nano Letters 2008;8:3613.

[106] Mathur A, Erlebacher J. Applied Physics Letters 2007;90:61910.

[107] Detsi E, Onck P, De Hosson JTM. ACS Nano 2013;7:4299.

[108] Wahl P, Traucnig T, Landgraf S, Hai-Jun J, Weissmuller J, Wurschum R. Journal of Applied Physics 2010;108:073706 (6 pp.).

[109] Hai-Jun J, Parida S, Kramer D, Weissmuller J. Surface Science 2008;602:3588.

[110] Hakamada M, Matsumura S, Mabuchi M. Materials Letters 2012;70:132.

[111] Ding DY, Chen Z, Lu C. Sensors and Actuators, B: Chemical 2006;120:182.

[112] Liu R, Zheng S, Baldwin JK, Kuthuru M, Mara N, Antoniou A. Applied Physics Letters 2013;103:241907.

[113] Deshpande VS, Ashby MF, Fleck NA. Acta Materialia 2001;49:1035.

[114] Chen C, Lu TJ, Fleck NA. Journal of the Mechanics and Physics of Solids 1999;47:2235.

[115] Farkas D, Caro A, Bringa E, Crowson D. Acta Materialia 2013;61:3249.

[116] Saane SSR, Mangipudi KR, Loos KU, De Hosson JTM, Onck PR. Journal of the Mechanics and Physics of Solids 2014;66:1.

[117] Gu XW, Loynachan CN, Wu Z, Zhang Y-W, Srolovitz DJ, Greer JR. Nano Letters 2012;12:6385.

[118] Deng C, Sansoz F. ACS Nano 2009;3:3001.

[119] Thorp JC, Sieradzki K, Tang L, Crozier PA, Misra A, Nastasi M, Mitlin D, Picraux ST. Applied Physics Letters 2006;88:1.

[120] Oliver WC, Pharr GM. Journal of Materials Research 1992;7:1564.

[121] Saha R, Nix WD. Acta Materialia 2002;50:23.

[122] Plimpton S. Journal of Computational Physics 1995;117:1.

[123] Sheng H, Kramer M, Cadien A, Fujita T, Chen M. Physical Review B 2011;83:134118.

[124] Tucker G, Zimmerman J, McDowell D. Modelling and Simulation in Materials Science and Engineering 2010;18:015002.

[125] Tucker GJ, Zimmerman JA, McDowell DL. International Journal of Engineering Science 2011;49:1424.

[126] Tucker GJ, Tiwari S, Zimmerman JA, McDowell DL. Journal of the Mechanics and Physics of Solids 2012;60:471.

[127] Volkert CA, Lilleodden ET, Kramer D, Weissmuller J. Applied Physics Letters 2006;89:61920.

[128] Hakamada M, Asao Y, Kuromura T, Chen Y, Kusuda H, Mabuchi M. Acta Materialia 2007;55:2291.

[129] Deshpande VS, Fleck NA. Journal of the Mechanics and Physics of Solids 2000;48:1253.

[130] Wu MS, Huang YA, Yang CH, Jow HH. International Journal of Hydrogen Energy 2007;32:4153.

[131] Zhang SC, Xing YL, Jiang T, Du ZJ, Li F, He L, Liu WB. Journal of Power Sources 2011;196:6915.

[132] Bringa EM, Monk JD, Caro A, Misra A, Zepeda-Ruiz L, Duchaineau M, Abraham F, Nastasi M, Picraux ST, Wang YQ, Farkas D. Nano Letters 2011.

[133] Lu K, Lu L, Suresh S. Science 2009;324:349.

[134] Cao A, Wei Y, Mao S. JOM Journal of the Minerals, Metals and Materials Society 2008;60:85.

[135] Schiotz J, Jacobsen KW. Science 2003;301:1357.

[136] Jang D, Li X, Gao H, Greer JR. Nat Nano 2012;7:594.

[137] Qian LH, Chen MW. Applied Physics Letters 2007;91:083105.

[138] Cheng IC, Hodge AM. Advanced Engineering Materials 2012;14:219.

[139] Qi Z, Zhao CC, Wang XG, Lin JK, Shao W, Zhang ZH, Bian XF. Journal of Physical Chemistry C 2009;113:6694.

[140] Tekog˘lu C, Gibson LJ, Pardoen T, Onck PR. Progress in Materials Science 2011;56:109.

[141] Gibson LJ. The Elastic and Plastic Behavior of Cellular Materials. Churchill College, England, Cambridge: University of Cambridge, 1981.

[142] Jennings AT, Burek MJ, Greer JR. Physical Review Letters 2010;104.

[143] Wu ZX, Zhang YW, Jhon MH, Greer JR, Srolovitz DJ. Acta Materialia 2013;61:1831.

[144] Cao A, Wei YG, Ma E. Physical Review B 2008;77.

[145] Lu L, Shen YF, Chen XH, Qian LH, Lu K. Science 2004;304:422.

[146] Ding Y, Chen MW, Erlebacher J. Journal of the American Chemical Society 2004;126:6876.

[147] Liu ZN, Du JG, Qiu CC, Huang LH, Ma HY, Shen DZ, Ding Y. Electrochemistry Communications 2009;11:1365.

[148] Kramer D, Viswanath RN, Weissmuller J. Nano Letters 2004;4:793.

[149] Sieradzki K, Dimitrov N, Movrin D, McCall C, Vasiljevic N, Erlebacher J. Journal of the Electrochemical Society 2002;149:B370.

[150] Namboodhiri T, Tripathi R. Corrosion science 1986;26:745.

[151] Detor AJ, Hodge AM, Chason E, Wang Y, Xu H, Conyers M, Nikroo A, Hamza A. Acta materialia 2009;57:2055.

[152] Liu X, Frankel G, Zoofan B, Rokhlin S. Corrosion Science 2004;46:405.

[153] Wakai F, Yoshida M, Shinoda Y, Akatsu T. Acta materialia 2005;53:1361.

[154] Bartis E, Barrett C, Chung T, Ning N, Chu J, Graves D, Seog J, Oehrlein G. Journal of Physics D: Applied Physics 2014;47:045202.

[155] Siow K, Tay A, Oruganti P. Materials science and technology 2004;20:285.

[156] Beyerlein IJ, Mara NA, Carpenter JS, Nizolek T, Mook WM, Wynn TA, McCabe RJ, Mayeur JR, Kang K, Zheng S. Journal of Materials Research 2013;28:1799.

[157] Volkert CA, Lilleodden ET. Philosophical Magazine 2006;86:5567.

[158] Maaß R, Van Petegem S, Van Swygenhoven H, Derlet PM, Volkert CA, Grolimund D. Physical review letters 2007;99:145505.

[159] Shan Z, Mishra RK, Asif SS, Warren OL, Minor AM. Nature materials 2008;7:115.

[160] Hertz H. 1882.

[161] Riccardi B, Montanari R. Materials Science and Engineering: A 2004;381:281.

VITA

RAN LIU

Ran Liu was born in Beijing, China. He earned his B.S. degree and M.S. degree in Mechanical Engineering from Beijing Institute of Technology in 2007 and 2009. He came to Georgia Institute of Technology in 2009 to pursue his Doctoral degree in the Georgia W. Woodruff School of Mechanical Engineering. His research interests include 1) mechanics of materials with emphasis on understanding the connections among geometry, microstructure, deformation mechanisms, and mechanical properties; 2) synthesis and micro-characterization of advanced materials and 3) their applications in energy storage and micro-electrical-mechanical (MEMS) devices. He is a member of American Society of Mechanical Engineers (ASME); Materials Research Society (MRS); The Minerals, Metals and Materials Society (TMS).